**Skoltech**

Skolkovo Institute of Science and Technology

Skolkovo Institute of Science and Technology

THE EFFECT OF SELECTED ELECTRODE-SOLUTION INTERACTIONS ON THE
POTASSIUM-ION BATTERY ELECTROCHEMICAL PERFORMANCE

*Doctoral Thesis*

by

NATALIA KATOROVA

DOCTORAL PROGRAM IN MATERIALS SCIENCE AND ENGINEERING

Supervisor

Professor Keith Stevenson

Co-adviser

Professor Artem Abakumov

Moscow - 2022

I hereby declare that the work presented in this thesis was carried out by myself at Skolkovo Institute of Science and Technology, Moscow, except where due acknowledgement is made, and has not been submitted for any other degree.

Candidate (Natalia Katorova)

Supervisor (Prof. Keith Stevenson)

Co-adviser (Prof. Artem Abakumov)

**Abstract**

Potassium-ion batteries (PIBs) have attracted significant research interest during last decade due to its low cost combined with competitive energy density characteristics compared to Li-ion batteries. Hence, one of feasible PIB application relates to the stationary energy storage market that will experience exponential growth in coming years. However, full K cells exhibit poor electrochemical performance stemming from electrolyte decomposition during cycling due to the formation of unstable Solid Electrolyte Interphase (SEI) and Cathode Electrolyte Interphase (CEI) layers on surfaces of negative and positive electrodes respectively. Furthermore, hard carbon (HC) electrodes demonstrate the enormous irreversible capacity loss with low CE values at the first cycles. The deteriorated performance of HC electrodes in K cells during first cycles arises from continuous reduction of electrolyte components since the deficient surface passivation or surface film cracking leads to the presence of bare spots on electrode that are available for further interaction with electrolyte.

One approach to improve the stability of SEI/CEI layers over cycling is to tune electrolyte composition. But the examination of a wide variety of electrolyte solutions has limitations. Despite the published advantages of KFSI-contained ($KN(SO_2F)_2$) electrolyte utilization with carbonaceous negative electrodes, they still suffer from aluminum current collector corrosion. This is impermissible for the prosperous elaboration of K full cell with further PIB commercialization. Hence, $KPF_6$ electrolyte salt providing the aluminum passivation is used in present research. Other strategies to develop new generation electrolyte for PIBs comprise solvent change, the enhanced salt concentration, and the utilization of electrolyte additives. Herein, all these approaches are explored.

The effect of salt concentration in diglyme-based electrolytes on cycling performance of promising $KVOPO_4$ and $K_{1.44}Mn[Fe(CN)_6]_{0.9} \times 0.4H_2O$ positive electrodes (cathodes) and a hard carbon negative electrode (anode) for next-generation potassium-ion ($K^+$-ion) batteries is investigated. A decrease in free solvent molecule number with increasing electrolyte concentration is found, which results in a better aluminum current collector stability, formation of thinner solid electrolyte interphase (SEI) passivation layers, and further inhibition of solvent degradation redox processes occurring at the electrode surface upon cycling. The $KVOPO_4$ and $K_{1.44}Mn[Fe(CN)_6]_{0.9} \times 0.4H_2O$ cathodes exhibit an enhanced specific discharge capacity (54 and 105 $mA \cdot h \cdot g^{-1}$, respectively) in $K^+$-ion cells at the highest electrolyte concentrations (2 and 2.5 M $KPF_6$ in diglyme, respectively) at a 0.1 C rate. However, the behavior of the hard carbon anode is noticeably affected by the salt concentration over the first few cycles, a phenomenon tentatively attributed to the SEI layer formation and the presence of irreversible intercalation sites for $K^+$ ions

in the hard carbon framework. In addition, the SEI film formation on hard carbon electrodes cycled in diglyme-based solutions with different salt concentrations are examined via X-ray photoelectron spectroscopy (XPS), high-angular annular dark field scanning transmission electron microscopy (HAADF-STEM) and electrochemical impedance spectroscopy (EIS) to adjust the impact of SEI composition. Finally, electrochemical tests on K full cells consisting of the $K_{1.44}Mn[Fe(CN)_6]_{0.9} \times 0.4H_2O$ cathode, a hard carbon anode, and an ether-based electrolyte show capacity retention of 86% over 300 cycles at a 0.6 C rate.

The possible reasons of HC capacity loss are examined with a combination of *in situ* AFM and various ex-situ TEM techniques (HR-TEM and HAADF-STEM imaging, STEM-EELS and STEM-EDX spectroscopic mapping) targeting the electrode/electrolyte interphase formation process in carbonate-based electrolyte with and without vinylene carbonate (VC) as an additive. The studied HC consists of curved graphitic layers arranged into short packets and round cages, the latter acting as traps for $K^+$ ions causing low Coulombic efficiency between cycling. Our comparative study of solid electrolyte interphase (SEI) formation in the carbonate-based electrolyte with and without VC additive revealed that in the pristine electrolyte SEI consists mostly of inorganic components whereas adding VC introduces a polymeric organic component to the SEI increasing its elasticity and stability against fracturing upon HC expansion/contraction during electrochemical cycling. Therefore, the present research is dedicated to elaborate the electrolyte solution for PIB with superb electrochemical performance via tuning its composition and probing the surface layers formed on electrode surfaces.

**Publications**

1.      **N.S. Katorova**, S.Yu. Luchkin, D.P. Rupasov, A.M. Abakumov, K.J. Stevenson, Origins of irreversible capacity loss in hard carbon negative electrodes for potassium-ion batteries. *The Journal of Chemical Physics.* **152**, no. 19 (2020), 194704.

2.      S.Yu. Luchkin, S.A. Lipovskikh, **N.S. Katorova,** A.A. Savina, A.M. Abakumov, K.J. Stevenson, Solid-electrolyte interphase nucleation and growth on carbonaceous negative electrodes for Li-ion batteries visualized with in situ atomic force microscopy. *Scientific Reports* **10**, no. 1 (2020), 1-10.

3.      **N.S. Katorova**, D.P. Rupasov, S.S. Fedotov, N.D. Luchinin, B.Delattre, Y.-M. Chiang, A.M. Abakumov, K.J. Stevenson, Effect of Concentrated Diglyme-based Electrolytes on the Electrochemical Performance of Potassium-ion Batteries, *ACS Applied Energy Materials*, **2,** no.8 (2019), 6051-6059

**Author's Contribution**

1.      The author is mainly responsible for this work. The author performed the synthesis of hard carbon materials; its structural, morphological and electrochemical characterization, the preparation of electrolyte solutions and electrode composites. The author pre-treated the hard carbon samples for novel in situ atomic force microscopy measurements which experiment design is elaborated in our research group. The author examined the surface layers formed on electrodes via scanning electron microscopy and Energy-dispersive X-ray spectroscopy. The author also analyzed and visualized the data, wrote the original draft and submitted the manuscript. The co-authors performed the HR-TEM measurements, in situ atomic force microscopy measurements, as well as supervised the work.

2.      The co-authors performed the measurements and analyzed the obtained results, wrote the original draft and managed the work. The author synthesized the hard carbon material and characterized it via spectroscopic and microscopic techniques. The author also participated in the discussions and interpretations of the observed results.

3.      The author is mainly responsible for this work. The author conducted the synthesis of potassium manganese hexacyanoferrate and hard carbon materials, the structural, morphological and electrochemical characterization of both electrode and electrolyte materials, Raman measurements, potentiostatic electrochemical impedance spectroscopic measurements, the laboratory powder X-ray diffraction experiments, performed the sequential Rietveld refinement and the Rietveld refinement of selected patterns, analyzed and visualized the data, composed the original manuscript and submitted it.

**Novelty**

1.      To date, the advantages of diglyme-based electrolyte utilization for PIBs was demonstrated for the first time. The enhanced performance of $KVOPO_4$ and $K_{1.44}Mn[Fe(CN)_6]_{0.9} \times 0.4H_2O$ positive electrode materials in K half cells with ether-based electrolyte is presented for the first time.

2.      The elaborate K full cell comprising $K_{1.44}Mn[Fe(CN)_6]_{0.9} \times 0.4H_2O$ and hard carbon electrodes with ether-based electrolyte delivers the stable cycle life upon 300 cycles at scan rate of 0.6C corresponding to charging time of 100 minutes.

3.      The origins of irreversible capacity loss in K cell with hard carbon electrode are identified. They comprise the presence of sites for irreversible $K^+$-ion intercalation in hard carbon structure, the binder effect, the electrolyte decomposition, and the enhanced content of hard carbon nanospheres. The synthesis technique to obtain hard carbon microspheres with reduced content of "nanosized" particles for PIBs with stable cycle life is demonstrated.

4.      For the first time the formation of films on hard carbon surface in K cell comprising vinylene carbonate additive was probed using various spectroscopic and microscopic techniques. The strategy utilizing vinylene carbonate additive to enhance the electrochemical performance in K cells is demonstrated.

**Acknowledgements**

I would like to express my special thanks of gratitude to my advisors Professor Keith Stevenson and Professor Artem Abakumov, who encouraged me with research in the field of $K^+$-ion batteries and who also provided valuable guidance and feedback. My skills and expertise have been significantly elaborated owing your useful pieces of advice and trainings you granted.

I am also grateful to the following people, without whom I would not have been able to complete this PhD thesis research: Professor Yet-Ming Chiang, Dr. Sergey Luchkin, Dr. Stanislav Fedotov, Dr. Dmitry Rupasov, Polina Morozova, Dr. Maksim Zakharkin, Dr. Maria Kirsanova, Artem Zaikin, Dr. Oleg Drozhzhin, Dr. Elena Abramova and Nikita Luchinin,

I express my gratitude to my colleagues at the Skoltech Center for Energy Sciences and Technologies: A.Savina, S. Lipovskikh, D. Aksenov, V.Gorshkov, S. Ryazantsev, V. Nikitina, E. Pazhetnov, A. Buchachenko for productive discussion of the results as well as to my colleagues at the Chemistry Department of Lomonosov Moscow State University Professor Evgeny Antipov, Z. Bobyleva, I. Tereshchenko and V. Sumanov. I also thank our collaborators Benjamin Dellatre, Menghsuan Sam Pan and Elizabeth Shaw from Massachusetts Institute of Technology. I would also like to thank to all my labmates for their invaluable contribution.

I extend my gratitude to Skolkovo Institute of Science and Technology for the awesome opportunity to learn and work with all these splendid people as well as to MSU, MIT, Haldor Topsøe, LG Chem, and Russian Science Foundation for the support of this research.

I finally would emphasize my greatest appreciation of the love, support and patience of my friends and family, especially my beloved husband Alexey and daughter Ekaterina. It has become possible only with you.

**Table of Contents**

**List of Symbols, Abbreviations**

AFM - atomic force microscopy

CE -Coulombic efficiency

CEI - cathode electrolyte interphase

CV - cyclic voltammetry

DC - differential capacity

DRR - double-resonance Raman

DFT – density functional theory

EMC - ethylmethylcarbonate

EV - electric vehicle

FEC - fluoroethylene carbonate

GIC - graphite intercalation compound

HAXPS - hard X-ray photoelectron spectroscopy

HC - hard carbon

HS – high spin

HTC - hydrothermal carbonization

ICL - irreversible capacity loss

KMFCN – potassium manganese hexacyanoferrate with general formula $K_xMn[Fe(CN)_6]_y \cdot zH_2O$

LIB -lithium ion battery

LS – low spin

MD - molecular dynamics

MOPOF - metal organic phosphates open framework

PAQS - poly(anthraquinonyl sulfide)

PBA - prussian blue analogue

PIB - potassium ion battery

PTCDA - perylene-3,4,9,10-tetracarboxylic dianhydride

SAED - selected area electron diffraction

SEI - solid electrolyte interphase

TOF-SIMS - time-of-flight secondary ion mass spectrometry

VC - vinylene carbonate

XPS - x-ray photoelectron spectroscopy

XRD - x-ray diffraction

**List of Figures**

**List of Tables**

**Chapter 1. Introduction**

Global energy storage market experiences rapid growth owing the decarbonization in key industry segments. The present energy storage devices based on Li-ion or lead-acid batteries suffer from high cost or inferior characteristics, respectively. Potassium-ion batteries (PIBs) are considered to accomplish all requirements for stationary energy storage beyond $Li^+$-ion systems due to the reduced cost combined with the high energy density value. However, the PIB development faces issues concerning the faster cell degradation compared to Li+-ion counterparts. Furthermore, the electrode materials should accommodate wide enough channels for solid diffusion of large $K^+$-ions into structure.

Prussian blue analogues and polyanionic compounds are reported to enable the reversible $K^+$-ion (de)intercalation into lattice host owing to open 3D framework. Moreover, they deliver the specific discharge capacity values in the range of 80-140 $mA \cdot h \cdot g^{-1}$ and high operation potentials >4V *vs* $K^+/K$ ensuring the elaboration of high energy density PIBs. Nevertheless, the enhanced working potential requests the increased oxidation potential of used electrolyte components to suppress the irreversible cell degradation.

Hard carbon (HC) negative electrode facilitates the reversible $K^+$-ion (de)intercalation delivering high specific capacity values in the range of 220-260 $mA \cdot h \cdot g^{-1}$ without significant volume changes compared to commercial graphite. However, HC electrodes in $K^+$-ion cells suffer from the continuous irreversible capacity loss during cycling originating from the electrolyte decomposition. It might be avoided via formation of uniform and stable solid electrolyte interphase (SEI) on HC surface. Thereby, the urgent demand in electrolyte composition choice emerges.

The electrolyte solution should satisfy the requirements from both positive and negative electrode sides. Besides, it should passivate the current collectors to prevent their corrosion. The electrolyte decomposition should result in formation of stable and $K^+$-ion conductive surface layers. This research is dedicated to probe the SEI layer formation on HC electrode surface in carbonate-based and diglyme-based electrolytes in $K^+$-ion cells. Furthermore, the HC synthesis is optimized to attain best HC performance in PIBs.

**Chapter 2. Review of the Literature**

**Characteristics of metal-ion intercalation systems**

The decarbonisation in key segments of the energy market in order to avoid the risk of catastrophic climate change[1] boosted the global market of the energy storage devices up to approximately \$99bln in 2019[2] the tremendous part of which (86%) is based on the electrochemical devices such as Li-ion batteries or lead-acid batteries[2]. The latter one possesses deteriorated characteristics such as low energy density and operation lifetime. The lithium-ion batteries exceed the lead-acid ones in overall electrochemical parameters, but suffer from the high cost. This brings an urgent demand for cheap competitive alternative that might be PIB due to abundance of potassium in the Earth's crust (~21000 ppm compared to 26 ppm for Li). Therefore, the worldwide trend of the transition from fossil fuel to renewable energy has provoked the insistent development of alkali metal-ion battery technology beyond Li-ion.

The key cell components embody the positive and negative electrodes, electrolyte, separator and current collectors. The choice of battery components define the substantial cell characteristics - specific capacity, operating voltage, specific energy, rate capability and cycle life[3]. The electrode composition and structure establish the *electrode potential*. The *voltage* designates the potential difference between the electrodes.

The *specific charge* and *discharge capacities* of an electrode material in metal-ion battery are defined as the amount of charge passed at the charging or discharging steps, respectively, per unit weight of the active electrode material. The factors determining the capacity of the insertion electrode in the alkali metal-ion cell are as follows: (1) the capability to change the valence states of electrochemically active atoms (generally, transition metal atoms); (2) the availability of the host sites to accommodate the alkali metal ions $A^+$; and (3) the reversibility of the (de)intercalation reactions. The *theoretical*, or maximal, *capacity* of the selected electrode material correlates with the number of reactive electrons and the molar weight of the material, as expressed by the following equation:

$$C = \frac{z * F}{3.6 * M}$$

where z is the number of reactive electrons per formula unit, M is the molar weight of active electrode material, the constant 3.6 provides the unit transform from A·s to mA·h and F is the Faraday constant (F = 96485.3 C·mol⁻¹). The equation implies that the choice of the electrode with lower molecular weight and with the capability to accommodate more electrons per formula unit leads to a higher capacity in theory.

Energy and power available per unit weight are called the *specific energy* and *specific power* and measured in W·h·kg$^{-1}$ and W·kg$^{-1}$, respectively. These terms transform into the *energy density* (W·h·L$^{-1}$) and the *power density* (W·L$^{-1}$) to address the amount of energy or power that can be stored per unit volume. The energy contained in the metal-ion cell is the integral of voltage multiplied by the charge capacity

$$Energy = \int EdC.$$

In battery terminology, the *rate capability* reflects the maximum charge/discharge rate of a metal-ion cell and, generally, is designated in the C rate denotation. A C rate represents the (dis)charge current at which the battery is charged or discharge during the selected amount of time, e.g. 1C equals the charge/discharge during 1 hour; 0.5 C – during 2 hours, 2C – during 0.5 hour. The metal-ion battery with the enhanced rate capability might deliver a significant amount of power, providing the low voltage loss at high current loads. Particularly, it matters in the metal-ion battery development for electric vehicles (EVs).

Another crucial parameter is the *cycle life* that is determined as the number of cycles that an electrochemical cell can be effectively recharged before its performance (its capacity) has become too degraded. The *Coulombic efficiency* (CE) shows how the initial capacity is reduced during cycling: the equation

$$CE = \frac{C_{discharge}}{C_{charge}} * 100\%$$

reflects the fraction of the preceding charge capacity that is available during the following discharge. This depends on different factors, e.g., current load and depth of discharge in each cycle. Applications involving long-term operation require the metal-ion cells with the extremely low capacity loss per cycle.

Within the battery charging and discharging the electrode reactions are based on reversible intercalation/deintercalation of the alkali cations A$^+$ into the host electrode lattice with a simultaneous addition/removal of electrons leaving/entering the external electrical circuit through current collectors. The current applied to a metal-ion cell to recover its capacity is called charge current or charge rate. Conversely discharge rate or discharge current is a rate at which electrical current is removed from a battery. They both are usually expressed in terms of the C rate. The electrolyte role includes mass transport of ions from one electrode to another. This is the simplified scheme of metal-ion cell operation. However, the genuine situation also comprises charge transfer, cation (de)solvation, ion migration through surface films, the solid-state diffusion of alkali metal-ions A$^+$ in the host lattice, and, in many cases, phase transitions. The elucidation of these sophisticated processes is required to elaborate next generation battery with enhanced properties.

**Processes occurring during operation of the metal-ion intercalation system**

The charge transfer (CT) processes denote the crucial role in the alkali metal-ion intercalation systems. Firstly, the electron transfer from the current collector to the redox active center in the electrode lattice accompanies the structure modification due to the change in the oxidation state. Secondly, the alkali metal ion transfer from the bulk of electrolyte solution into the intercalation host is, in most cases, the rate-limiting step[4].

Solvated alkali metal ion $A^+$ diffuses to the electrode/electrolyte interface through the electrolyte solution. The solvation shell may encompass solvent molecules and anions of the electrolyte salt. The complete or partial desolvation occurs in the vicinity of the electrode surface. The desolvation energy depends on the solvent nature, ion radius and ion charge. It might contribute significantly to the apparent activation energy of the intercalation process in the case of the absence of the surface film formation[5].

One remarkable phenomenon manipulating the metal-ion battery performance consists in the formation of passivating films. During battery operation the electrochemical interaction between the bare electrode surface and the electrolyte components, in the most cases, results in the covering of negative or positive electrode surfaces by the solid electrolyte interphase (SEI) or cathode electrolyte interphase (CEI) layers, respectively[6]. The formation of SEI/CEI films on electrode surfaces is accompanied by the significant increase in the apparent activation energy of charge transfer[4]. By contrast, the formed surface layers prevent further electrolyte degradation. The electrolyte salt, solvent and additives alter the structure of the electrode/electrolyte interface. The rate performance of metal-ion batteries is determined by the rate-limiting step that in various cases is associated with the hindered ion transfer across resistive layers[5,7,8] due to the strong interaction between their components and alkali metal ion. Thereby, most research efforts should concern tuning SEI/CEI layer properties to enhance the ion transfer rate through surface films.

Generally, the alkali metal ion intercalation comprises the following steps[4,9,10] **1)** ion diffusion in the solution bulk; **2)** ion desolvation in the vicinity of the SEI(CEI)/electrolyte interface; **3)** ion transfer through surface layers **4)** ion adsorption at the electrode surface (an adion formation); **5)** surface diffusion of ion that may adjust phase transformation in electrode materials, e.g., lithium iron phosphate-based cathode composite $LiFePO_4$[11]; **6)** charge transfer across the electrode/SEI(CEI) interface; and **7)** ion solid state diffusion in the electrode lattice. If no passivating films are formed at the electrode surface, the intercalation scheme simplifies as step **3)** is missed and the ion desolvation occurs at the bare electrode/electrolyte interface.

**K⁺-ion battery**

The expected advantages of the emerging PIB technology have inspired intensive research activity in this field. The abundance of K in the Earth's crust, $K^+/K$ redox potential that is 0.09V more negative than that of $Li^+/Li$ in carbonate-based electrolyte, and higher ionic conductivity due to the smaller Stoke's radius of the $K^+$ ion compared to $Li^{+}$ [12] provide impetus for investigation of $K^+$-ion intercalation systems. Nevertheless, major drawbacks arising from the electrode instability (irreversible structural changes occurring, e.g., in graphite electrode[13]) and interfacial surface chemistry in $K^+$-systems have been reported[12,14]. The overwhelming problem stands in the large resistance detected at the cathode-electrolyte inter electrode/electrolyte interphase (CEI) in $K^+$-ion electrolytes whose origin is poorly understood[14,15]. Moreover, the primary methodological examination of electrode materials for $K^+$-ion batteries is typically performed in the K metal anode half-cells. In the most cases, the observed capacity fading in such K half-cells is mistakenly ascribed to the intrinsic problems of electrode materials such as surface reconstruction or bulk structure degradation. More probably the undesirable capacity decay may stem from the high charge transfer resistances of the K metal stripping/plating reactions[12], as well as from the formation of an unstable or highly resistive interfacial film on the K metal electrode surface upon electrolyte decomposition[14] due to high K metal reactivity. In total, the listed processes result in the large overpotential on the K metal anode and might become a reason behind the dramatic capacity fading of the half-cells[14,16]. However, all these problems involving the huge resistances of the CEI layer, the formation of the unstable SEI film on K metal surface and large charge transfer resistances of the K metal stripping/plating reaction and the resulting poor electrochemical performance can be at least partially avoided using proper choice of solvent-salt combinations which is the important outcome of this study. Since the ultimate selection of the electrolyte solution depends on both positive and negative electrodes utilized in $K^+$-ion system, the overview of most popular electrode materials for PIBs is presented below.

**Positive electrodes for PIBs**

The comprehensive review was composed by the research group of Komaba[17]. The positive electrode materials might be divided into several groups depending on their structure: layered transition metal oxides, Prussian blue analogues (PBAs), polyanionic compounds, and organic materials.

**Layered transition metal oxides $A_xMO_2$**

The structure of $\alpha$-NaFeO$_2$-type AMO$_2$ compounds is designed from MO$_2$ slabs comprising edge-sharing MO$_6$ octahedra and alkali metals in the interslab gaps. Polymorphism emerges when the MO$_2$ slabs are stacked with different stacking sequences along the *c*-axis direction. Herein, the

notation covering the corresponding O3-, P3- and P2- oxide types is described (Figure 2.1a). In the O3-type (α-NaFeO$_2$-type) structure, MO$_2$ slabs are disposed along the $c$-axis with cubic close-packed (ccp) oxygen sublattice corresponding to an AB CA BC array, while the alkali-metal ions are accommodated at the octahedral sites in the interslab space. Each hexagonal unit cell encompasses three MO$_2$ slabs. The "O" in O3 type denotes the octahedral sites where alkali-metal ions are located and the subsequent number "3" is the number of MO$_2$ slabs comprised in the hexagonal unit cell. Large K$^+$ ions generally prefer occupation of trigonal prismatic sites providing larger space than the octahedral ones, leading to formation of P-type layered oxides such as P3 and P2 (β-RbScO$_2$) types. In the P3-type layered oxide, alkali-metal ions accommodate the trigonal prismatic sites in the interslab space between the MO$_2$ slabs with the oxygen packing arrangement AB BC CA along the $c$-axis. There are three MO$_2$ slabs in the hexagonal unit cell. In the case of the unit cell distortion from the hexagonal symmetry, a prime symbol is added between the letter and the number; however, the number of MO$_2$ slabs is counted for a pseudohexagonal unit cell. In the P2-type layered oxide, alkali-metal ions occupy the prismatic sites with the oxygen packing arrangement AB BA AB along the $c$-axis.

The distinct difference in the structural stability of layered alkali metal oxides AMO$_2$ was elucidated via the correlation between the ionic radii of the alkali metal atoms ($R_{A+}$) and transition ($R_{M3+}$) metal atoms[18–21] and that between $R_{A+}$ and the ionicity of the A−O and M−O bonds[19,22]. The ionic radius of Li$^+$ in octahedral coordination (0.76 Å) is similar to those of the transition-metal ions[23]. Hence, the mixture of lithium ions with transition metal ions is more favorable to form cation disordered rock-salt-type (NaCl type) phases such as α- LiFeO$_2$. On the other hand, the Na$^+$ (1.02 Å) and K$^+$ (1.38 Å) ionic radii are larger than those of Li$^+$ and the transition metal ions, and consequently, no site-exchange occurs between them.
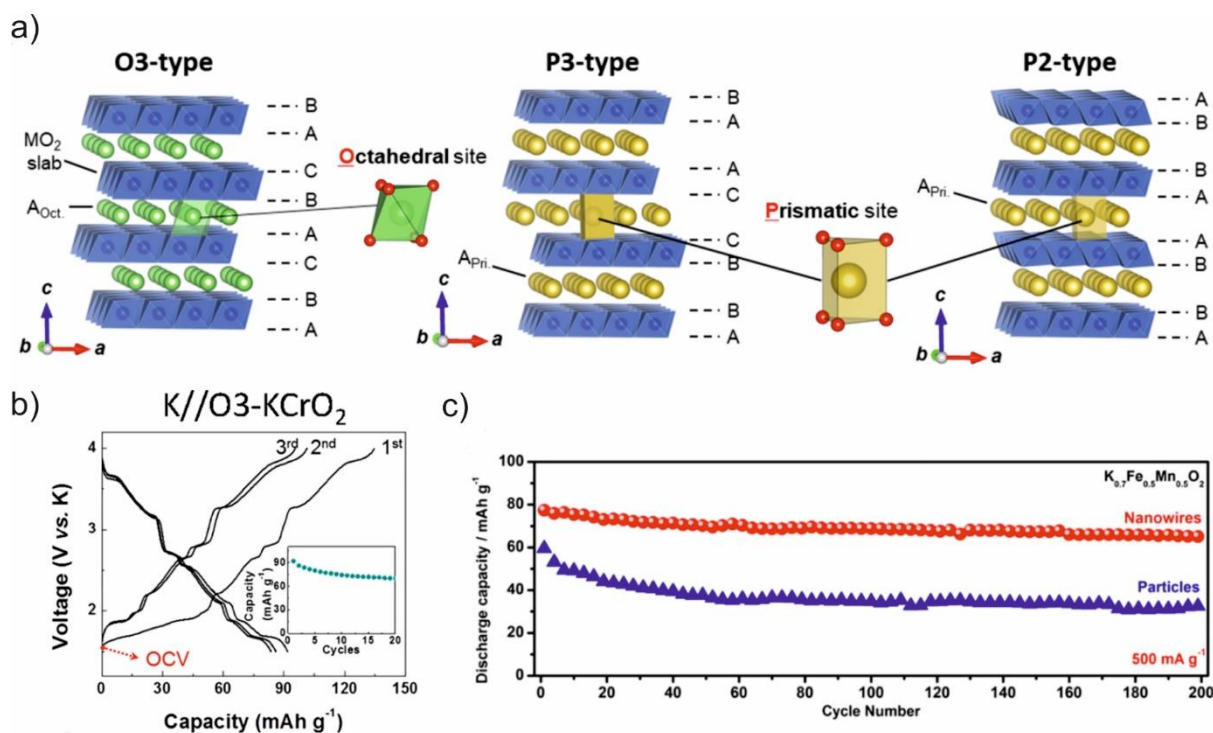
Figure 2.1. a) Schematic illustrations of the crystal structures of O3-, P3-, and P2-type $K_xMO_2$[17] b) galvanostatic profile of O3-$KCrO_2$ electrode in K cell[24] c) cycle performance of the P3-$K_{0.7}Fe_{0.5}Mn_{0.5}O_2$-nanowire and P3-$K_{0.7}Fe_{0.5}Mn_{0.5}O_2$-particle electrodes in K cell [25]

The only reported O3-$K_xMO_2$ are $KScO_2$[26] and $KCrO_2$[27]. The former having the electron configuration $[Ar]4s^03d^0$ should be electrochemically inactive as O3-$NaScO_2$[21]. The latter exhibited good cycle stability and a reversible capacity of ~90 mA·h·g$^{-1}$ with stepwise voltage profile in the range of 4.0− 1.5 V vs K$^+$/K[24] in K cells (Figure 2.1b) that arises from the complicated structural changes (O3−O′3-P′3−P3−P′3−P3−O3 for $1 > x > 0.4$ in $K_xCrO_2$).

Two nonstoichiometric Mn-containing layered oxides P′2-type $K_{0.3}MnO_2$[28–30] and P3-type $K_{0.5}MnO_2$[31] are reported while the stoichiometric oxide $KMnO_2$ possesses the nonlayered structure consisting of chains of $[MnO_5]$ edge-sharing square-pyramids[32]. The K content $x$ might alter the structural type of $K_xMO_2$ obtained via the solid-state reaction. The synthesized anhydrous P′2-type $K_{0.3}MnO_2$ exhibited an orthorhombic lattice with the space group $Cmcm$[29,30] and delivered a reversible capacity of ~70 mA·h·g$^{-1}$ in 1.5−3.5 V vs K$^+$/K and ~130 mA·h·g$^{-1}$ in the extended potential range of 1.5−4.5 V vs K$^+$/K in three-electrode K-half cells[28]. While larger capacities stemmed from higher upper cutoff potentials, the capacity retention was visibly declined. In contrast, the restricted potential range of 1.5−3.5 V vs K$^+$/K resulted in better capacity retention without structural degradation. The layered P3-type $K_{0.5}MnO_2$ oxide with a rhombohedral lattice (the space group $R3m$) delivered a reversible capacity of ~100 mAh g$^{-1}$ in 1.5− 3.9 V vs K$^+$/K in a K half-cell[31]. The performed *in situ* XRD measurements for P′3-$K_{0.5}MnO_2$ support that structural

changes from the P3- to the O3-type phase occurred via a two-phase reaction for $0.425 > x > 0.395$ in $K_xMnO_2$ and from the O3- to O3-like-phase (a phase with larger slab spacing preserving O3-stacking[31]) via a two-phase reaction for $0.364 > x > 0.316$ in the K deintercalation process[31]. Particularly, the irreversible migration of transition metals from the slab into the interslab is less beneficial compared to the transition metal migration in the Li and Na systems. The inverse structural changes were detected on K intercalation during discharge confirming a reversible K (de)intercalation from/into the framework of P3-$K_xMnO_2$ structure in the voltage range of $1.5-3.9$ V vs $K^+/K$. The stacking faults and defects occurred in the structure during K extraction at $x > 0.27$ in $K_xMnO_2$, resulting in less stepwise voltage profile and capacity fading during cell cycling.

$K_xCoO_2$ compounds crystallize in P′2- and P3- type structures[33,34]. Both P2- and P3-$K_{1-x}CoO_2$ delivered the reversible capacities of $\sim 60$ mA·h·g$^{-1}$ and $\sim 70$ mA·h·g$^{-1}$ in the potential ranges of $2.0-3.9$ V vs $K^+/K$ and $1.5-3.9$ V vs $K^+/K$, respectively[35]. The $K^+$ ions occupy the large prismatic sites instead of octahedral sites compared to small $Li^+$ ions, providing larger interslab distances during the charge and discharge processes. The low-voltage operation of both P2- and P3-$K_{1-x}CoO_2$ electrode materials would stem from the elongated Co−O distances compared to $LiCoO_2$. The stepwise shape of voltage profile probably originates from $K^+$/vacancy ordering.

Various binary and ternary transition metal systems (including p-block elements) have been reported[25,36–39] compared to the limited single transition metal systems that were described above. Both the P2-$K_{0.7}Fe_{0.5}Mn_{0.5}O_2$ nanoparticles[36,37] and P3-$K_{0.7}Fe_{0.5}Mn_{0.5}O_2$ nanowires[25] deliver reversible capacities exceeding 170 mA·h·g$^{-1}$ with good cycle stability in the potential range of $1.5-4.0$ V vs $K^+/K$ (Figure 2.1c). The enhanced capacity values originate from the specific particle size and morphology, while smaller reversible capacities and poor rate performances were observed for the micrometer-sized P2-$K_{0.65}Fe_{0.5}Mn_{0.5}O_2$[37] and P3-$K_{0.7}Fe_{0.5}Mn_{0.5}O_2$[25] (Figure 2.1c). The micrometer-sized particles P3-$K_{0.54}Co_{0.5}Mn_{0.5}O_2$ delivered the reversible capacity value of 120 mA·h·g$^{-1}$ and 100 mA·h·g$^{-1}$ in K half-cell and full cell with hard carbon negative electrode, respectively[38].

Multiple transition-metal systems utilizing the partial replacement with redox-inactive metals such as Mg, Cu, Zn, and Te, residing the $MO_2$ slab, tune the $K^+$ ions and vacancy ordering in the interslab and, thus, diminish the voltage steps[40]. The P2-$K_{2/3}Ni_{2/3}Te_{1/3}O_2$ electrode delivered a reversible capacity value of 65 mA·h·g$^{-1}$. While replacing $Ni^{2+}$ with $Zn^{2+}$ in the P2-$K_{2/3}[Ni_{1/2}Zn_{1/6}Te_{1/3}]O_2$ results in a higher reversible capacity value of 75 mA·h·g$^{-1}$ but with decreased capacity retention due to the contributions of the oxide ion redox reaction during (de)intercalation.

The potassium layered oxides exhibit the inferior working potential compared to those of PBAs and polyanionic compounds that are described below.

**Prussian Blue Analogues (PBAs)**

There exists vast diversity of Prussian Blue Analogues (PBAs) comprising various transition and alkali/alkali earth metals. The chemical formulas of PBAs are depicted as $A_xM1[M2(CN)_6]_y \cdot nH_2O$ ($0 \leq x \leq 2$, $y \leq 1$), where A is an alkali or alkali earth metal, and M1 and M2 can be various metals such as Ti, V, Cr, Fe, Co, Ni, Cu, and Zn. The reduced Prussian Blue $AFe[Fe(CN)_6]$, i.e., all the $Fe^{3+}$ ions are reduced to $Fe^{2+}$ ions and, thus, the alkali (x = ~2) or alkali earth (x = ~1) metal content is enhanced, is called Prussian White $A_2Fe[Fe(CN)_6]$. Generally, the discussion of PBAs also includes Prussian white compounds. A typical PBA crystal structure has a 3D open-framework comprising corner-connected octahedra $M1N_6$ and $M2C_6$ (Figure 2.2a)[41]. Ordinarily, the PBAs have a cubic structure (space group *Fm-3m*) with the correspondingly arranged octahedra. However, the incorporated cations and molecules may promote the octahedra rotation with the subsequent structural transformation to monoclinic (space group *P2₁/n*) or rhombohedral (space group *R-3m*) distorted PBAs (Figure 2.2b). The PBA structure with open 3D channels facilitates the intercalation and diffusion of alkali metal ions with large size like $K^+$. Indeed, PBAs possess the electrochemical activity in all alkali metal ion systems ($Li^+$, $Na^+$, and $K^+$)[42,43]. K-poor PBAs exhibit a cubic structure, while K-rich PBA compounds tend to possess monoclinic structures, regardless of the drying conditions[44–46], due to the large $K^+$ ionic radius. The increased value of the Pauli repulsion prevents the lattice shrinkage[47], and the formation of a rhombohedral lattice with a smaller volume than that of the monoclinic phase.
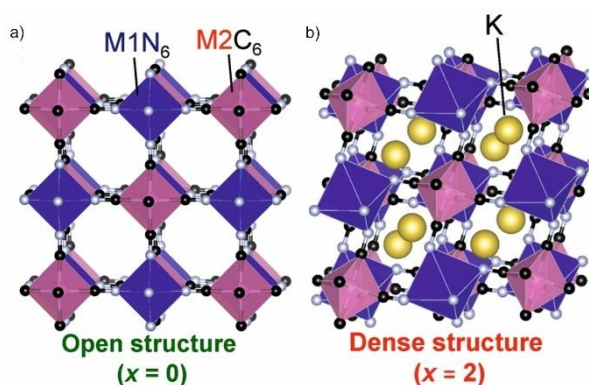


Figure 2. 2 Crystal structures of PBAs: (a) cubic and (b) rhombohedral; the blue and pink polyhedra depict $M1N_6$ and $M2C_6$, while the yellow spheres represent K metal[17]

Another characteristic feature of PBAs is the difference in the spin states of the transition metals in the $M1N_6$ and $M2C_6$ octahedra depending on the ligand field. For instance, the transition metals Fe and Mn have the high-spin (HS) M1 in the $M1N_6$ octahedron, and the low-spin (LS) M2 in the $M2C_6$ octahedron owing to their respective weak N-coordinated and strong C-coordinated ligand fields[48].

The electrochemical performance of the PBA electrodes is summarized in the table 2.1. Most of PBAs compounds are studied as positive electrodes whereas only $Co_3[Co(CN)_6]_2$ refers to the negative electrode. Besides, $K_2Zn_3[Fe(CN)_6]_2$ possesses the structure different from PBAs. Conventionally, electrochemical properties of PBAs are contingent on transition metals; $[Fe(CN)_6]$ vacancies (due to the significantly declined number of electroactive redox $Fe^{2+}$ centers in vacancy-rich materials); particle size; K and interstitial water contents.

Table 2.1. Summary of the electrochemical properties of PBAs in PIBs.

| Electrode material | Specific capacity, $mA \cdot h \cdot g^{-1}$ | Average discharge voltage, V vs $K^+/K$ | Reference |
|---|---|---|---|
| $K_xFe[Fe(CN)_6]$ thin film | 79 | 3.7 | [49] |
| $rGO@K_xFe[Fe(CN)_6]@steel$ | 97 | 3.1 | [50] |
| $K_xFe[Fe(CN)_6]$ | 111 | 3.5 | [51] |
| $K_xCo[Fe(CN)_6]$ | 60 | 3.3 | [51] |
| $K_xNi[Fe(CN)_6]$ | 64 | 3.6 | [51] |
| $K_xCu[Fe(CN)_6]$ | 35 | 3.2 | [51] |
| $KFe[Fe(CN)_6]$ | 119 | 3.5 | [52] |
| $K_{1.92}Fe[Fe(CN)_6]_{0.94} \cdot 0.5H_2O$ | 128 | 3.6 | [46] |
| $K_{1.89}Mn[Fe(CN)_6]_{0.92}$ | 142 | 3.6 | [45] |
| $K_{1.75}Mn[Fe(CN)_6]_{0.93} \cdot 0.16H_2O$ | 141 | 3.8 | [44] |
| $K_{0.220}Fe[Fe(CN)_6]_{0.805} \cdot 4.01H_2O$ | 78 | 3.1 | [53] |
| $K_{0.3}Ti_{0.75}Fe_{0.25}[Fe(CN)_6]_{0.95} \cdot 2.8H_2O$ | 138 | 2.3 | [54] |
| $K_2Zn_3[Fe(CN)_6]_2$ | 67 | 3.7 | [55] |
| $Co_3[Co(CN)_6]_2$ | 366 | 0.6 | [56] |

The choice of transition metal in PBAs alters the values of operating voltages and reversible capacities. Figure 2.3 illustrates the charge−discharge curves of PBAs with various transition metals: $K_{1.63}Fe[Fe(CN)_6]_{0.89}$ (KFFCN), $K_{1.75}Mn[Fe(CN)_6]_{0.93}$ (KMFCN), $K_xNi[Fe(CN)_6]$ (KNFCN), $K_xCu[Fe(CN)_6]$ (KCuFCN), $K_xCo[Fe(CN)_6]$ (KCoFCN), and $K_{0.3}Ti_{0.75}Fe_{0.25}[Fe(CN)_6]_{0.95} \cdot 2.8H_2O$ (KTFCN)[44,51,54]. Ni-, Cu- and Co-based PBAs exhibit capacity values in the range of 30−70 $mA \cdot h \cdot g^{-1}$ attributed to a one-electron LS $Fe^{2+/3+}$ redox process, whereas $Ni^{2+}$, $Cu^{2+}$, and $Co^{2+}$ remain electrochemically inactive. Conversely, Fe-, Mn- and Ti-based PBAs reveal high specific capacity values in the range 130−140 $mA \cdot h \cdot g^{-1}$, corresponding to a two-electron redox process comprising both LS $Fe^{2+/3+}$ and HS $M^{2+/3+}$ ($Fe^{2+/3+}$

or Mn $^{2+/3+}$ or likely Ti$^{2+/3+}$) redox reactions. The capacity gathered in the range of 3.75−4.0 V vs K$^+$/K corresponds to the redox of LS Fe$^{2+/3+}$. However, the redox potential of HS transition metals varied greatly depending on their nature. Accordingly, the redox of HS Mn$^{2+/3+}$ occurs at high potentials >4 V vs K$^+$/K, while HS Fe$^{2+/3+}$ and Ti$^{2+/3+}$ occurred at values of 3.3 and ≤2.0 V vs K$^+$/K, respectively. Therefore, Mn-based PBAs seem to be an attractive cathode material for PIBs with the enhanced energy density. Furthermore, PBAs reveal excellent long-term cycle stability. For instance, K$_x$Mn[Fe(CN)$_6$]$_y$·zH$_2$O (KMFCN) show capacity retention values >90% after 350 cycles in 7 mol kg$^{-1}$ potassium bis(fluorosulfonyl)amide (KFSA) in 1,2-dimethoxyethane (DME) electrolyte solution[57].

The operando XRD study of the structural evolution of monoclinic K$_x$Mn[Fe(CN)$_6$]$_y$·zH$_2$O reveals a reversible transition from the monoclinic to the cubic structure in the lower voltage plateau via a two-phase reaction where K content changes in the range of x = 2−1[44]. The further transition occurs from the cubic to tetragonal structure in the higher voltage plateau (K content varies in the range of x =1−0)[44]. These structural transformations are accomplished with volume changes of +14.4 and −6.0% for the monoclinic to cubic and cubic to tetragonal transitions respectively.

The proper particle size selection may tune the electrochemical properties of PBA-based cathodes. For instance, K$_x$Fe[Fe(CN)$_6$]$_y$·zH$_2$O (KFFCN) exhibits the substantial difference in electrochemical performance depending on particle sizes[58]. The small KFFCN cubes with the average size ∼20 nm demonstrate a high reversible discharge capacity of 140 mA·h·g$^{-1}$ in the K cell, while large KFFCN cubes with the size >1.5 μm show a poor capacity value of ∼10 mA·h·g$^{-1}$. The low discharge capacity value of KFFCN with large particle size could be tentatively ascribed to the slow solid state diffusion of K$^+$ ions in the KFFCN host. However, the morphology design[59] and transition metal change[60,61] may alleviate the slow K$^+$ ion diffusion in PBA framework for future use of large PBA particles.

Thereby, high specific capacity and redox potential values resulting in high energy densities, together with the easy scalable and low-cost compound production, result in reasoned option of KMFCN as the encouraging cathode material for PIBs. Nevertheless, despite their splendid electrochemical performances, PBAs possess several disadvantages: the low tap density, the low electronic conductivity due to their open 3D framework structure and chemical-bond character and insufficient thermal safety in case of a short circuit. The cyanide groups are released as toxic cyanides above 200 °C, which also exothermically react with the electrolyte and cause the runaway[62]. However, the tap density value might be enhanced via spray drying within thermal stability of PBA material, the electronic conductivity might be increased via addition of carbon

nanotubes to electrode composite and, finally, the suppression of CN groups emission might be attained via the utilization of additive acting as scavenger.
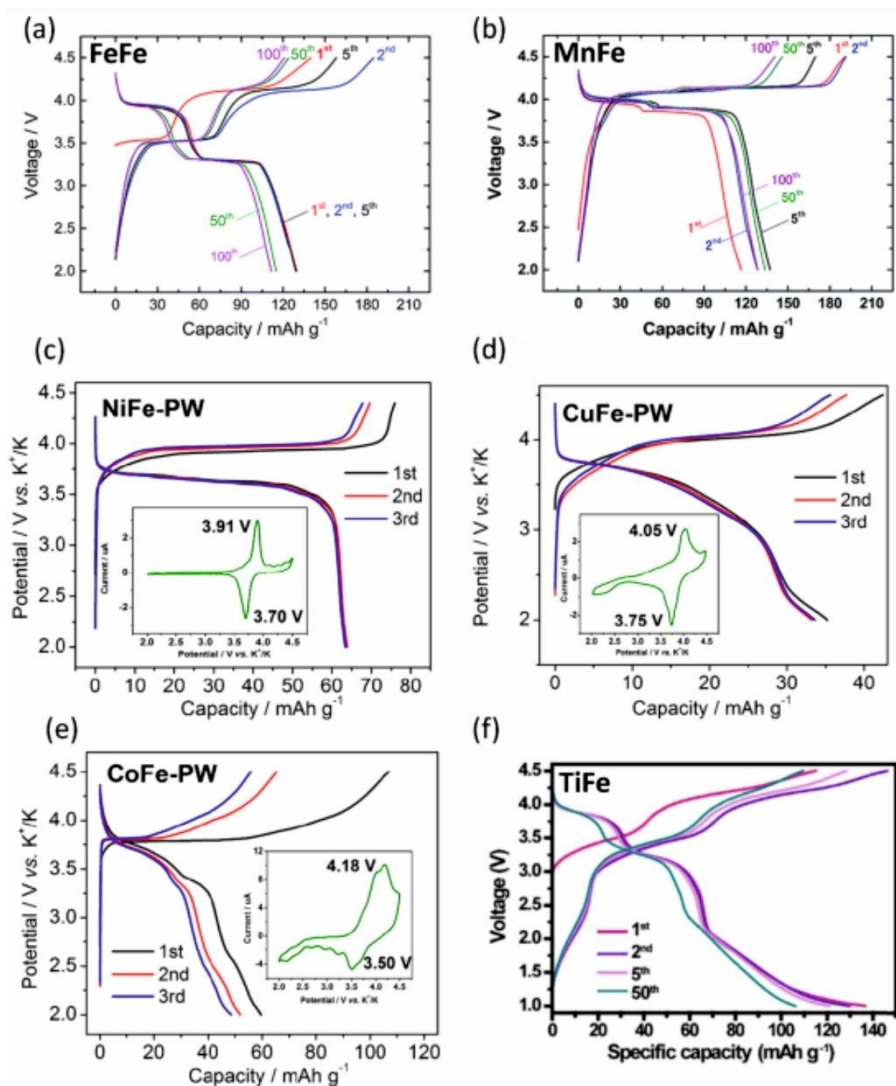


Figure 2.3. Charge−discharge curves of PBAs in K cells: (a) KFFCN[44]; (b)KMFCN[44]; (c) KNFCN[51], (d) KCuFCN[51]; (e) KCoFCN[51]; and (f) KTFCN[54].

**Polyanionic compounds**

Similarly to PBAs, polyanionic compounds possess 3D open framework structures comprising $MO_x$ (where M = transition metals) and $(XO_4)_n$ (where X = P, S, Mo, W, As and Si) polyhedra. This open structure facilitates fast diffusion of $K^+$ ions. Furthermore, polyanionic structures deliver the enhanced redox potential that arises from decreased covalency of the M−O bonds due to the highly covalent X−O bonds. The more electronegative element X, the more covalent X−O bond. This phenomenon was proposed by Manthiram and Goodenough in the field of energy storage materials and called "the inductive effect"[63,64].

Primarily, the potassium-based polyanionic compounds similar to their lithium and sodium counterparts were studied as positive electrodes for PIBs. However, a number of structures was

observed not to be thermodynamically stable like triphylite $KFePO_4$ (olivine-type structure). Others like $KFePO_4$ (SG $P2_1/n$), $KMnPO_4$, $KFeP_2O_7$, $KCrP_2O_7$, and $K_2MnP_2O_7$ appeared to be electrochemically inactive[65,66].

Three kinds of pyrophosphate, $KTiP_2O_7$, $KMoP_2O_7$ and $KVP_2O_7$, with structure related to $KAlP_2O_7$ (SG $P2_1/c$) have demonstrated the reversible $K^+$-ion intercalation, exhibiting reversible capacities of 22, 25, and 54 $mA \cdot h \cdot g^{-1}$ at 50 °C, respectively[66]. On the other hand, the Fe- and Mn-based pyrophosphates $KFeP_2O_7$ and $K_2MnP_2O_7$ occur to be electrochemically inactive.

Some vanadium-based fluorophosphate and oxyphosphate compounds, such as $K_3V_2(PO_4)_2F_3$, $KVPO_4F$ and $KVOPO_4$, have also been studied as positive electrodes for PIBs. $K_3V_2(PO_4)_2F_3$ have demonstrated the reversible capacity values >100 $mA \cdot h \cdot g^{-1}$ and the good capacity retention of 95% upon 180 charge/discharge cycles. Its crystal structure is built up of $VO_4F_2$ octahedra and $PO_4$ tetrahedra. The volume change has not exceeded 6.2% during $K^+$-ion (de)intercalation. Both $KVPO_4F$ and $KVOPO_4$ compounds have a $KTiOPO_4$ (KTP)- type structure (SG $Pna2_1$), consisting of corner-sharing $VO_4F_2$/ $VO_6$ octahedra and $PO_4$ tetrahedra. KTP-type structures provide appropriately large channels that alleviate the $K^+$-diffusion. $KVPO_4F$ and $KVOPO_4$ have exhibited the reversible capacity values of ~92 and 84 $mA \cdot h \cdot g^{-1}$ , respectively, and high redox potential values ~4 V *vs* $K^+$/K. Orthorhombic $KFeSO_4F$ with a KTP-type structure has exhibited a capacity value of 110 $mA \cdot h \cdot g^{-1}$ in the first cycle and a capacity retention of 78% upon 20 cycles[65].

The electrochemical properties of polyanionic compounds in K cells are summarized in Table 2.2. Vanadium-based phosphates and fluorophosphates have demonstrated good electrochemical performances in terms of capacity value and operating potential[66–69]. However, the utilization of expensive and toxic elements (V) would hinder the future implementation of PIB. So, the abundant and nontoxic elements such as Fe and Mn are more preferable.

Table 2.2. Summary of electrochemical properties of polyanionic materials for PIBs

| Electrode material | Specific capacity, $mA \cdot h \cdot g^{-1}$ | Average discharge voltage, V vs $K^+$/K | Reference |
|---|---|---|---|
| $KVPO_4F$ | 90 | 4.13 | [67] |
| $KVOPO_4$ | 80 | 4 | [67] |
| $KVP_2O_7$ | 61 | 4.15 | [66] |
| $K_3V_2(PO_4)_3$ | 54 | 3.5 | [68] |
| $K_3V_2(PO_4)_2F_3$ | 104 | 3.7 | [69] |

| heterosite FePO$_4$ | 120 | 2.3 | 65 |
|---|---|---|---|
| K$_2$FeP$_2$O$_7$ | 60 | 2.7 | 65 |
| orthorhombic KFeSO$_4$F | 100 | 3.6 | 65,70 |
| monoclinic KFeSO$_4$F | 50 | 3.4 | 65,71 |
| KMoP$_2$O$_7$ | 25 | 2.5 | 66 |

**Organic compounds and metal-ion frameworks**

Other materials explored as cathodes for PIBs are constituted of organic molecules and polymers with carbonyl groups as redox centers. Poly(anthraquinonyl sulfide) (PAQS) delivers a reversible capacity value of $\sim$190 mA·h·g$^{-1}$ in K cell with electrolyte solution [potassium bis(trifluoromethanesulfonyl)- amide (KTFSI) in the mixture of dioxolane and DME] at a current rate of 20 mA·g$^{-1}$ ($\sim$0.1C)[72]. The mechanism of K$^+$-ion storage in the PAQS electrode is depicted in Figure 2.4a. The two voltage plateaus at the charge−discharge profile at 1.5 V and 2.1 *vs* K$^+$/K correspond to the two step (de)insertion of K$^+$ ions (Figure 2.4b). However, PAQS electrode dissolution in electrolyte leads to the reduced cycle stability.

Perylene-3,4,9,10-tetracarboxylic dianhydride (PTCDA) exhibits a reversible capacity value of 120 mA·h·g$^{-1}$ at operating potential of $\sim$2.4 V vs K$^+$/K at low current density (Figure 2.4c)[73]. However, PTCDA suffers from the substantial capacity decay due to the low electronic conductivity and electrode dissolution in the electrolyte. But the annealing the PTCDA powder at 450 °C results in the increased electronic conductivity value up to $5.3 \times 10^{-6}$ S m$^{-1}$ from $10^{-10}$ S m$^{-1}$ [74]. Furthermore, a reversible capacity value of 123 mA·h·g$^{-1}$ at 100 mA·g$^{-1}$ rate after 140 cycles is attained in K cell with concentrated electrolyte solution (3 mol kg$^{-1}$ KFSA/DME) (Figure 2.4d), owing to the suppressed PTCDA dissolution accomplished with the reduced amount of free solvent molecules.

Oxovanadium oxalate phosphates with the general formulas A$_2$[(VO)$_2$(HPO$_4$)$_2$(C$_2$O$_4$)] and A$_2$[(VO)$_2$(HPO$_3$)$_2$(C$_2$O$_4$)] have also been examined as the electrodes for PIBs. Generally, these materials refer to the metal organic phosphates open framework (MOPOF). Their structure consists of [(VO)$_2$(HPO$_4$)$_2$(C$_2$O$_4$)]$_2$ layers with K$^+$ ions located in the interlayer space. However, they demonstrate a reduced specific capacity value and a poor Coulombic efficiency in K cells with conventional carbonate-based eletrolyte[75].

Thereby, most organic materials possess low charge/discharge potentials of ~2−2.5 V *vs* K$^+$/K leading to the decreased specific energy. Moreover, they suffer from the significant dissolution in electrolyte during battery operation resulting in the fast capacity decay. Besides, these electrodes require additional prepotassiation process for anodes, owing to the K absence in the positive electrode structure.
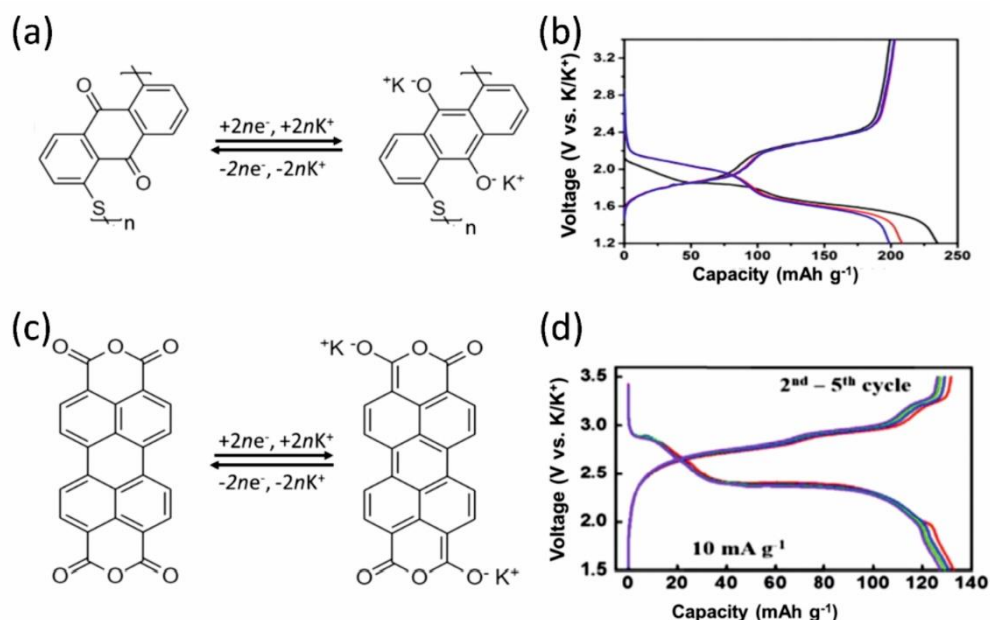


Figure 2.4. (a) Mechanism of reversible K$^+$-ion storage in PAQS[72]; (b) galvanostatic profile of PAQS for the initial three cycles in the voltage range of 1.5−3.4 V vs K$^+$/K at a current density of 20 mA·g$^{-1}$;[72] (c) Mechanism of K$^+$-ion storage in PTCDA[73]; (d) galvanostatic curves of PTCDA at the potential range of 1.5−3.5 V vs K$^+$/K at a current density of 10 mA·g$^{-1}$ [73]

In summary, K containing layered transition-metal oxides exhibit small specific capacity values, low operating potentials, and stepwise voltage profile arising from multiple phase transitions. In addition, organic compounds also demonstrate low operating potentials in K cells and suffer from the significant dissolution in electrolyte. Whereas, PBA electrodes deliver both high capacity values and operation potentials in K cells, due to their 3D frameworks with channels and interstitial sites suitable for fast K$^+$-ion diffusion. Similar to PBAs, polyanionic compounds with 3D open frameworks demonstrate high operation potentials.

**Electrolyte for PIBs**

Generally, the electrolyte is usually obtained by the dissolution of an alkali metal salt in a mixture of organic solvents. The ideal electrolyte exhibits high ionic conductivity and low viscosity combined with wide electrochemical stability window. PIB electrolytes often contain K salts and organic solvents (with additives). Popular K salts are KPF$_6$, KClO$_4$, KBF$_4$, KN(SO$_2$F)$_2$ (potassium bis(fluorosulfonyl)imide, KFSI) and KN(SO$_2$CF$_3$)$_2$ (potassium bis(trifluoromethanesulfonyl)imide, KTFSI). Carbonate ester (such ethylene carbonate (EC),

diethyl carbonate (DEC), dimethyl carbonate (DMC), propylene carbonate (PC)) and ether solvents (dimethoxyethane (DME); diethylene glycol dimethyl ether or diglyme) are often utilized in PIBs[12,17].

The solution structure influences the ion transport, electrolyte stability and electrochemical performance of a metal-ion battery. The DFT-molecular dynamics (MD) simulations of $KPF_6$/EC localized structures unveil typical solvation structure of $K^+$ ions[76]. It is not ascribed to a definite geometry due to the numerous coordinating oxygen atoms. Though $K^+$ ions prefer the coordination numbers of 8, a broader coordination number distribution is reported for $K^+$ ions compared to $Li^+$ ions[76]. So, $K^+$ ions might exhibit both higher coordination number and more disordered and flexible solvation structures, resulting in faster ionic diffusion in aprotic solvents.

The lower solubility of $K^+$ salts in organic solvents arises from the decreased solvation energies compared to $Li^+$ and $Na^+$[77]. The $K^+$-ion desolvation energy values calculated via the gas phase approximation varies in the range of 68.9 kJ·mol$^{-1}$-139 kJ·mol$^{-1}$ for 27 solvents involving carbonate esters and ethers. However, the reduced desolvation energy promotes faster desolvation process at the electrode − electrolyte interface[17]. Thereby, the $K^+$ desolvation process is more kinetically favorable compared to that in the $Li^+$- and $Na^+$-systems in aprotic solvents providing reliable reason to elaborate high-power PIBs. Albeit insufficient $K^+$-ion solvation leads to bare ions that bombard and, thereby, corrode the forming surface layers.

$KPF_6$-based electrolytes are more often utilized to examine both positive and negative electrodes for PIBs because $KPF_6$ salt possesses the electrochemical stability and provides the sufficient Al foil passivation to prevent current collector oxidation[17], whilst using the KFSI salt at the potentials > 4 V *vs* $K^+$/K results in the drastic Al foil corrosion[57]. Hereby, KFSI-based electrolytes are mainly utilized to probe negative electrode materials. Moreover, the binary-salt KFSI-$KPF_6$ solutions could be implemented to attain both stable SEI on graphite negative electrode and Al current collector stability[78]. $KClO_4$ and $KBF_4$ salts are rarely utilized as electrolytes for PIBs due to their low solubilities in organic solvents.

Electrolytes primarily contribute to the film formation on the electrode surface owing to the electrolyte decomposition. Solid-electrolyte interphase (SEI) and cathode electrolyte interphase (CEI) are formed on the negative and positive electrodes respectively resulting in the irreversible capacity loss. However, the formation of stable surface layers with high $K^+$-ion transport properties prevents further electrolyte reduction/oxidation and ensures the sustainable battery performance. Two approaches may be applied to attain stable SEI/CEI formation together with the sufficient $K^+$-ion solvation tuning the composition of electrolyte solution: the additional of special functional compound, named as "electrolyte additive", in moderate quantities and the increase in the salt concentration[79].

**Electrolyte additives**

Electrolyte additives are successfully utilized in metal-ion batteries resulting in improved electrode kinetics due to the formation of less resistive and stable passivation films[80,81]. Various compounds such as vinylene carbonate (VC), fluoroethylene carbonate (FEC), 1,3-propane sultone (PS), etc.[82,83] have been examined as the electrolyte additives improving the electrode performance in Li-ion batteries. To date, the deficient number of studies on electrolyte additives for PIBs have been reported. VC and FEC are most widely implemented in the metal-ion batteries over last two decades. A small FEC concentration (<2 wt%) was examined in K cells with PBA cathode since PBA electrodes exhibit large irreversible capacity in a K cell at high potentials[44,46,58]. The FEC addition enhances the CE values from <60% up to 90%, albeit this increases K cell polarization[44,46]. Furthermore, the elaborated cycle performance is reported owing to suppressed irreversible side reactions[44,58]. However, FEC stimulates the electrolyte decomposition and other side reactions at potentials below 2 V $vs$ $K^+$/K resulting in larger electrode polarization and fast capacity fading in PIBs[44,84]. The poor published data provokes the meticulous study of effective electrolyte additives for PIBs

**Concentration effect**

The use of highly concentrated electrolytes ( >3 M) leads to the preferential formation of stable $FSI^-$-derived SEI[57,74,85–87]. The reversible dendrite-free plating/stripping of a K-metal was reported in [5 M KFSI/DME] electrolyte solution owing to $FSI^-$-derived surface films[85]. Fan et al. demonstrated the advantages of concentrated ether-based electrolyte [3 M KFSA/DME] over conventional carbonate-based electrolyte [0.8 M $KPF_6$/EC:EMC(1:1,v:v)] for the anodes based on carbon with oxygen defects[86]. 3.9 M KFSI/DME electrolyte provides the stable cycling of graphite anode in a K half-cell and K full cell with PBA positive electrode[57]. The K half-cell delivers a specific discharge capacity value of 260 mA·h·$g^{-1}$ and high initial CE value >80%.

The 3 M KFSI/DME electrolyte enables prominent cycle stability without significant capacity loss over 14000 cycles at high current density of 2000 mA·$g^{-1}$ (Figure 2.5a), while [0.8 M $KPF_6$/EC:EMC(1:1,v:v)] electrolyte with conventional concentration delivers poor capacity retentions of <50% within 500 cycles. XPS characterization of formed surface layers reveals the different SEI composition depending on the electrolyte choice. Figure 2.5b-e illustrates the high-resolution C1s, O1s, S2p, and N1s XPS spectra of the carbon electrodes retrieved upon 50 cycles. In concentrated ether-based electrolyte [3 M KFSA/DME] the electrode surface is primarily composed of inorganic salts derived from $FSI^-$ anions. The S2p and N1s spectra indicate the presence of $K_2SO_4$-, $K_2S$-, and N-containing products originating from KFSI-salt decomposition. Although the C1s XPS spectrum demonstrates peaks attributed to >C=O and C−O−C bonds owing to the DME decomposition. The broad peaks assigned to $KHCO_3$/ROCOOK, >C=O/$K_2CO_3$, and

37

C−O−C bonds are observed for the electrodes cycled in [0.8 M KPF$_6$/ EC:EMC(1:1,v:v)]. The O1s XPS spectrum supports the presence of RO−COOK and RO-K arising from EC and EMC decomposition. These variety in SEI formation is likely due to the different reduction potentials of salts and solvents (KFSI, DME, KPF$_6$, EC, and EMC).
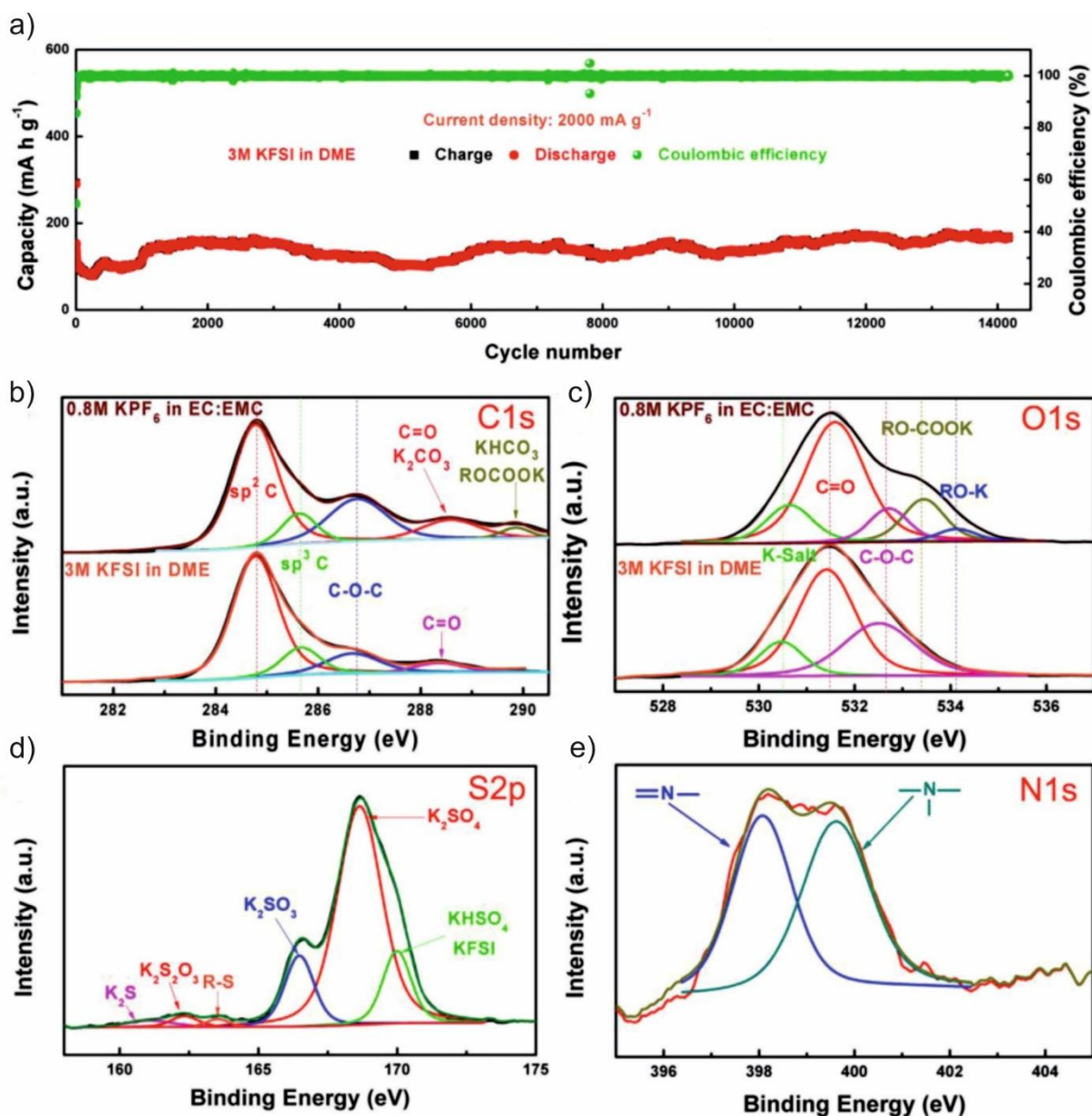


Figure 2.5. a) Cycle performance of the carbonaceous electrode in K cell with [3 M KFSI/DME] at 2000 mA·g$^{-1}$ current density; b) high-resolution C1s and d) O1s XPS curves of the carbonaceous electrode retrieved upon 50 cycles in K cells with [3 M KFSI/DME] or [0.8 M KPF$_6$/EC:EMC(1:1,v:v)]; e) high-resolution S2p and f) N1s XPS curves of the carbonaceous electrode in K cell with [3M KFSI/ DME][86].

**Remark on HOMO-LUMO Notation concerning electrolyte stability**

A prevalent number of publications in the metal-ion battery literature associate the energy difference of unoccupied molecular orbital (LUMO) and highest occupied molecular orbital

(HOMO) of the solvent to the electrochemical stability window. This widespread misconception implicates that the electrolyte is reduced at electron energies higher than LUMO and the electrolyte is oxidized at electron energy levels lower than HOMO. However, electrolyte stability is much more complex issue, concerning not only the redox potentials of the solvent, but also both other reactions of electrolyte solution components and the surfaces of the electrode materials.

Peljo et al. elucidated that the HOMO – LUMO concepts in terms of electrochemical stability window should be avoided[88]. The HOMO and LUMO notation is deduced from approximated electronic structure theory considering the electronic properties of isolated molecules. Hence, the energy levels of HOMO and LUMO do not correspond to the electrochemical potentials of species participating in sophisticated reactions during the battery operation. By contrast, electrochemical potentials are connected to the Gibbs free energy difference of the products and reactants. Figure 2.6 illustrates the importance of the comparison of the Fermi levels for the electron in the electrode and in solution for the redox couples restricting the stability of the electrolyte. The bright example is the case of pure water, in which the redox couple for the reduction is $H_2O/H_2$ and that for oxidation $O_2/H_2O$ that limits the electrochemical stability window to 1.23 V instead of ~8.7 V derived from electronic structure theory and corresponding to the water band gap[88].
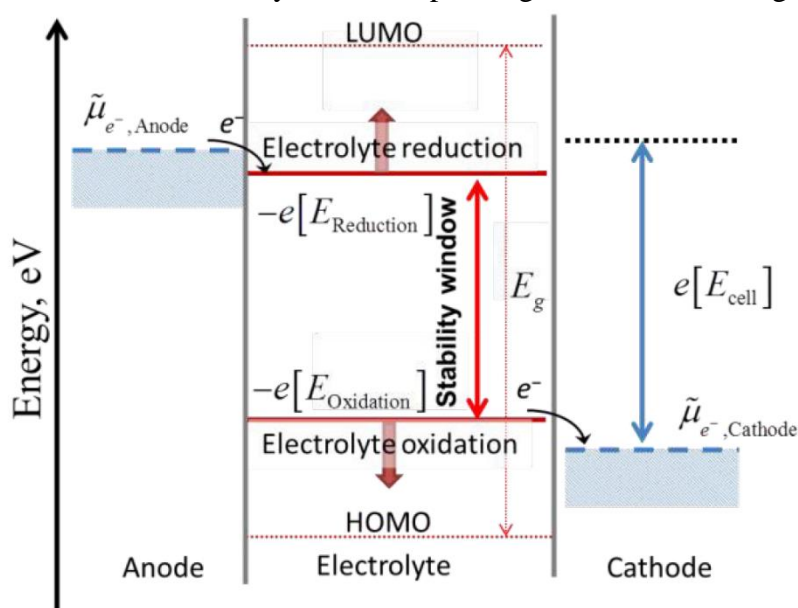


Figure 2.6. Notation for the negative and positive potential limits indicating the electrolyte stability and the energy levels of HOMO and LUMO suggested by Peljo et al.[88].

**Negative electrodes for PIBs**

Generally, the wide diversity of materials (carbonaceous compounds, K-alloying materials, oxides, chalcogenides, polyanionic compounds, and organic materials) are reported as the negative electrode for PIBs[17]. However, the carbonaceous materials attract most research interest as

negative electrodes for PIBs due to delivering high specific discharge capacity values, the feasibility for fast reversible K^{+}-ion (de)intercalation and the simplicity of production methods.

**Graphite**

Graphite consists of stacked graphene layers bonded by weak van der Waals interactions. The carbon atoms within the layer form planar hexagonal structure with $sp^2$ hybridization (Figure 2.7a,c). The stacking sequence of graphene layers displays an ABAB order along the *c*-axis with an interlayer distance of 3.354 Å (Figure 2.7a,c). Conventionally, graphite powder possesses a surface area value of <20 $m^2 \cdot g^{-1}$.

The graphite electrode exhibits the reversible intercalation of K^{+}-ions in K cells[13,89,90]. The observed reversible capacity values in the range of 240−260 mAh g^{−1} correspond to the theoretical capacity of 279 mAh g^{−1} assuming the formation of $KC_8$ intercalation compound. Galvanostatic charge-discharge curves exhibit the stepwise potential changes indicating the stage transformation of potassium intercalated graphite host. Generally, the notation of "stages" is utilized to describe the forming graphite intercalation compounds (GICs): "the stage ***n***" designates the ***n***th stage with a number ***n*** of graphene layers between the two closest intercalated layers". At least the three pair of reduction/oxidation peaks are obtained at 0.14/0.29 V, 0.20/0.46 V, and 0.28/0.58 V vs K^{+}/K respectively at the differential charge−discharge profile during intercalation/deintercalation processes[17] (Figure 2.7e). The stage 1 $KC_8$ structure is apparently formed at the end of the reduction process[13,89,90] and is illustrated in Figure 2.7b,d. During K^{+} -ion insertion between graphene layers the stacking sequence alters into A|A for the intercalated sheets accompanied by the increase in the interlayer distance up to~5.3 Å.[90] $KC_8$ possesses the orthorhombic symmetry with the layer sequence AαAβAγAδA along the *c*-axis, where α, β, γ, and δ denote the K layers with the identical K^{+}-ion distribution within the plane but with a different stacking order (Figure 2.7d).
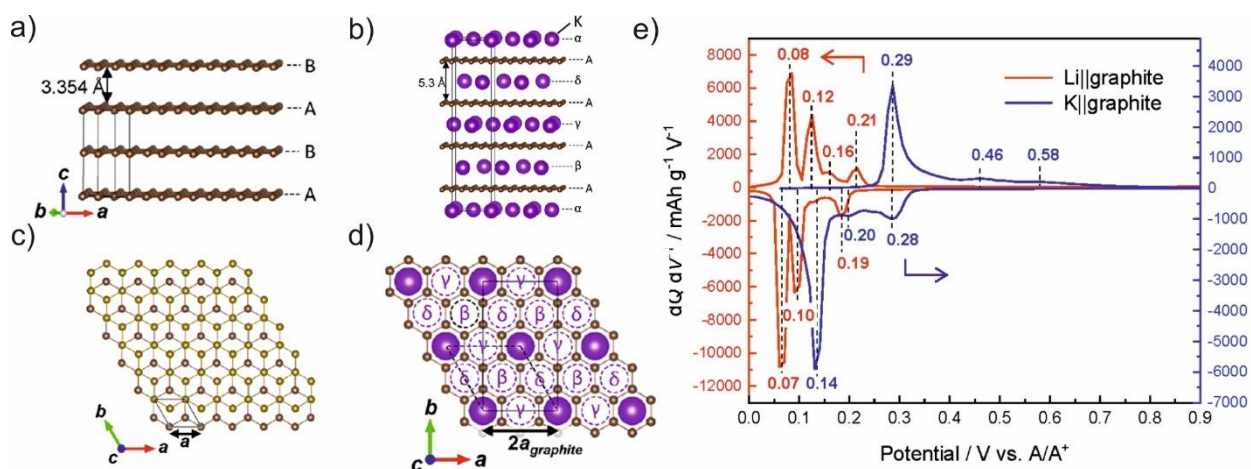


Figure 2.7. In-plane and side views of (a,c) graphite structure and (b,d) potassiated graphite $KC_8$; (e) Differential charge−discharge curves of the graphite electrode in a Li cell with 1 M

LiFSI/EC:DEC (1:1, v/v; red curve) and K cell with 1 M KFSI/EC:DEC (1:1, v/v; blue curve) at a current density of 12.4 and 9.3 mA·g$^{-1}$ respectively[17]

Operando XRD measurements reveal the transformation sequence of potassium GICs within the K$^+$-ion intercalation in graphite in the ester-based electrolyte implied graphite → disorderly stacked high stage (KC$_{96}$) → stage 4L - stage 3L (KC$_{96}$/KC$_{24}$) → stage 2L(2) (KC$_{28}$/KC$_{24}$) → stage 1 (KC$_8$). The reverse K$^+$-ion deintercalation occurs in order stage 1 (KC$_8$) → stage 2 (KC$_{16}$) → (stage 2L (KC$_{24}$/KC$_{28}$)) → stage 3L (KC$_{24}$/KC$_{42}$) → stage 4L(KC$_{36}$/KC$_{56}$) → disorderly stacked high stage (KC$_{96}$) → graphite[90]. "L" denotes the "liquid-like" distribution of K atoms between graphene layers (implying the absence of visible K atoms ordering in the (a,b)-plane). Figure 2.8 illustrates the scheme of the proposed graphite structure evolution. The K$^+$-ion intercalation process starts with the formation of disorderly stacked high stage with the approximate composition ~KC$_{96}$ by gliding of graphene layers to approach A|A or B|B stacking. Figure 2.8 depicts the resulted graphite structure as stacked empty and filled interlayers according to Rüdorff–Hofmann model[91]. Probably, at this stage K$^+$ ions heterogeneously accommodate positions into the graphite framework constituting locally potassium GICs layers with the disordering along the c-axis. Further K$^+$ intercalation produces stages 4L–3L, comprising potassium GICs with the variable composition in the range of KC$_{96}$-KC$_{36}$. The difference in stacking sequences between even- and odd numbered stages during subsequent K$^+$-ion insertion is described by the Daumas–Hérold defect notation. The domains of 4L and 3L stages coexist and are separated by a Daumas–Hérold wall (Daumas– Hérold type defect) as a domain boundary[90]. So, the phase transition proceeds like a single-phase reaction via migration of the Daumas–Hérold walls which separate multiple domains (Figure 2.8). The increase of accommodated potassium atoms results in the appearance of the stage 2L (including stage 2) that coexists with stage 3L in the compositional range of KC$_{36}$–KC$_{24}$. The most of the Daumas–Hérold defects vanish with the formation of a single phase of 3D-ordered stage-1 KC$_8$ at the end of the intercalation process. Notably, the reverse deintercalation process is accompanied by transformation from stage-1 KC$_8$ into stage-2 KC$_{16}$ preserving the ordering within plane.

The utilized electrolyte solvents affect the potassium GIC evolution during (de)intercalation processes. *Ex situ* XRD data of the K$^+$-ion (de)intercalation into graphite electrodes in K cells with dilute ether-based electrolyte solutions unveiled the intercalation of solvated K$^+$ ions. The transformation sequence occurs in the order graphite → stage 3 (KC$_{24}$) → stage 2 (KC$_{24}$/KC$_{16}$)→ stage 1 (KC$_8$) during the reduction process (corresponding to the intercalation) and vice versa during an oxidation process (the deintercalation)[92]. Moreover, the observed enhanced interlayer

distances (12.11 Å) lead to the capacity decay during charging\discharging owing to the large volume change and, thus, the electrical isolation of the active particles.
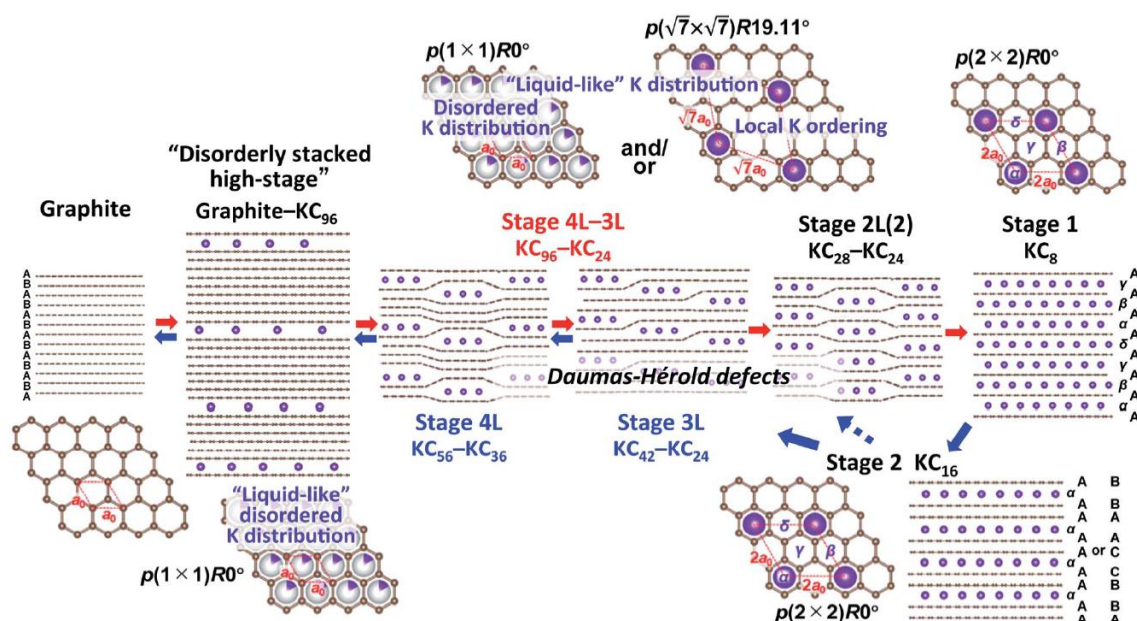


Figure 2.8. Scheme of the plausible phase evolution of graphite during $K^+$-ion (de)intercalation[90] (red and dark blue arrows denote intercalation and deintercalation respectively).

Predominantly, the electrochemical performance of the graphite electrode depends on the electrode and electrolyte compositions, on particle morphology, and on the intrinsic structural properties. For instance, reduced initial Coulombic efficiency values in the range of 40-60% arise from electrolyte decomposition until the formation of a stable SEI on electrode. The formation of resistive films on the graphite surface results in capacity degradation during cycles. In addition, graphite electrode suffers from exfoliation of layers accompanied by significant electrolyte decomposition in K cell with the PC-based electrolyte[93]. However, the proper electrolyte choice might overcome these obstacles. For example, the usage of EC-based electrolyte solutions instead of PC-based ones does not lead to the peeling off of graphene layers[90]. Furthermore, the enhanced CE values (>80%) of graphite electrodes in K cells with elaborated electrolyte solutions at first cycles are reported[12,44,57,89,94].

To date, high CE values and excellent cycle stabilities have been observed in following electrolyte solutions: [1 M KFSI/EC:DEC (1:1 v/v)][89], [7 mol·kg$^{-1}$ KFSI/DME][57], and [KFSI:ethylmethylcarbonate (EMC) (1:2.5, molar ratio)][95]. Conventional carbonate-based electrolyte solution [KPF$_6$/EC:DEC (1:1, v/v)] could be used to electrochemically examine carbonaceous electrodes in K-metal cells[12]. However, the high impedance value in a K cell with [0.8 KPF$_6$/EC:DEC (1:1 v/v)] electrolyte solution is reported[96]. The utilization of KFSI electrolyte salt in the mixture of EC:DEC(1:1, v/v) compared to KPF$_6$ and KTFSI is more beneficial to achieve better cycle stability[90]. The graphite electrode in ether-based electrolyte ([1 M KPF$_6$/DME][97])

instead of carbonated-based one exhibited the lower impedance values. The formation of GICs during cycling in ether-based electrolytes differs from those observed for potassium GICs in carbonate-based electrolytes. Notably, only highly concentrated ether-based electrolytes such as 7 mol kg$^{-1}$ KFSA/DME[57] facilitate the reversible (de)intercalation of desolvated K$^+$ ions into graphite structure. On the other hand, both K$^+$ ions and electrolyte solvent molecules are inserted into graphite framework in dilute ether-based electrolytes such as 1 M potassium trifluoromethanesulfonate (KOTf)/diethylene glycol dimethyl ether (diglyme)[92] and 1 M KPF$_6$/DME.

Constituents of electrode composite such as a binder and a conductive additive also influence the electrochemical properties of graphite in K cells. The utilization of sodium polyacrylate (PANa) and sodium carboxymethylcellulose (Na-CMC) results in the enhanced CE values (79 and 89% respectively) in K‖graphite cells compared to the CE value of 59% for a conventional poly(vinylidene fluoride) (PVdF) binder[89]. The deteriorated performance of graphite electrode with PVDF binder might originate from incomplete and unstable surface passivation or from insufficient mechanical strength against large volume changes during cycling. Beltrop et al. demonstrated the CE value of 81.8% at the first cycle in K cell with graphite electrode comprising Na-CMC binder and excellent stability during subsequent cycles[94].

Furthermore, the reported large reversible capacity values[96] exceeding the theoretical capacity value of 279 mAh g$^{-1}$ originate from the contribution of the carbon conductive additive. Xing et al.[98] demonstrated that the carbon black electrode (Super C45, Imerys Graphite and Carbon), comprising 10 wt % of Na-CMC as a binder, delivered reversible capacity values of 268 mAh g$^{-1}$ at the first cycle at the current rate 27.9 mA g$^{-1}$. The capacity value is reduced to 235 mAh g$^{-1}$ at the 100th cycle upon subsequent cycling at the current density 279 mA g$^{-1}$. The carbon black electrode delivers low initial CE values (47.6% for Super C45, Imerys Graphite and Carbon[98]; 20% for carbon-black-like material exhibiting an onion-like structure[99]) owing to its large surface area and, hence, amplified electrolyte decomposition. Nevertheless, carbon black addition improves the cycle stability of a graphite electrode since it serves an electric conductive agent between the active material particles during K$^+$-ion (de)intercalation that is accompanied with the huge volume changes. Thus, optimization of the electrode composition is required to achieve a good cycle stability and high CE values of a graphite electrode in K cells.

The graphite particle morphology tunes its electrochemical performance in K cells[90]. The smaller particles (3 μm) with higher surface area values promote the electrolyte decomposition resulting in reduced CE value of 60% compared to larger particles (the CE value of 76% for particles with both sizes 15 μm and 30 μm)[90]. Whereas, the initial capacity value of 240 mAh g$^{-1}$ remains independent from particle morphology. Remarkably, the increase in the capacity retention values

from 85% to 96% upon 30 cycles is achieved by the utilization of the smallest graphite particles (3 µm).

The structural properties of graphite also influence its electrochemical performance in K cells[17]. Graphite with a small interlayer distance ($d_{002}$) of 3.355 Å delivers the best cycle performance. The capacity retention is decreased in the interlayer distance order 3.355, 3.360, and 3.366 Å. Hence, the graphite structure with an average small d002 is more favorable for reversible $K^+$-ion (de)intercalation at room temperature. Table 2.3 summarizes the electrochemical properties of graphite electrode in K cells with various electrolytes.

Table 2.3. Summary of the electrochemical properties of graphite negative electrodes

| Electrolyte | Binder | Specific capacity, mAh·g$^{-1}$ | Coulombic efficiency, % | Reference |
|---|---|---|---|---|
| 0.7 M KPF$_6$/EC:DEC (1:1, v/v) | Na-CMC | 280 (C/10) | 92 | [44] |
| 1 M KFSI/EC:DEC (1:1 v/v) | PVDF | 240 (C/10) | 60 | [90] |
| 1 M KFSI/EC:DEC (1:1 v/v) | PAN | 240 (C/10) | 88 | [90] |
| 0.8 M KPF$_6$/EC:DEC (1:1 v/v) | PVDF | 240 (C/10) | 42 | [90] |
| 1 M KTFSI/EC:DEC (1:1 v/v) | PVDF | 240 (C/10) | 49 | [90] |
| 1 M KOTf/diglyme | PVDF | 105 (C/10) | 79 | [92] |
| 1 M KFSI/EC:DEC (1:1 v/v) | PVDF | 240 (C/10) | 59 | [89] |
| 1 M KFSI/EC:DEC (1:1 v/v) | Na-CMC | 240 (C/10) | 89 | [89] |
| 1 M KFSI/EC:DEC (1:1 v/v) | PAN | 244 (C/10) | 79 | [89] |
| 1 M KFSI/EC:DEC (1:1 v/v) | PAN | 220 (15C) | | [89] |
| 0.8 M KPF$_6$/EC:DEC | PAN | 250 (C/10) | 65 | [57] |
| 7 mol·kg$^{-1}$ KFSI/ DME | PAN | 260 (C/10) | 81 | [57] |
| KFSI:EMC (1:2.5, molar ratio) | Na-CMC | 250 (C/3) | 60 | [95] |
| N-butyl-N-methyl bistrifluoromethane-sulfonyl imide (Pyr$_{14}$TFSI) + 0.3 M KTFSI + 2wt.% ethylene sulfite (ES) | Na-CMC | 270 (C/27) | 82 | [94] |

| | | | | |
|---|---|---|---|---|
| 1 M KPF$_6$/EC:DEC (1:1, v/v) | PVDF | 240 (C/12) | 47 | 100 |
| 1 M KPF$_6$/EC:PC (1:1, v/v) | PVDF | 240 (C/12) | 67 | 100 |
| 1 M KPF$_6$/EC:DMC (1:1, v/v | PVDF | 220 (C/10) | 43 | 100 |
| 1 M KPF$_6$/DME | Na-CMC | 108 (1C) | 87 | 97 |
| 1 M KPF$_6$/EC:DMC(1:1 v/v) | Na-CMC | 135 (1C) | 70 | 97 |

**Hard carbon**

Hard carbon (HC) consists of randomly oriented small domains of graphene layers with a large interlayer distance and nanopores between the domains. HC does not convert into graphite even upon annealing at temperatures ≥3000°C and, hence, HC is also called non-graphitizable carbon[101].

The Raman spectrum of HC powder (Figure 2.9a) shows two characteristic broad bands located at ~1350 cm$^{-1}$ (D-band) and at ~1580 cm$^{-1}$(G-band). Defect-free graphite exhibits two Raman-active $E_{2g}$ vibrational bands arising from the carbon atoms with $D_{6h}$ symmetry. Generally, one of them, the $E_{2g2}$ band, is typically denoted as the G-band[102]. Defects induce the appearance of the additional D-band. The emergence of the D-band was initially thought to originate from disorder and symmetry reduction, that cause inactive modes becoming Raman-active[103]. Hence, the D-band intensity has been utilized to estimate the disorder degree in the hard carbon structure. However, the D-band origin is attributed to a so-called double resonance[104], but defects are still required for the double-resonance Raman (DRR) process. The D-band arises from a coupled resonance between excited electrons, phonons, and defects. The incoming laser light excites an electron that transfers to an empty state in the conduction band, forming a hole in the valence band. The further interaction between the excited electron and the lattice result in the phonon annihilation by inelastic electron scattering. Thereafter, defects elastically scatter the electron, transferring it to a virtual state in the vicinity of the initial momentum, but with a slightly increased/decreased energy. The subsequent recombination of electron with the hole in the valence band leads to emission of the photon with a reduced/ increased frequency. Figure 2.9b,c illustrates a scheme of the DRR process.
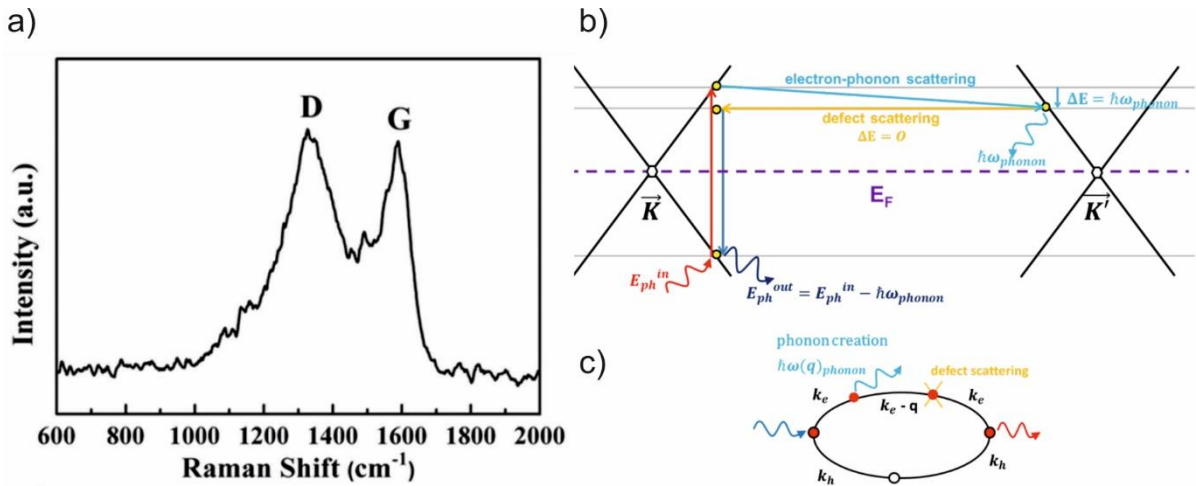
Figure 2.9. a) Typical Raman spectrum of hard carbon structure[105]; b) schematic illustration of a DRR process and c) respective Goldstone diagram. Notably, the depicted process is not the only possible DRR route[102].

**Relation between synthesis conditions and HC properties**

The hydrothermal carbonization (HTC) technique is beneficial for HC material production for the sake of sustainable energy storage since it has advantages such as lower energy consumption and less gas emission over pyrolysis[106,107]. The composition, morphology, size, and other properties of obtained HC can be tuned by adjusting reaction conditions, such as temperature, synthesis duration (or also called residence time), precursor material concentration, and pH[106,107].

HTC implies the biomass transformation into various functional carbon compounds under relatively mild synthesis conditions. Water acts both as the media and catalyst to facilitate the hydrolysis and cracking of biomass. At high temperatures, water hydrolyzes organic compounds, which can be further catalyzed by acids or bases[106,107]. The formation of organic acids (e.g., acetic, formic, and lactic acids) is accompanied with the decline in pH-value and contributes to the hydrolysis with generation of smaller fragments from oligomers and monomers. The amount of colloidal carbon particles magnifies with the enhanced reaction degree. When the temperature and pressure approach an appropriate level, volatile products are emitted and organic precursors are converted to solids. The porosity of hydrothermal carbons is produced at this 'fragmentation' stage as generated gaseous products create pores host structure. Sevilla and Fuertes have inferred the formation mechanism can as follows: (1) the dehydration and cracking, (2) the polymerization and condensation, (3) the aromatization, and (4) the nucleation and subsequent chain propagation[108,109]. The temperature is the most essential parameter in HTC process. The increased temperature results in the chemical bond breakage in the polymers, generation of volatile compounds and rearrangement reactions of residues. Hereafter, the further conversion reactions of some unstable

volatile compounds are designated as the secondary reactions[106]. The higher temperature values promote the enhanced product yield since there is the extra energy to destroy the biomass bonds. On the other hand, the temperature increase often results in the reduced product yield. The origin might be the dissolution of total organic carbon, including sugars and organic acids. Sun et al. obtained the extremely high product yields at temperatures below 200°C[110].

Furthermore, temperature influences the particle morphology. The particles derived from cellulose upon HTC at a low temperature of 160 °C resemble the parent framework. The increase in temperature up to 220 °C cause the formation of spherical-like particles[111]. The further temperature increase promotes the gas product emission leading to more pores in the structure and, hence, in the enlarged surface area.

The HTC duration or residence time affects the properties of obtained compounds. The product yield declines with the increased HTC duration. Since longer HTC duration results in the polymerization of dissolved fragments in water, forming the secondary products with a polyaromatic structure[106]. Furthermore, the residence time also determines the particle size due to the excessive polymerization (Figure 2.10). The increased HTC duration leads to the broader particle size distribution[112]. The duration time affects the reaction end point, specific surface area, and pore volume, owing to the structural melting, elemental realignment, and shrinkage[113].

The size of microspheres increased at higher precursor concentration when easily dissolved carbon-sources were utilized (glucose and sucrose). However, the relation between particle size and precursor concentrations depends on the raw material. The enhanced precursor concentrations of cellulose lead to the smaller microspheres[106]. pH-value also may control the particle size: the addition of different amounts of oxalic acid ($C_2H_2O_4$) varies the size of HC derived from glucose in the range of 0.5–0.8 $\mu$m[114].
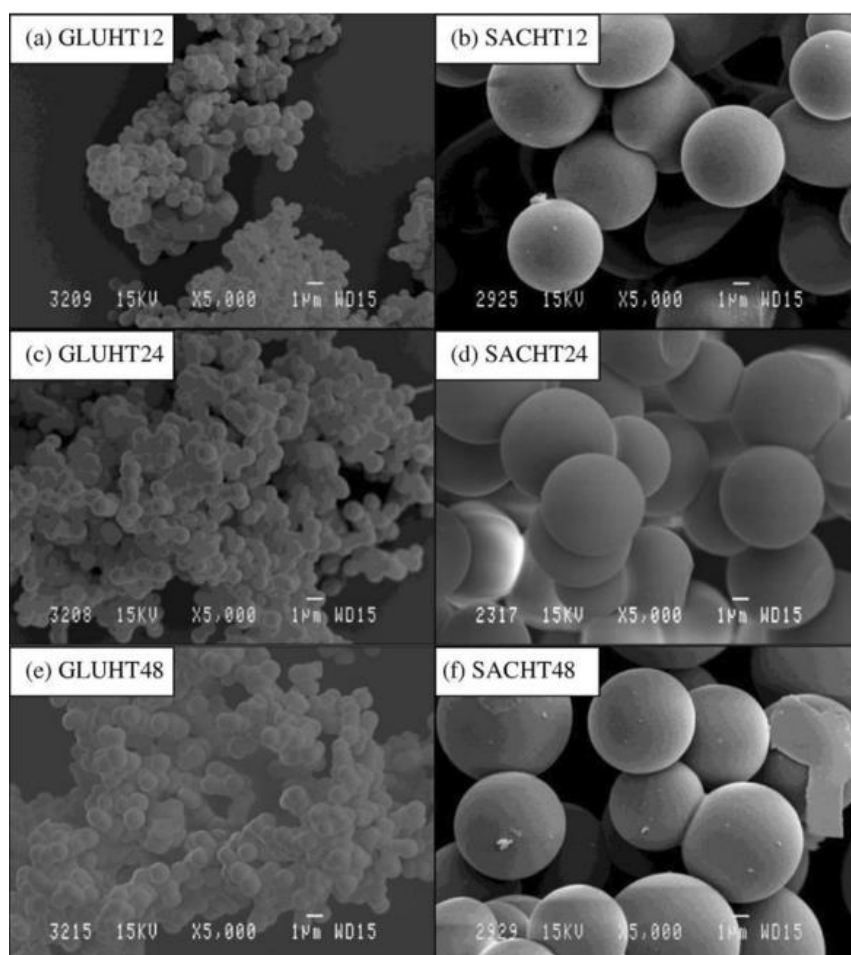
Figure 2.10. Scanning electron microscopy (SEM) images of hydrothermal carbons derived from glucose (a, c, e) and saccharose (b, d, f) upon different HTC duration: (a, b) during 12 h; (c, d) during 24 h; (e, f) during 48 h[112].

Generally, the synthesis of HC proceeds via two-step heat-treatment comprising pre-heating step (**I**) and carbonization step (**II**). To approach stable and profitable cycling of HC electrodes in K cells, all synthesis parameters (pre-heating temperature $T^I$, pH, type and concentration of precursors, duration time, carbonization temperature $T^{II}$) should be probed.

HC derived from various carbon-sources: rice-starch[28], oak[115], waste-tire rubber[116], cellulose[117], skimmed cotton[118], potatoes[119], loofah[120], and maple leaves[121] possessed diverse morphology (chunks; mesoporous bulk structure; crumbly chunks; chunks; tubular; mesoporous chunks, hollow tubular framework, respectively) and was examined in $K^+$-ion system. Figure 2.11 illustrates the morphology of obtained HC powders. None of them resembles the spherical particles synthesized from simple sugars such as glucose and saccharose. Table 2.4 summarizes the electrochemical properties in K cells for HC obtained from various carbon-sources. The cellulose- and skimmed cotton-derived HC electrodes deliver the better electrochemical performance in terms of specific capacity values and cycle stability. The former demonstrates the initial discharge capacity value of 290 mAh·g$^{-1}$ with CE value of 83% in a K cell with [1 M KFSI / EC:DEC (1:1,

v:v)][117]. The latter exhibits the specific discharge capacity value of 235 mAh·g$^{-1}$ with CE value of 73 % in a K cell with [1 M KPF$_6$/DME] at the first cycle.
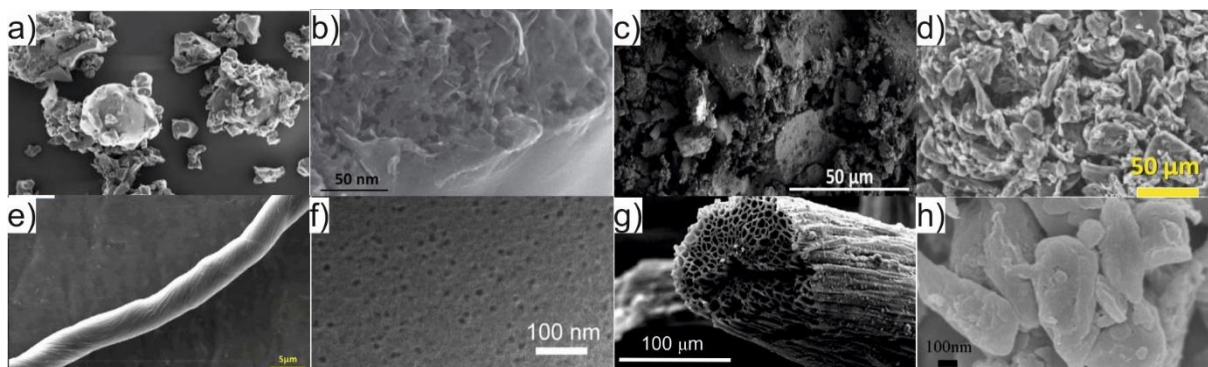


Figure 2.11. SEM images of HC derived from: (a) rice-starch[28]; (b) oak[115]; (c) waste-tire rubber[116]; (d) cellulose[117]; (e) skimmed cotton[118]; (f) potatoes[119]; (g) loofah[120]; and (h) maple leaves[121].

Table 2.4. Summary of electrochemical properties of HC obtained via different synthesis conditions.

| Carbon source | Synthesis conditions | binder | Electrolyte | Initial specific capacity, mAh·g$^{-1}$ | CE, % | Reference |
|---|---|---|---|---|---|---|
| rice-starch | T$^I$=230°C (air; 4h), T$^{II}$=1100°C (Ar; 1h) | PVDF | 1.5 M KFSI / EC:DMC (1:1, v:v) | 200 (C/10) | 50 | 28 |
| oak | T$^I$=600°C (N$_2$, 12 h), T$^{II}$=1100°C (Ar; 6h) | PVDF | 0.4 M KPF$_6$ / EC:DEC (1:1, v:v) | 233 (C/13) | 56 | 115 |
| waste-tire rubber | T$^I$=120°C (H$_2$SO$_4$; 12 h), T$^{II}$=1600°C (N$_2$) | PVDF | 0.8 M KPF$_6$ / EC:DEC (1:1, v:v) | 181 (C/10) | 37 | 116 |
| cellulose | T$^I$=275°C (air; 12 h), T$^{II}$=1500°C (Ar; 1h) | PAN | 1 M KFSI / EC:DEC (1:1, v:v) | 290 (C/12) | 83 | 117 |

| | | | | | | |
|---|---|---|---|---|---|---|
| sucrose | $T^I$=275°C (air; 12 h), $T^{II}$=1500°C (Ar; 1h) | PAN | 1 M KFSI / EC:DEC (1:1, v:v) | 240 (C/10) | - | [117] |
| skimmed cotton | $T^I$=900°C (2 h), $T^{II}$=1200°C (Ar; 2h) | Na-CMC | 1 M KPF$_6$/DME | 235 (C/6) | 73 | [118] |
| potatoes | $T^I$=500°C (Ar), $T^{II}$=1000°C (Ar; 2h) | PVDF | 3 M KFSI/DME | 270 (C/3) | 43 | [119] |
| loofah | $T^I$=60°C (alkali,48h), $T^{II}$=1000°C (N$_2$; 2h) | PVDF | 1 M KPF$_6$ / EC:DMC (1:1, v:v) | 155 (C/1.5) | 38 | [120] |
| maple leaves | $T^{II}$=700°C (Ar; 7h) | PVDF | 1 M KClO$_4$ / EC:DEC (1:1, v:v) | 283 (C/6) | 30 | [121] |

The hard carbon microspheres are derived via the HTC of sucrose at $T^I$=195 °C followed by annealing at $T^{II}$=1100 °C under Ar atmosphere (Figure 2.12a)[122]. The HC electrode demonstrated sloping curves at 1.25−0.3 V *vs* K$^+$/K and plateau regions at 0.2 and 0.33 V *vs* K$^+$/K during the intercalation and deintercalation, respectively (Figure 2.12b)[122]. The specific discharge capacity value was observed to be 260 mA·h·g$^{-1}$ at the first cycle in K cell with [0.8 M KPF$_6$/ EC:DEC(1:1, v:v)]. The substitution of PVDF binder by Na-CMC improves the initial Coulombic efficiency value from 49% to 76%[122,123].
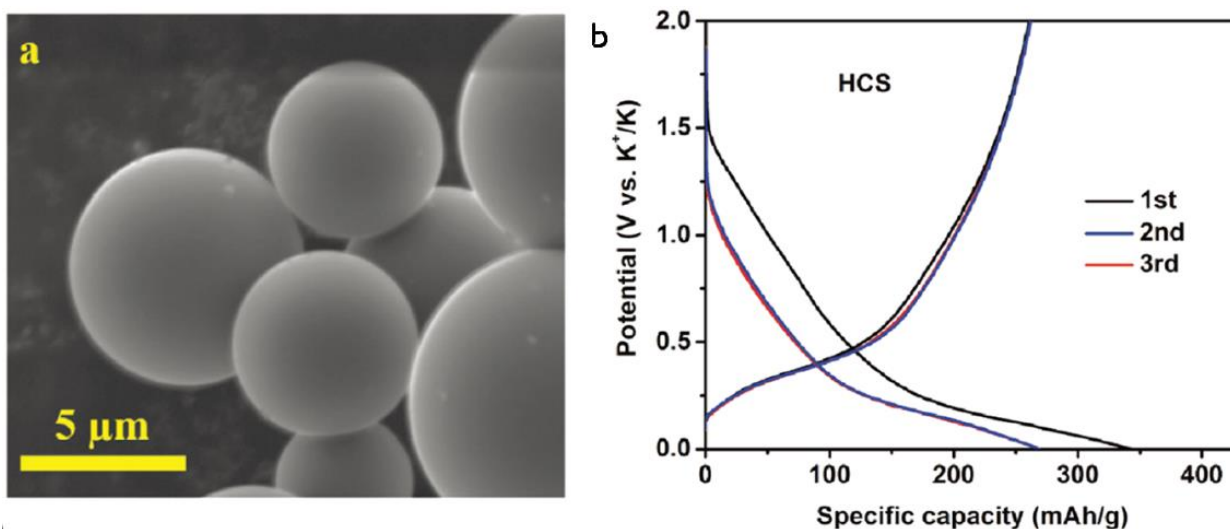
Figure 2.12. (a) SEM image and (b) the first three charge/discharge cycles of sucrose -derived HC in a K cell with [0.8 M KPF$_6$/ EC:DEC(1:1, v:v)][122]

The cross-linkage process is proposed to influence the resulted HC structure. Preheating procedure at T$^I$=275 – 300 ºC in air leads to the dehydration and crosslink between the polymer chains resulting in the larger pores, the increased interlayer distance between the stacked carbon layers, and the higher specific capacity values[117]. The carbonization of the pristine cellulose without preheating produces the dense host with smaller pores exhibiting the reduced specific capacity values[117].

The increased carbonization temperature results in the reduced surface area, the decreased interlayer space, and the enhanced micropore radii[117]. The specific discharge capacity of HC electrode in a K cell increases from 50 to 290 mA·h·g$^{-1}$ with raising carbonization temperature in the range of 700-1500°C (Figure 2.13a)[117]. The highest initial CE of 83% is attained via preheating treatment at T$^I$=275°C with subsequent annealing at T$^{II}$=1500°C for cellulose-derived HC electrode[117]. Besides, good cycle stability and higher CE >99.5% are observed upon 50 cycles (Figure 2.13b)[117]. HC electrodes demonstrate larger reversible specific capacity values compared to the graphite electrode.
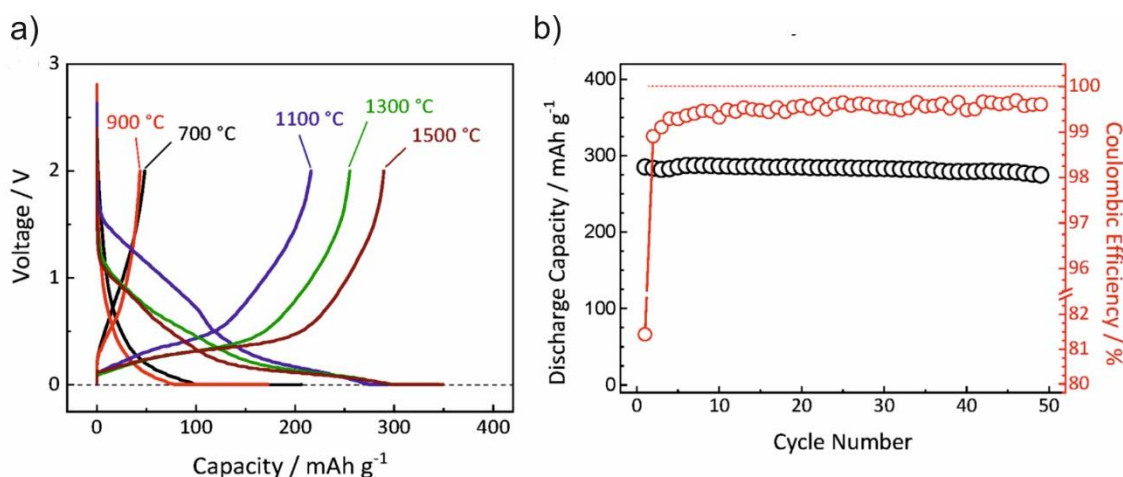
Figure 2.13. (a) Charge−discharge curves of cellulose-derived HC ($T^I$=275°C) after annealing at 700−1500 °C and (d) capacity retention of the HC ($T^I$=275°C; $T^{II}$=1300 °C) with 5 wt % PANa binder in K cells with [1 M KFSI /EC:DEC (1:1, v:v)][117]

The similar study of carbonization temperature $T^{II}$ impact on sucrose-derived HC ($T^I$=180°C) was conducted[124]. The enhanced carbonization temperature $T^{II}$ results in the increased number of stacking $sp^2$-carbon layers, the reduced interlayer distance, the enlarged domain size, and reduced amount of carbon defects. Concomitantly, hydrogen content declines with annealing temperature $T^{II}$ increase, while micropores expand and are closed against nitrogen and oxygen molecules above 1100°C and against helium atoms above 1300°C[124]. The specific surface decreases without a significant variation in the HC microsphere size. Hence, sucrose-derived HC after carbonization temperature $T^{II}$ in the range of 700−1300°C possesses the microstructure with smaller open micropores and smaller graphitic layered domains comprising carbon vacancy and hetero atoms resulting in sloping potential curves and large initial irreversible capacities. The increase in carbonization temperature $T^{II}$ up to 1300−2000 °C leads to HC with larger and thicker stacking of graphitic planes and closed larger micropores[124]. The $K^+$-ion intercalation into the large interlayer space of defective carbon layers prevails for HC samples obtained after annealing at $T^{II}$=700°C-900°C, but $K^+$-ion insertion into the narrow spacing between graphitic planes dominates for the HC annealed at $T^{II}$=1100°C −2000°C[124]. Thus, the precise optimization of synthesis parameters is required to obtain HC material for PIBs. The analysis of published data indicates the attractive temperature range for HC powder annealing resides at 1100-1500°C1. The decreased annealing temperature resulted in poor electrochemical performance in K cell. Further enhanced annealing temperature is undesirable owing to K+-ion battery development at affordable cost for the needs of stationary energy storage. Thus, 1200°C and 1500°C chosen to obtain a clue about best synthesis conditions of HC powder.

**Mechanism of $K^+$-ion storage in HC**

The $K^+$-ion storage mechanism identification in HC host is sophisticated owing to the diverse variety of structures obtained via different synthesis conditions as described above. HC consists of abundant defects, edges, functional groups, randomly stacked graphene layers, and a large amount of nanopores, that provide active storage sites. Various storage scenarios have been proposed, involving adsorption on defects, edges, and functional groups; intercalation between $sp^2$-carbon layers, and filling into nanopores (Figure 2.14)[125–127].

Generally, defect/ heteroatom adsorption mainly corresponds to the slope capacity for $K^+$-ion storage, while pore filling process is responsible for the plateau region at the charge/discharge

profile. The filling of enough large $K^+$ ions into the pores results in a stronger coordination of $K^+$ ions with pore walls, resembling the intercalation of $K^+$ ions in graphite. Furthermore, the $K^+$-ion intercalation between graphene layers significantly contributes to the plateau region. Hence, two main mechanisms have been considered to influence the electrochemical performance of batteries: a surface-induced capacitive process and diffusion-controlled intercalation process[125–127]. The contribution of surface-induced capacity increases with a higher specific surface area, that might be achieved by reducing the size of active materials or introducing a porous structure[125,126]. Therefore, the HC structure is adjustable to maximize the contribution from the selected storage type depending on synthesis conditions.
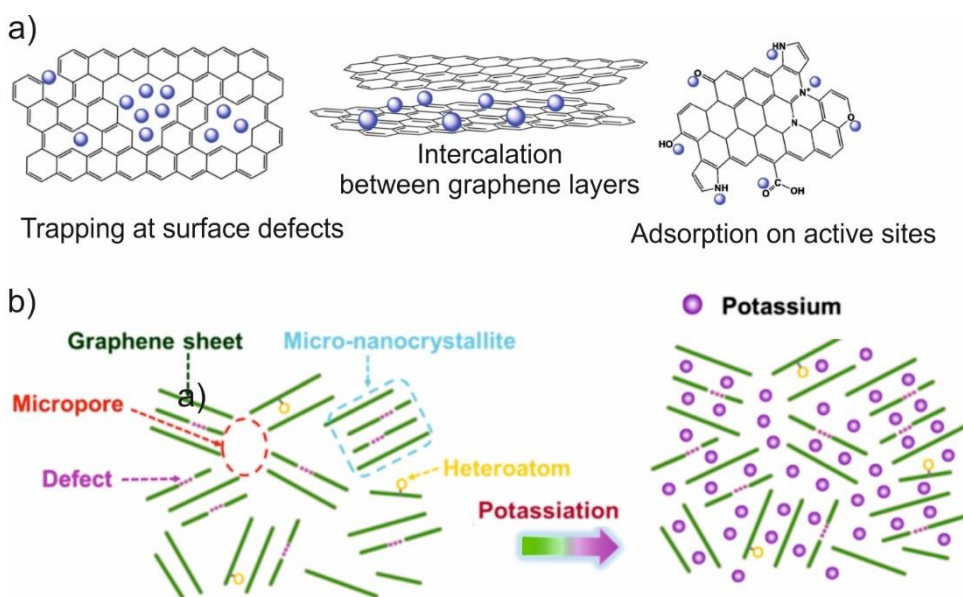


Figure 2.14. Schematic of the mixed mechanisms of $K^+$-ion storage for (a) HC obtained from Al-based MOF[126] and (b) sucrose-derived HC[127].

Herein, in this thesis HC is selected as the negative electrode due to its ability to sustain fast and reversible $K^+$-ion intercalation required for stable performance of PIBs[128,129] compared to graphite which experiences a large volume expansion in $K^+$-systems[13] and, therefore, could not be implemented in PIBs despite its potential simplicity for further examination. However, HC reveals reduced Coulombic efficiency at the first discharge cycle and significant irreversible capacity loss (ICL) in the course of further electrochemical cycling, which both prevent prosperous commercialization of PIBs[117,123,128]. High ICL accompanied by low CE originates from irreversible reactions that could be assigned to poor or unstable SEI. A uniform and elastic SEI might suppress the capacity decay and prevent irreversible side reactions

**SEI formation/composition on HC in different electrolytes**

The electrochemical performance of anodes in PIBs depends on solubility, uniformity, and $K^+$-ion conductivity of SEI layers formed in the different electrolytes. The choice of electrolyte

components determines the products of salt and solvent decomposition, the resulted SEI layer composition and, thereby, its properties. To date, the reported literature covering the characterization of SEI formed in $K^+$-ion systems is limited.

The SEI layer formed on cellulose-derived HC in a K cell with [1M KFSI/PC] was characterized by hard X-ray photoelectron spectroscopy (HAXPS) and time-of-flight secondary ion mass spectrometry (TOF-SIMS)[117]. Figure 2.15a shows the C1s HAXPS spectrum of HC electrode retrieved upon 10 cycles delivering the specific discharge capacity value of 215 mA·h·g$^{-1}$ and the CE value of 84%. The observed peaks are attributed to the −CH$_2$-COO−, R-OK, −C(=O)−, and −OC(=O)O− bonds indicating the presence of alkyl carbonates and alkoxides, due to PC decomposition. The F1s spectrum displays peaks attributed to the KF and −SOxF species, originating from the FSI− anion decomposition (Figure 2.15b). The S1s spectrum exhibits peaks ascribed to −SO$_2$F, −SO$_2$−, >S=O, S$^0$ and K$_x$S$_y$ supporting the formation of the anion-derived SEI film (Figure 2.15c). The presence of peaks corresponding to S$^0$ and K$_x$S$_y$ are reported to be characteristic of anion-derived SEI layers formed in the highly concentrated TFSI- and FSI-based electrolytes in Li$^+$-ion[130] and Na$^+$-ion[131,132] systems. Good electrochemical HC behavior is tentatively attributed to the prevailing contribution of the FSI$^-$-anion decomposition products in the SEI formation that is consistent with other reported excellent performances of negative electrodes in K cells with KFSI-based electrolyte solutions[57,85,86].

The TOF-SIMS measurements mainly reveal the presence of inorganic fragments (e.g., K$_2$O, and KF) owing to higher solubilities of the potassium organic compounds (e.g., potassium alkyl carbonates and potassium alkoxides)[117]. The schematic composition of SEI layer formed in K cell is presented in Figure 2.15d. In the K cell, the SEI film comprises the inner and outer layers. The former contains both organic and inorganic species, while the latter mainly consists of inorganic species. The comparison with SEI layers formed in Li$^+$- and Na$^+$-systems[117] unveils different surface chemistries depending on the alkali metal ion. Hence, the optimal combination of salts, solvents, and additives should be unique for successful surface passivation in $K^+$-ion systems.
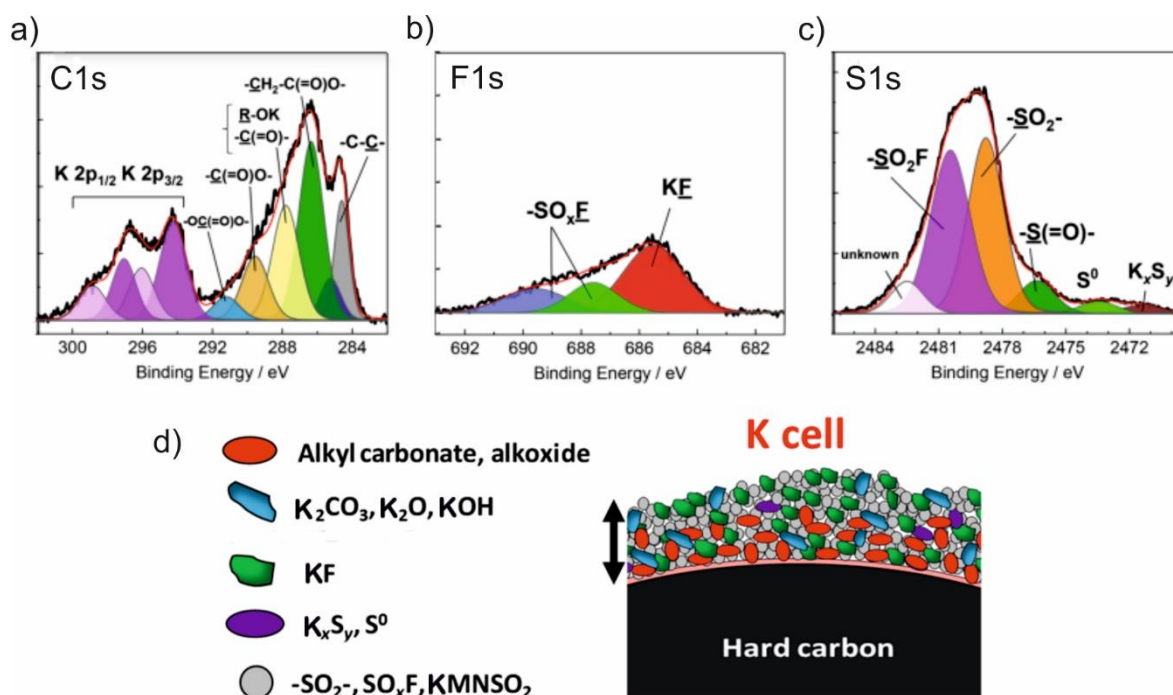
Figure 2.15. a) C1s, b) F1s, c) S1s HAXPS spectra of HC electrode and d) the schematic illustration of the SEI composition formed on the HC electrode cycled in K cells with [1M KFSI/PC] at the potential range 2.0−0.002 V vs $K^+/K$[117]

The rigorous comparison of surface layers formed on lignin-derived HC in four different electrolyte solutions [0.8 M $KPF_6$/ EC:DEC(1:1,v:v)], [1 M KFSI/ EC:DEC(1:1,v:v)], [1 M $KPF_6$/ DME], and [1 M KFSI/ DME] was conducted by Wu, et al.[133]. The surface chemistry characterization was performed by using XPS and high-resolution transmission electron microscopy (HRTEM).

Figure 2.16 illustrates the XPS analysis of HC electrodes cycled in four electrolytes. The C1s XPS spectra of all samples exhibit peaks corresponding to $K_2CO_3$, RCOOK, C–O, C–C, C–H bonds. C–C and C–H bonds correspond to the $sp^2$-carbon content in the SEI layer. The peaks referring to the C–O, C=O bonds, and K salt are observed in the O1s XPS spectra. However, the peak corresponding to RO-COOK only emerges in carbonate-based electrolytes, while peak attributed to R-OK appears only in ether-based electrolytes. The F1s spectra of HC electrode cycled in $KPF_6$-contained electrolytes display peaks corresponding to $K_xPF_y$, $K_xPO_yF_z$, K-F bonds, while the F1s spectra of samples cycled in KFSI-based electrolytes contains only peaks attributed to $-SO_xF$ and K-F bonds[133].

The electrolyte solution structure adjusts the reduction potential of its components. The electrolyte constituents should decompose in the order: FSI-, EC, DEC, DME, $PF_6^-$, thus, contributing to the SEI formation[134]. The higher reduction potential of $FSI^-$ than DME, results in the highest KF content ratio in [1 M KFSI/DME]. Furthermore, FSI- anions might suppress the

DME decomposition by surface passivation and, thereby, prevent the reaction between solvent molecules and bare electrode. The R-OK content arising from DME decomposition decreases after substitution of $KPF_6$ with KFSI in the electrolytes, indicating the "inhibitory effect" of $FSI^-$ anions over DME decomposition (Figure 2.16). The suppression of solvent decomposition is also observed in carbonate-based electrolytes utilizing KFSI salt leading to the FSI⁻derived SEI formation. In contrast, the formation of unstable organic SEI film likely originates from the primary solvent reduction[135].
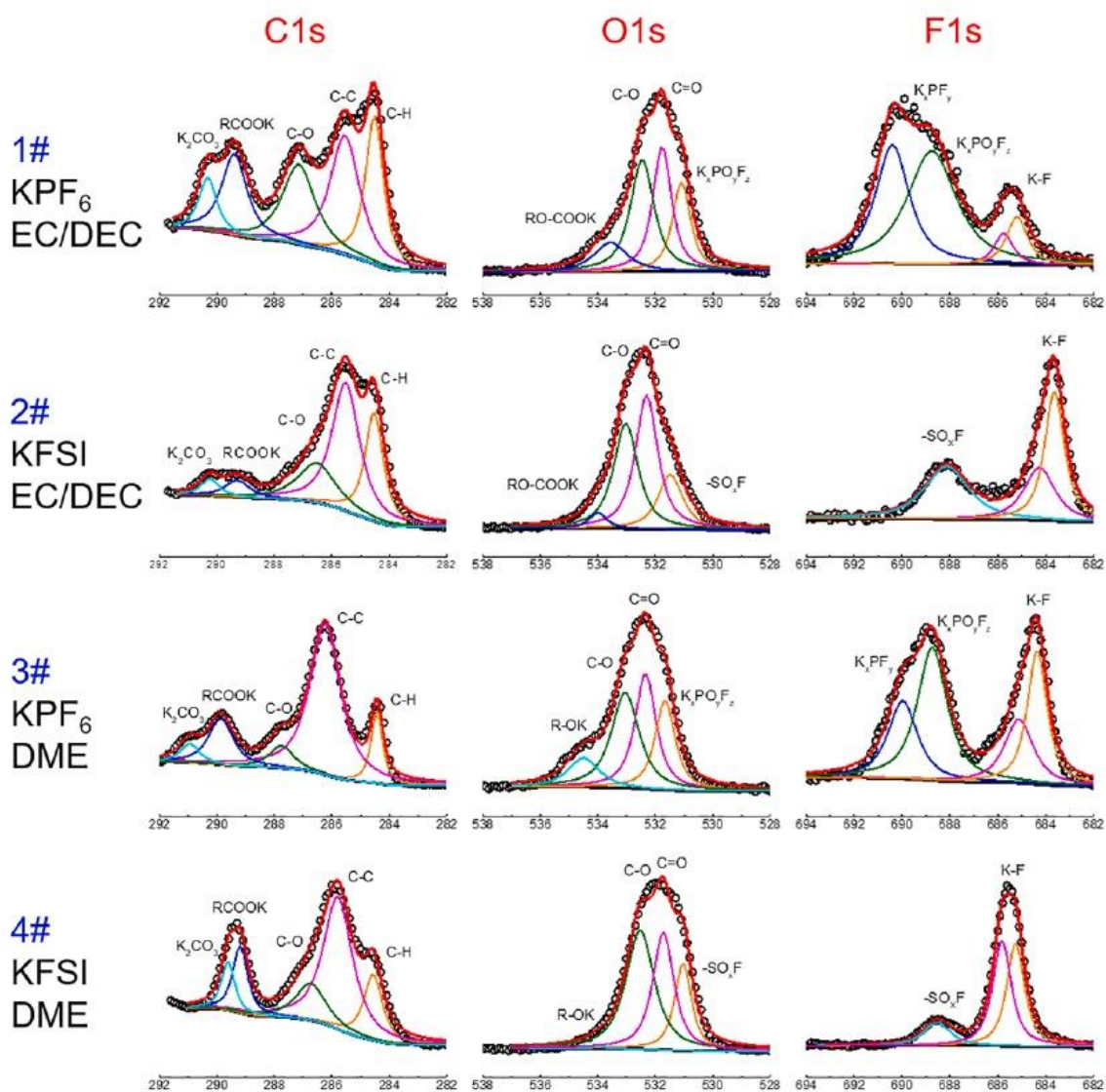


Figure 2.16. C1s, O1s and F1s XPS spectra of HC electrode cycled in four electrolyte solutions[133]

HRTEM combined with selected area electron diffraction (SAED) techniques reveals the distinction in HC electrodes cycled in four electrolytes in terms of the passivated film thickness, interlayer spacing, and graphitization degree (Figure 2.17)[133]. The thickest SEI layer is evidenced on HC surface in [0.8M $KPF_6$/ EC:DEC (1:1, v:v)] (Figure 2.17a). The SEI thickness decreases for HC electrodes retrieved upon cycling in [1 M KFSI/ EC:DEC (1:1, v:v)] and [1 M KFSI/ DME] (Figure 2.17b,d). Remarkably, roughly no SEI formation is detected in electrolyte comprising both

KPF$_6$ salt and DME solvent (Figure 2.17c). In [0.8M KPF$_6$/ EC:DEC (1:1, v:v)] the SEI composition mainly consists of organic compounds such as (CH$_2$OCOOK)$_2$ arising from EC decomposition. The substitution of KPF$_6$ with KFSI in carbonate-based electrolyte results in the predominant content of KF owing to FSI$^-$ decomposition, followed by (CH$_2$OCOOK)$_2$ and C$_2$H$_5$COOK from EC and DEC decomposition, respectively. While in [1 M KFSI/ DME] only electrolyte salt contributes to the SEI film with a higher KF content (Figure 2.17d).
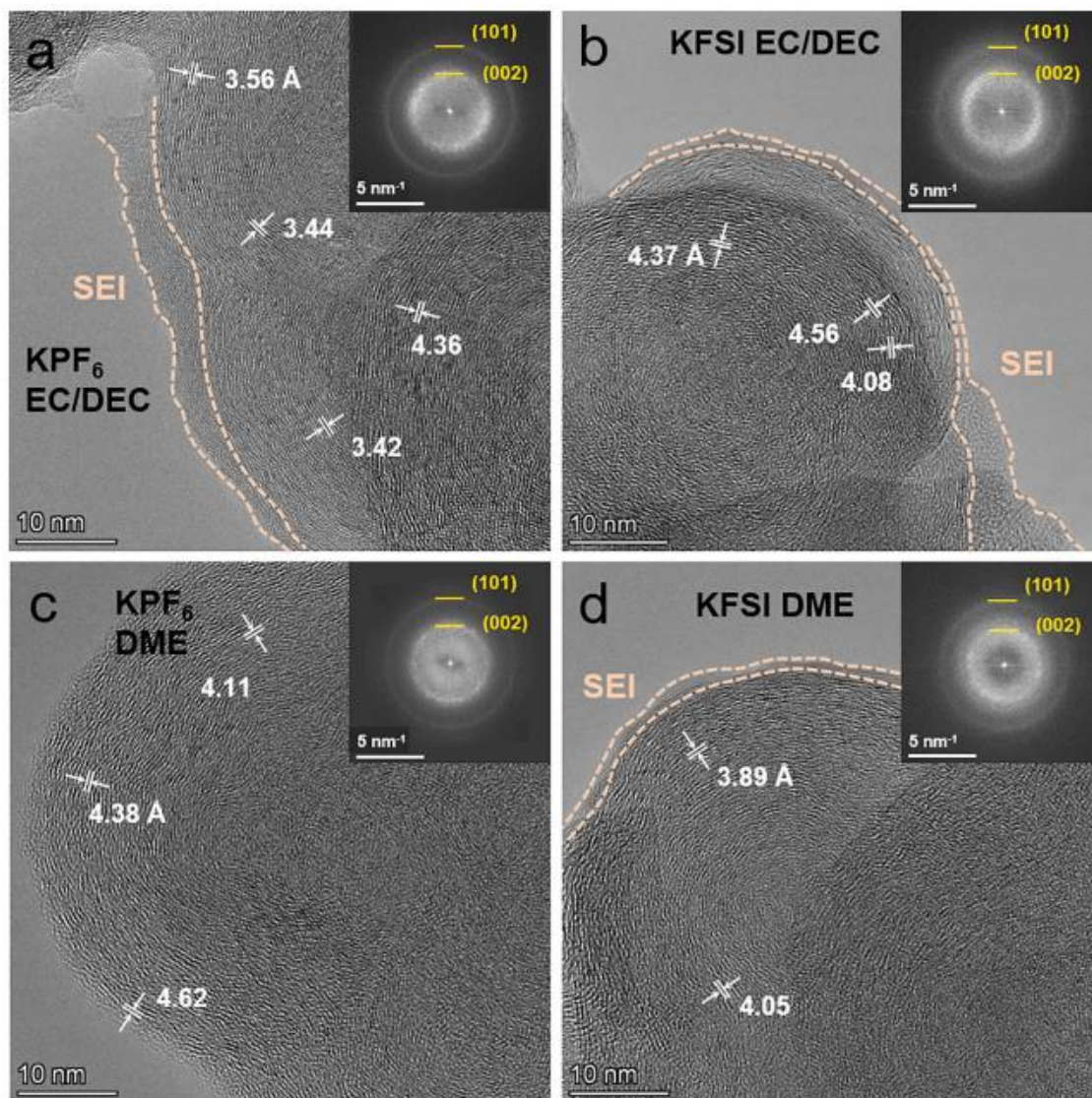


Figure 2.17. HRTEM images of HC electrodes after 5 cycles in a) [0.8 M KPF$_6$/ EC:DEC (1:1, v:v); b) [1 M KFSI/ EC:DEC (1:1, v:v)]; c) [1 M KPF$_6$/ DME]; and d) [1 M KFSI/DME][133].

The measured interlayer distance in typical selected areas of cycled lignin-derived HC indicates the smallest spacing in the range of 3.42–4.36 Å for the electrode cycled in [0.8M KPF$_6$/ EC:DEC (1:1, v:v)]. Whereas, the largest graphite-like nanocrystals are preserved (Figure 2.17a). The bright and sharp diffraction rings in its SAED pattern indicate the higher graphitization degree[136]. Hence, HC cycled in carbonate-based electrolyte with KPF$_6$ salt maintains the most layered structure, implying the intercalation of desolvated K$^+$-ions through organic SEI instead of

chelated $K^+(EC)_2$. In contrast, HC anode upon cycling in [1M KPF$_6$/ DME] shows the largest interlayer distance, probably owing to co-intercalation of the solvated $K^+(DME)_4$.

The XRD data indicate that the lignin-derived HC undergoes smaller volume change in KFSI-contained electrolytes than in KPF$_6$-based counterparts[133]. Compared to the HC before cycling (4.04 Å), the calculated average d-spacings enhances in the order 3.84, 3.84, 3.87, 4.02 Å for anodes cycled in [0.8 M KPF$_6$/ EC:DEC (1:1, v:v)], [1 M KPF$_6$/ DME], [1 M KFSI/ EC:DEC (1:1, v:v)], and [1 M KFSI/ DME], respectively.

The highest initial CE value of 76% is observed in K cell with [1 M KPF$_6$ /DME] whilst K cell with other electrolytes exhibit the initial CE value in the range of 45-52%. However, the worst cycling stability is evidenced for HC in [1 M KPF$_6$ /DME]. HC shows rapid capacity decay, and the cell dies after 40 cycles. On the contrary, K cell with [1M KFSI/ EC:DEC (1:1,v:v)] delivers the best performance over 550 charge/discharge cycles. It might be attributed to the KF-based SEI formation and sufficient solvation of $K^+$-ions by EC molecules. The SEI film with high KF content might effectively separate the HC surface from the organic solvents, suppressing further solvent decomposition. Moreover, since FSI$^-$-anions reduction occurs before EC, K ions have enough number of EC molecules to complete the solvation, thereby, preventing the SEI from being corroded by bare $K^+$-ions. In addition, EC molecules have steric hindrances to co-intercalate into HC host compared to linear smaller DME molecules. Figure 2.18 depicts the summarized scheme of SEI formation and degradation mechanisms in four different K electrolytes proposed by Wu, et al.[133].

The properties of formed SEI layers have crucial impact on battery performance. They may both promote or suppress the continuous decomposition of electrolyte components, electrode deactivation (*e.g.*, exfoliation, pulverization) and, thus, drastic cell degradation. Hence, the choice of appropriate salt and solvents play a vital role in PIB development. Notably, the implementation of electrolyte solutions utilized in Li$^+$- and Na$^+$-systems is not suitable due to different surface chemistries as it was mentioned above. To date, the reported studies concerning the evolution of surface layers in PIBs are limited. Besides, other approaches such as electrolyte additives and salt concentration increase are anticipated to examine to improve the SEI film characteristics. To sum up, further research aiming the SEI formation on the HC surface in K$^+$-ion systems is required since most features of processes occurring at the electrode/electrolyte interface remain vague.
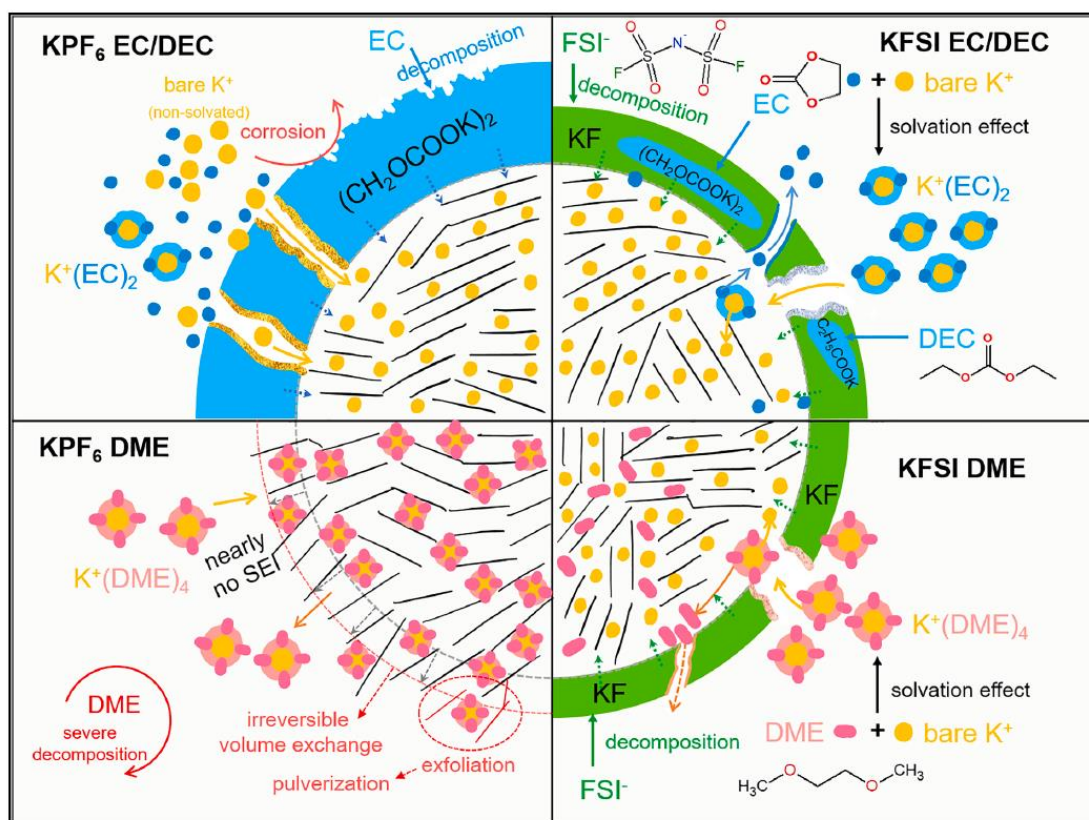
Figure 2.18. The schematic illustration of the SEI layer formation and degradation mechanisms on lignin-derived HC electrodes cycled in K cells with the four electrolytes[133]

**Motivation and objective**

PIBs have attracted significant research interest during last decade due to its low cost combined with competitive energy density characteristics compared to Li-ion batteries. Hence, one of feasible PIB application relates to the stationary energy storage market that will experience exponential growth in coming years. However, full K cells exhibit poor electrochemical performance stemming from electrolyte decomposition during cycling due to the formation of unstable Solid Electrolyte Interphase (SEI) and Cathode Electrolyte Interphase (CEI) layers on surfaces of negative and positive electrodes respectively. Furthermore, carbonaceous anodes delivering high specific capacity values experience own obstacles. For instance, graphite undergoes large volume change during $K^+$-ion (de)intercalation process resulting in an unalterable degradation of K cells. On the other hand, HC electrodes deprived of such challenge demonstrates the enormous irreversible capacity loss with low CE values at the first cycles. The deteriorated performance of HC electrodes in K cells during first cycles arises from continuous reduction of electrolyte components since the deficient surface passivation or surface film cracking leads to the presence of bare spots on electrode that are available for further interaction with electrolyte.

One approach to improve the stability of SEI/CEI layers over cycling is to tune electrolyte composition. But the examination of a wide variety of electrolyte solutions has limitations. Despite

the published advantages of KFSI-contained electrolyte utilization with carbonaceous negative electrodes, they still suffer from aluminum current collector corrosion. This is impermissible for the prosperous elaboration of K full cell with further PIB commercialization. Hence, $KPF_6$ electrolyte salt providing the aluminum passivation is used in present research. Other strategies to develop new generation electrolyte for PIBs comprise solvent change, the enhanced salt concentration, and the utilization of electrolyte additives. Herein, all these approaches are explored. Diglyme-based electrolyte might expand the solubility of $KPF_6$ salt. So, the research objective aims to examine the impact of $KPF_6$ salt concentration on both positive and negative electrode performance in K cells utilizing diglyme-based electrolyte solutions. Fluoroethylene carbonate (FEC) and vinylene carbonate (VC) additives (popular electrolyte additives in $Li^+$-ion batteries) are also tested. The main objective of the study is to probe the formation of surface films on HC electrode using scanning electron microscopic, X-ray photoelectron spectroscopic, in situ atomic force microscopic, and various transmission electron microscopic techniques. The obtained results might assist in the design of full K cell. Moreover, the synthesis conditions tune the resulted hard carbon properties as negative electrode for PIBs. Hence the optimization of HC preparation technique to attain lower irreversible capacity loss during cycling is also required.

Therefore, the present research aims to elaborate the electrolyte solution for PIB with superb electrochemical performance via tuning its composition and probing the surface layers formed on electrode surfaces.

**Chapter 3. Methodology and techniques**

**Synthesis methods, electrode and electrolyte preparation procedures**

**KMFCN**

$K_{1.44}Mn(Fe[CN]_6)_{0.9}\times0.4H_2O$ (KMFCN) was prepared by a precipitation method[1]. 4 mmol of $K_4Fe(CN)_6$ (Ruskhim, >98%) was dissolved in 160 mL of saturated KCl (Sigma Aldrich, >99.5%) solution at room temperature. 4 mmol of $MnCl_2\times4H_2O$ (Sigma Aldrich, >99%) was dissolved in 80 mL of water. Then, the solutions were slowly mixed together dropwise under magnetic stirring. The obtained white precipitate was aged for 4 hours, centrifuged, washed with deionized water and dried overnight at 100 °C under vacuum.

**KVOPO₄**

$KVOPO_4$ (KVPO) was prepared by thermal decomposition of hydrothermally synthesized $K_3(VO)(HV_2O_3)(PO_4)_2(HPO_4)$ ( = "$KVOPO_4\times1/3H_2O$") precursor[2]. First, $V_2O_5$ (Sigma-Aldrich, >99.6 %), $KH_2PO_4$ (Sigma-Aldrich, >99 %), $K_2HPO_4$ (Sigma-Aldrich, >99 %) and oxalic acid (Sigma-Aldrich, anhydrous >99 %) were dissolved in 30 ml of deionized $H_2O$ under vigorous stirring at 25°C according to the following molar ratio:

$$V_2O_5 + 3KH_2PO_4 + 3K_2HPO_4 + 1.5H_2C_2O_4 + 300H_2O$$

Then the mixture was transferred to a 50 ml Teflon-lined stainless-steel autoclave, sealed and kept at 160°C for 16h under intense stirring. The resulting $KVOPO_4\times1/3H_2O$ precursor was washed with water and acetone and heated up to 650°C (3°/min) in Ar flow (10 ml/min) followed by quenching to room temperature to yield $KVOPO_4$. To obtain a carbon-coated $KVOPO_4$/C composite for further electrochemical measurements, $KVOPO_4$ was ground with 12.5 wt.% D-glucose and heated to 650°C (3°/min rate) in flowing Ar (10 ml/min). The residual carbon content was determined by thermogravimetric analysis to be approximately 5 wt. %.

**Hard carbon**

Hard carbon (HC) microspheres were prepared via a hydrothermal method from D-glucose (Sigma Aldrich, >99.5%) followed by pyrolysis. The mixture of 9 g of D-glucose and 0.1 g of pectin (Souzopttorg, ARA104) was dissolved in 25 ml of deionized water and placed in a hydrothermal autoclave reactor with addition of 2 ml polytetrafluoroethylene solution (PTFE: Sigma Aldrich, 60 wt. % dispersion in $H_2O$) or 0.5 g of citric acid $C_6H_8O_7\times H_2O$ (Ruskhim, 99%). The hydrothermal carbonization (HTC) was carried out at temperature $T^I$=180°C or 200°C. The residence time was applied from the set of (8h; 16h; 24h). After the hydrothermal synthesis, a dark

---

[1] Batch of $K_{1.44}Mn(Fe[CN]_6)_{0.9}\times0.4H_2O$ powder was synthesized by Dmitry Rupasov and Polina Morozova

[2] $KVOPO_4$ was synthesized by Nikita Luchinin and Stanislav Fedotov

precipitate was obtained. The powder was centrifuged and washed with deionized water several times, dried in air and annealed in a tubular furnace at $T^{II}$=1200 °C or 1500°C for 5 h in flowing Ar.

**Electrode preparation**

The KVOPO$_4$/C (KVPO) powder was mixed with Super P carbon (Timcal) and polyvinylidene fluoride (PVDF: Sigma Aldrich) in the 60:30:10 mass ratio and afterwards with 1-methyl-2-pyrrolidinone (NMP: Acros organics, extra pure, 99%) in a SPEX 8000M high-energy ball mill for 5 min. The resulting electrode slurry was spread on carbon-coated aluminum foil (MTI, 18 μm) and subsequently dried at 60°C. Finally, the electrodes were dried at 120°C under vacuum overnight. The same electrode preparation technique was applied to the K$_{1.44}$Mn(Fe[CN]$_6$)$_{0.9}$×0.4H$_2$O (KMFCN) and HC powders while using a different electrode slurry composition (KMFCN: Super P carbon: sodium carboxymethyl cellulose (Na-CMC: Sigma Aldrich) = 60:30:10, mixed in deionized water and HC:Super P carbon: Na-CMC = 80:10:10 in water, respectively). The electrode loading for KVPO was in the range (1.4-1.8 mg·cm$^{-2}$), for KMFCN - in the range (1.2-1.9 mg·cm$^{-2}$); for HC – in the range (0.6-0.9 mg·cm$^{-2}$) for electrochemical measurements in K half cells.

**Electrolyte preparation**

The carbonate-based electrolyte solution was prepared by mixing ethylene carbonate (EC: Sigma Aldrich, anhydrous, 99%) and diethyl carbonate (DEC: Sigma Aldrich, anhydrous, ≥99%) in the corresponding volume ratio, holding overnight over activated molecular sieves (Sigma Aldrich, 4 Å, 4-8 mesh). The KPF$_6$ electrolyte salt (Acros organics, extra pure, 99%) after drying at 60°C under vacuum was dissolved in the mixture to result in pristine carbonate-based electrolyte 0.5M KPF$_6$ in EC:DEC (1:1 v:v). Vinylene carbonate (VC: Sigma Aldrich, 99%) and fluoroethylene carbonate (FEC: Sigma Aldrich, 99%) were dried with activated molecular sieves overnight. The appropriate amount of VC was added to the prepared solutions to achieve 1, 2 and 4 wt.% concentrations. The same procedure was performed with FEC to attain 5 and 50 wt.% in 0.5M KPF$_6$ in EC:DEC (1:1 v:v).

The KPF$_6$ electrolyte salt (Acros organics, extra pure, 99%) after drying at 60°C under vacuum was dissolved in diethylene glycol dimethyl ether (diglyme, G2: Sigma Aldrich, anhydrous, 99.5%) to achieve concentrations of 1, 1.5, 2, and 2.5M KPF$_6$ in G2. An increase of the KPF$_6$ concentration over 2.5M resulted in non-transparent solutions indicating a solubility limit for KPF$_6$ in G2. The appropriate amount of VC was also added to the prepared ether-based solutions to achieve 0.5 and 1 wt.% concentrations.

All produced solutions were transparent with less than 30 ppm of residual water measured with a coulometric Karl Fischer titrator (Mettler Toledo).

## Characterization methods

### Raman spectroscopy

In order to study the electrolyte solution and hard carbon structure, Raman spectroscopy measurements were conducted on a DXRxi Raman imaging microscope (ThermoFisher Scientific) equipped with a 10X optical zoom and green solid-state laser ($\lambda = 532$ nm). The laser spot diameter was about 1 μm. The spectra were measured for 50 points with a laser power of 10 mW and 0.5 s exposure time in the 300-3500 cm$^{-1}$ range (2 cm$^{-1}$ spectral dispersion).

### Thermogravimetric analysis

The thermal analysis[3] was carried out with a TG-DSC STA-449 apparatus (Netzsch, Germany) under dry air flow. The powders were heated at 5-10 K/min rate in the 25-600°C temperature range.

### Specific surface area measurements

The specific surface area of HC powders was determined using Brunauer–Emmett–Teller (BET) method. BET specific surface area (SSA$_{BET}$) was measured by $N_2$ adsorption technique with a Quantachrome Instruments NOVA surface area and pore size analyzer[4].

### X-ray Powder Diffraction (XRPD)

X-ray powder diffraction (XRPD) patterns were collected using a Bruker D8 ADVANCE diffractometer (Cu-K$_\alpha$ radiation). In order to perform XRPD measurements under Ar, the cycled electrodes were placed in a special cuvette for Bruker D8 ADVANCE diffractometer in the glovebox. The background from the observed diffractograms is substracted using WinXpow software. The unit cell parameters of KMFCN and KVPO were refined using the Le Bail method implemented in the JANA2006[137] program package. The background was estimated by a set of Chebyshev polynomials, followed by the refinement of the cell parameters and the peak shapes with a pseudo-Voigt function. The $KVOPO_4$ and KMFCN structures are preserved after 30 cycles in all used electrolyte solutions.

### Scanning Electron Microscopy (SEM)

The morphology and particle size of the electrode materials were investigated by scanning electron microscopy with a ThermoFisher Quattro S FEG-SEM. In order to probe the SEI layers formed on HC negative electrodes, the samples were transferred to the SEM chamber from an Ar-filled glove box (MBraun) with a Kammrath & Weiss transfer module precluding contact with air.

---

[3] Thermal analysis was performed by Dmitry Rupasov and Stanislav Fedotov
[4] $N_2$ adsorption measurements were conducted by Polina Morozova

**Transmission Electron Microscopy (TEM)**

The samples for transmission electron microscopy (TEM) were also prepared in the Ar-filled glove box by gently grinding the electrodes in an agate mortar and dipping the lacey carbon Cu-supported grid into the electrode mass. The samples were transferred to the TEM column with a Gatan vacuum transfer holder. High resolution TEM (HR-TEM) images, high angle annular dark field scanning TEM (HAADF-STEM) images were taken with a Titan Themis Z transmission electron microscope operated at 120 kV[5]. Electron energy loss spectra (EELS) were measured in a STEM mode (STEM-EELS) with a GIF Quantum ER965 with 0.17 eV energy resolution according to full width at half maximum of the zero-loss peak. Energy-dispersive X-ray spectra in the STEM mode (STEM-EDX) were taken with a Super-X EDX system.

**X-ray Photoelectron Spectroscopy (XPS)**

The HC electrodes were retrieved from the two electrode K-half cells with corresponding $x$ M $KPF_6$ in G2 electrolyte solution after 1, 2, 3 and 30 full charge/discharge cycles. After being washed in G2 in the glovebox for 1 hour to remove $KPF_6$ traces, the samples were transferred to the spectrometer using a PHI VersaProbe vacuum vessel to prevent the exposure to the atmosphere. XPS measurements[6] were carried out using a PHI VersaProbe II spectrometer equipped with a monochromatic Al Kα X-ray source. XP spectra for C 1s, K 2p, Na 1s, O 1s, P 2s, and F 1s were acquired with an electron pass energy of 10−40 eV. The spectra were approximated with a Gaussian/Lorentzian convolution function with a Shirley background shape using the CasaXPS Software. Quantification of the composition was performed by taking into account the analyzer transmission function.

**Atomic Force Microscopy (AFM)**

In order to conduct *in situ* AFM measurements[7], the HC powder was mixed with Super P carbon (Timcal) and sodium carboxymethyl cellulose (Na-CMC, Sigma Aldrich) in the 80:10:10 mass ratio and afterwards with deionized water in a SPEX 8000M high-energy ball mill for 20 min. The resulting electrode slurry was spread on a Kapton tape and dried at room temperature overnight. Afterwards, the electrode was dried at 120°C for 12 hours. After drying the composite electrode was delaminated from the tape, embedded in a bisphenol A/F based epoxy resin (epoxy resin HT2 and hardener HT2 from R&G Faserverbundwerkstoffe GmbH (Waldenbuch, Germany)) by vacuum infusion and cured according to the specification. The sample was mechanically polished by sand paper and diamond paste and finally by the OP-S silica suspension (Struers), washed in deionized water and dried. After that the sample was fixed on a steel substrate

---

[5] HR-TEM, HAADF-STEM and STEM-EELS measurements were conducted by Artem Abakumov
[6] XPS measurements were carried out by Menghsuan Sam Pan and Elizabeth Shaw
[7] *In situ* AFM measurements were performed by Sergey Luchkin

by conductive silver paint and additionally by the TorrSeal epoxy along the perimeter. The utilized AFM electrochemical cell was elaborated in our research group[138]. Figure 3.1 depicts the scheme of the AFM cell preparation. As it was described above, the sample (1) is embedded into epoxy resin (2), polished/cross-sectioned (3), connected to the substrate by a conductive silver or carbon paint (4), and installed into an AFM. The cantilever is positioned above the sample (5), and the electrolyte is injected through the tubing to form the meniscus between the sample and the cantilever holder (6).

*In situ* AFM measurements were made on a Cypher ES AFM (Asylum Research, Oxford Instruments) installed in an Ar filled glove box using a liquid perfusion cantilever holder and a soft PNP-TR Pyrex-Nitride Probe with 67 kHz resonance frequency and 0.32 N/m spring constant. Stiffer cantilevers affected SEI growth by dragging it off from the scan area. Thin (<50 µm) K electrode serving as a reference and a counter electrode was inserted between the cantilever holder and the sample, which was the working electrode. The cantilever was brought to 100 µm above surface. The electrolyte was injected between the cantilever and the sample until it formed a meniscus between the epoxy and the fused silica window of the cantilever holder. After that the cantilever was landed on the sample surface in a semicontact mode. A single AFM scan acquisition took 340 sec. AFM slow scan direction was from top to bottom. The cyclic voltammetry was made by BioLogic SP-150 potentiostat.



Figure 3.1. Schematic illustration of AFM electrochemical cells[138].

**Electrochemical measurements**

For electrochemical measurements, two-electrode Swagelok electrochemical cells with a working volume of 90 µl and glass-microfiber separator (AHLSTROM, Munktell) were assembled under argon atmosphere in an Ar-filled glovebox (MBraun, $H_2O$ < 0.1 ppm, $O_2$ < 0.1 ppm).

Electrochemical data were registered with a Biologic VMP-3 potentiostat/galvanostat at room temperature. The cells with three combinations of working/counter electrodes were implemented: K half-cell with K metal as the counter electrode (CE) and one of the prepared electrodes (KVPO, KMFCN or HC) as the working electrode (WE); K full cell (CE – the HC electrode, WE – the KMFCN electrode); K symmetric cell (CE, WE – K metal). The cyclic voltammetry (CV) curves accompanying with the AFM measurements were registered at a scan rate of 1 mV·s-1. The cyclic voltammetry curves in K half cells were registered at a scan rate of 100 µV/s. The cut-off current density value was defined as 10 times the background current density constituting 0.08 µA/cm$^2$ in order to determine the oxidation potential of the Al current collector. Galvanostatic measurements were performed with different electrolyte concentrations in K half cells and K full cells at a 0.1C and 0.6C charge/discharge rate respectively in the potential range corresponding to the specific WE. In the case of full cells, the anode pre-cycling technique was conducted to form the stable SEI on the electrode surface. The hard carbon anode was cycled down to 0.01 V vs K$^+$/K, then up to 2.5 V vs K$^+$/K and, finally, down to 0.1 V vs K$^+$/K at a 0.1C charge/discharge rate in a K half cell. Subsequently, the pre-cycled anode was extracted from the cell and assembled with KMFCN cathode and fresh electrolyte in a new cell in the glovebox. Potentiostatic electrochemical impedance spectra (PEIS) were registered in the K symmetric cells at the open circuit voltage in the 1MHz-100mHz frequency range with 5 mV peak-to peak alternating voltage, and then analyzed using the MEISP software.

**Chapter 4. Exploring positive and negative electrodes for K⁺-ion batteries.**

**Effect of synthesis conditions on Hard Carbon properties**

The first research objective is aimed to probe the relation between synthesis conditions, hard carbon particle morphology and resulted electrochemical performance in PIBs. In Chapter 2 the impact of HC preparation parameters on particle morphology and intrinsic properties is discussed. HC particle size influences the electrochemical properties since the enhanced specific surface area increases the irreversible capacity loss due to the surface film formation and, therefore, results in the reduced CE, though large particle size accompanying the lower specific surface area may hinder K⁺-ion diffusion in HC structure. The spherical shape of HC particles seems to be beneficial in terms of high reversible capacity and straightforward adjustment of microsphere diameter via synthesis parameters. Generally, HC microspheres are obtained from simple sugars[112,122]. D-glucose-derived HC samples with different distributions of sphere diameters were obtained under various synthesis conditions to examine the relation between the particle morphology and the resulted electrochemical performance.

One may tune the hard carbon morphology through varying hydrothermal synthesis conditions[107,139,140] whereas the high-temperature annealing affects the graphitization degree[141], the specific surface area, the space between graphene layers, and the amount of carbon defects[117,124]. The various synthesis parameters were applied (the designation of **HC1-HC7** samples with respective synthesis conditions could be found in table 4.1): the pre-heating temperature $T^I$ (180 ° C and 200 ° C) and duration/ residence time (8 h, 16 h, 24 h) of HTC, a set of precursors (water solution of [D-glucose + pectin + polytetrafluoroethylene] and a water solution of [D-glucose + pectin + citric acid]) and the temperature of the subsequent annealing $T^{II}$ (1200 °C and 1500 °C). In addition, the rinsing intermediate carbonization product with ethanol after the hydrothermal synthesis and before the high-temperature annealing occurs to be an important step. Figure 4.1 illustrates the difference between samples obtained under the same conditions. Without ethanol rinsing step the hollow microspheres of HC with a particle size less than 0.5 µm (hereafter they are -called "nanosized particles" or "nanospheres") prevail in the HC powder. HC nanospheres might enlarge the irreversible capacity loss during first formation cycles of K⁺-ion cell operation owing to enhanced specific surface area. On the other hand, the fraction of "nanosized" HC particles is reduced in the sample that was preliminarily rinsed with ethanol before the high-temperature annealing at 1500°C.

Table 4.1. Comparative table of properties of hard carbon samples obtained under various synthesis conditions. The electrochemical measurements were conducted in K half cells with a 0.5 M KPF6 / EC: DEC electrolyte solution (1: 1 by volume ratio)

| Synthesis conditions | Particle size, μm | Specific discharge capacity at the 1st cycle, mA·h·g⁻¹ | CE of the 1st cycle, % | Capacity retention after 30 cycles, % |
|---|---|---|---|---|
| **HC1:** Hydrothermal synthesis (D-glucose + pectin + polytetrafluoroethylene, 180 ° C, 8 h), high-temperature annealing (1200 ° C) | 0.16 -2.1 | 223 | 19.6 | 1.1 |
| **HC2:** Hydrothermal synthesis (D-glucose + pectin + polytetrafluoroethylene, 180 ° C, 16 h), high-temperature annealing (1200 ° C) | 0.14 - 15.8 | 199 | 70.8 | 29.6 |
| **HC3:** Hydrothermal synthesis (D-glucose + pectin + polytetrafluoroethylene, 180 ° C, 8 h), high-temperature annealing (1500 ° C) | 0.12 – 10.7 | 223 | 45.5 | 43.2 |
| **HC4:** Hydrothermal synthesis (D-glucose + pectin + polytetrafluoroethylene, 180 ° C, 16 h), high-temperature annealing (1500 ° C) | 0.13 – 15.7 | 221 | 64.3 | 57.9 |
| **HC5:** Hydrothermal synthesis (D-glucose + pectin + polytetrafluoroethylene, 180 ° C, 24 h), high-temperature annealing (1500 ° C) | 0.14 - 14.2 | 202 | 62.3 | 82.2 |
| **HC6:** Hydrothermal synthesis (D-glucose + pectin + citric acid, 180 ° C, 16 h), high-temperature annealing (1500 ° C) | 0.44 – 4.3 | 250 | 56.7 | 92.0 |

| HC7: Hydrothermal synthesis (D-glucose + pectin + citric acid, 200 °C, 16 h), high-temperature annealing (1500 °C) | 2.3 – 32.4 | 181 | 67.3 | 89.0 |
|---|---|---|---|---|

Figure 4.2 shows the morphology and size distribution of D-glucose-derived HC microspheres obtained under various conditions of the hydrothermal carbonization. All HC particles resemble spherical shape. The particle size distribution was calculated using ImageJ software from a number of SEM images. The applied synthesis conditions alter the size distribution and the content of "nanospheres" in the resulting HC samples. The particle diameter distribution might give a clue about the content of HC nanospheres. Assuming the analyzed SEM images reflect the average size distribution in whole powder volume, one could estimate the fraction of nanosized particles. It decreased in order HC1>HC2>HC6>HC4>HC5>HC7 (corresponding to 89.0%>60.98%>14.5%>6.4%>2.3%>0% respectively). Both HC powders obtained upon annealing at $T^{II}$=1200°C contain the predominant amount of "nanosized" HC spheres. The increase in the residence time from 8 hours to 16 hours results in the broader particle size distribution and the enhanced number of larger particles. The elevated annealing temperature $T^{II}$=1500°C leads to the drastic diminution of "nanosized" HC particles. The further raised HTC duration of 24 hours causes the wider distribution of HC microsphere diameter in the range of 2-10 µm. The "nanosized" HC particles disappear with the substitution of polytetrafluoroethylene with citric acid $C_6H_8O_7$. However, the average diameter of HC microspheres derived from aqueous solution with citric acid (pH~2.8) decreased down to ~0.79 µm. The enhanced hydrothermal temperature $T^{I}$=200°C results to the broad distribution of larger HC particles in the range of 4-10 µm.
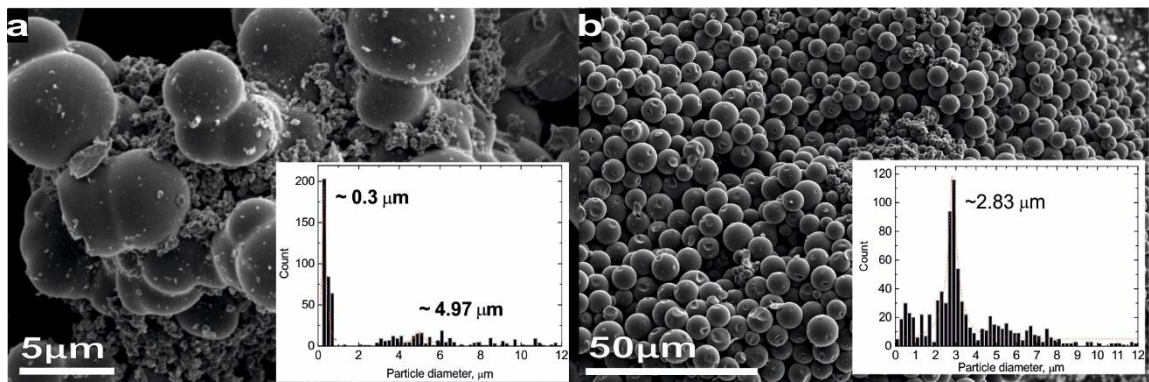


Figure 4.1. SEM images of **HC4** powders obtained: a) without ethanol rinsing and b) with ethanol rinsing. Insets depict the particle diameter distribution.

The SEM results are consistent with the values of the specific surface area measured by the BET method (Table 4.2). The lower specific surface area of 57.18 $m^2 \cdot g^{-1}$ for **HC2** ($T^{I}$=180°C;

t=16h; $T^{II}$=1200°C) compared to 317.02 $m^2 \cdot g^{-1}$ for **HC1** ($T^{I}$=180°C; t=8h; $T^{II}$=1200°C) stems from the formation of larger HC particles owing to the raised residence time of HTC step. A decrease in the "nanospheres" content is accompanied by reduction of the specific surface area. But it's not the single reason manipulating the specific surface area. Enhanced $T^{II}$=1500°C results in the declined specific surface area. **HC4** sample containing lower fraction of nanospheres than **HC6** exhibit higher specific surface area tentatively owing to the contribution of mesopores in HC walls. Despite the HC particle diameter of less than 1 μm, the lowest specific surface area value of 5.74 $m^2 \cdot g^{-1}$ is observed for the **HC6** ($T^{I}$=180°C; t=16h; $T^{II}$=1500°C) sample derived from aqueous solution containing citric acid. So, the improved values of CE originated from the diminished irreversible capacity loss are anticipated for this sample. Nevertheless, matching of microscopic and electrochemical data is required for selecting the most appropriate HC since the possible kinetic difficulties might arise because of large HC spheres.
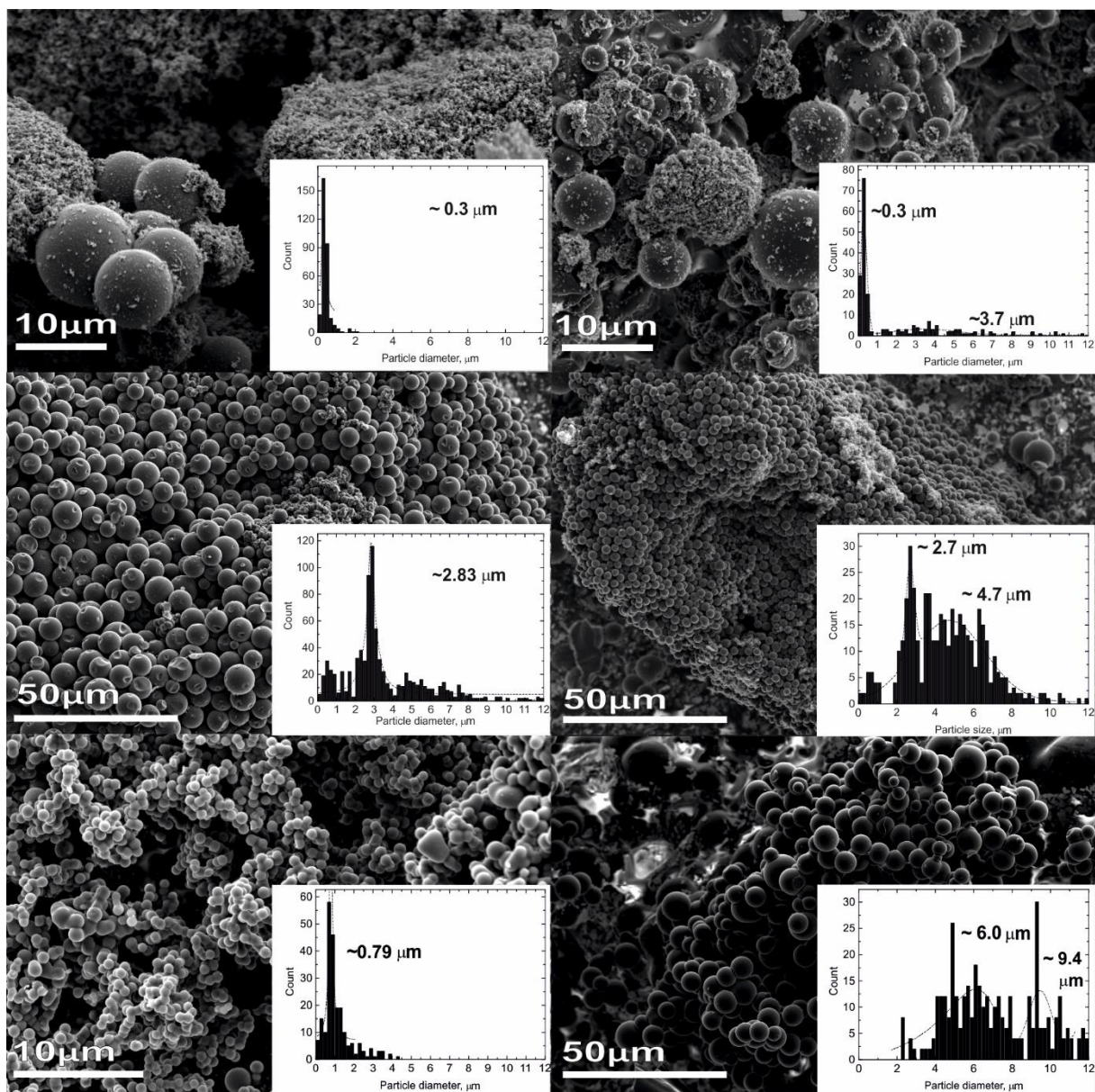
Figure 4.2. SEM images of a) **HC1**; b) **HC2**; c) **HC4**; d) **HC5**; e) **HC6** and f) **HC7** powders. Insets depict the particle diameter distribution.

Table 4.2. Specific surface area values obtained by using the BET method for the HC samples produced under various synthesis conditions.

| Synthesis conditions | $SSA_{BET}$, $m^2 \cdot g^{-1}$ |
|---|---|
| **HC1:** Hydrothermal synthesis (D-glucose + pectin + polytetrafluoroethylene, 180 ° C, 8 h), high-temperature annealing (1200 ° C) | 317.02 |
| **HC2:** Hydrothermal synthesis (D-glucose + pectin + polytetrafluoroethylene, 180 ° C, 16 h), high-temperature annealing (1200 ° C) | 57.18 |

| | |
|---|---|
| **HC4:** Hydrothermal synthesis (D-glucose + pectin + polytetrafluoroethylene, 180 ° C, 16 h), high-temperature annealing (1500 ° C) | 26.56 |
| **HC6:** Hydrothermal synthesis (D-glucose + pectin + citric acid, 180 ° C, 16 h), high-temperature annealing (1500 ° C) | 5.74 |

The results of galvanostatic cycling of HC electrodes in K cells with conventional carbonate-based electrolyte [0.5 M $KPF_6$ / EC: DEC (1: 1, v:v)] at C/10 rate are shown in Figure 4.3. The charge/discharge curves exhibit sloping profile at 1.3−0.3 V *vs* $K^+$/K and plateau regions at 0.18 and 0.29 V *vs* $K^+$/K during the intercalation and deintercalation respectively. The SEI layer formation and emerging electrode polarization account for the difference in the shape of charging curve at the 1st cycle. It should me mentioned, that the K metal as negative electrode contributes to the irreversible capacity loss in all K cells due to the formation of unstable SEI layer. The complete degradation of K cell with **HC1** electrode upon 30 cycles originates from the continuous electrolyte decomposition on particles with the enlarged surface area. The irreversible capacity loss correlates with the fraction of "nanosized" HC microspheres. The diminution of the "nanosized" particles improves the CE values at the 1st cycle and cycle stability. The capacity retention increases up to 92%. Moreover, the surface induced capacity, corresponding to the slope region at the galvanostatic curves, reduces with the decreased specific surface area value. The K cells with **HC6** and **HC7** deliver the best capacity retention of 92 and 89%, respectively. The specific discharge capacity at the 1st cycle varies in the range of 180-250 mA·h·$g^{-1}$.
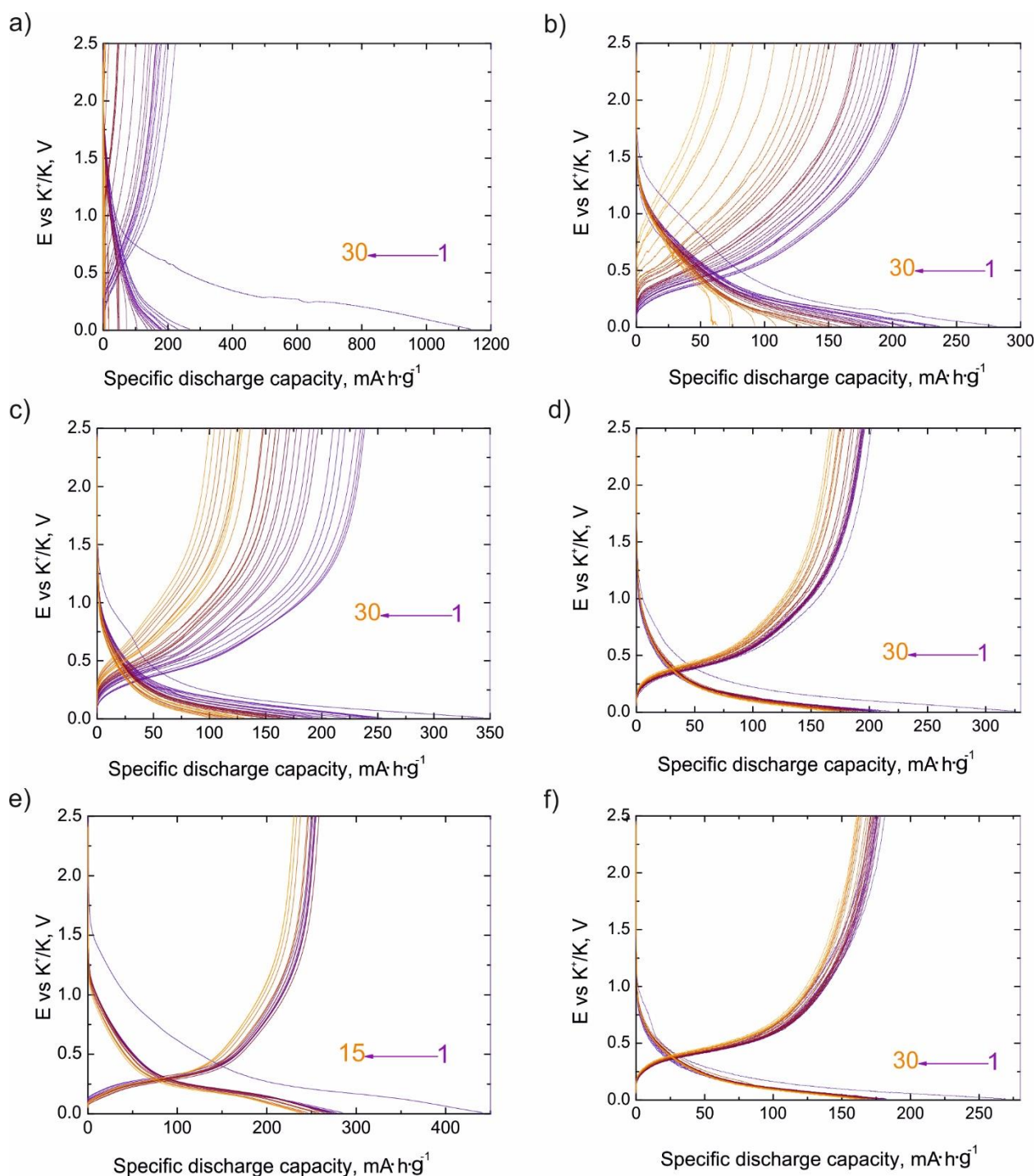
Figure 4.3. Galvanostatic curves measured for $K^+$-ion cells with a [0.5 M $KPF_6$ / EC: DEC (1: 1 by volume ratio)] electrolyte and with a) **HC1** ; b) **HC2**; c) **HC4**; d) **HC5**C; e) **HC6** and f) **HC7** as working electrode

The comparative table 4.1 demonstrates that the enhanced content of "nanospheres" leads, as expected, to lower CE values during the first formation cycles and to a faster degradation of the PIB with the [0.5 M $KPF_6$ / EC: DEC (1: 1 by volume ratio)] electrolyte. Therefore, the "nanosized" particles should be absent in HC powders utilized in further study. It might be attained via introducing the step of ethanol rinsing, via the application of prolonged residence time ($\geq$16

hours) and enhanced annealing temperature ($T^{II}$=1500°C), and via the substitution of polytetrafluoroethylene by citric acid. The **HC4** and **HC6** samples exhibit the better combination of the specific capacity (221 mA·h·g$^{-1}$ and 250 mA·h·g$^{-1}$) and CE values at the 1$^{st}$ cycle (64.3% and 56.7%) compared to other samples. However, **HC7** sample delivers the high CE value of 67% at the first cycle with capacity retention of 89% after 30 cycles. Hence, HC powders with decreased content of nanosized particles and annealed at higher temperature of 1500°C deliver the best electrochemical properties. The best combination of synthesis conditions comprise the HTC of (D-glucose + pectin + citric acid, 180 ° C, 16 h) with the subsequent high-temperature annealing at T=1500 °C.

**Characterization of the HC negative electrodes**

The **HC4** microspheres with the diameter distribution in the range of 0.13-15.7 μm were utilized to probe the surface film formation. The observed Raman spectrum (Figure 4.4) exhibits so-called D-band (the defect-induced band) and G-band (the crystalline graphite band) peaks at ~1344 cm$^{-1}$ and ~1585 cm$^{-1}$ respectively being characteristic of the HC structure. The G-band represents sp$^2$ vibration in graphite-like materials, whereas the D-bands emerges due to the double resonance Raman process (see Chapter 2). However, the double resonance Raman process is induced by defects and, thereby, implicitly associated with their presence. Herein, the ratio of D-band and G-band's intensity ($I_D/I_G$) is calculated to be 1.2, indicating defective structure on a large scale. These defects might contribute to the surface-driven storage of K$^+$-ions and, hence, to the sloping profile of galvanostatic curves above 0.3 V *vs* K$^+$/K.
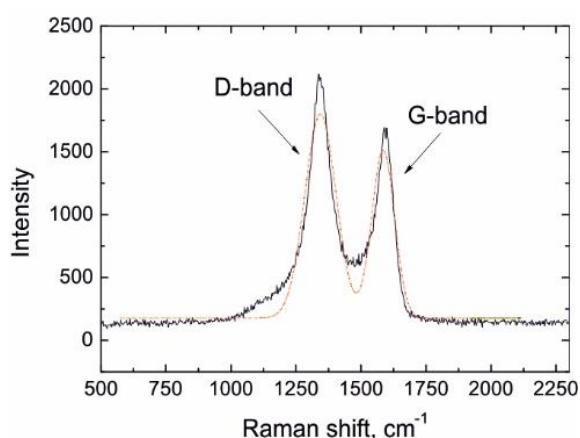


Figure 4.4. Raman spectrum of **HC4** powder

HAADF-STEM image in Figure 4.5a allows identifying the components of the HC-based electrodes. The HC spheres appear prominently bright due to their large thickness. The spheres are in contact with porous network structures of the carbon black additive. STEM-EDX analysis of the HC sphere (Figure 4.5b,c,d) reveals no side elements except oxygen and argon. Apparently Ar is trapped during final annealing of the HC spheres at 1500 ℃ in Ar flow. The $K^+$-ion adsorption at the surface oxygen atoms might also promote the surface induced capacitive process during $K^+$-ion intercalation into HC framework.

Figure 4.5. Microstructure of the pristine HC electrode: a) HAADF-STEM image of the HC microsphere with attached carbon black forming a porous network structure; b, c) HAADF-STEM image of the edge of HC microsphere and corresponding color-coded EDX map demonstrating distribution of oxygen and argon. The surface of the sphere is slightly oxidized whereas Ar is more homogeneously distributed inside the sphere; d) typical EDX spectrum demonstrating presence of O and Ar.

**KMFCN cathode material characterization**

In Chapter 2 the advantages of the PBA utilization in PIBs provided by the 3D open framework are discussed. Mn-contained PBA with general chemical formula $K_2Mn[Fe(CN)_6]\times nH_2O$ delivers better electrochemical performance in terms of reversible capacity values, operating potential and cycling stability[12,17,44,51] and, hence, is beneficial for the development of full K cell. The cathode powder was synthesized via precipitation technique described in Chapter 3. The obtained particles possess the size less 400 nm (Figure 4.6a). EDX analysis combined with the thermal analysis results reveals the chemical composition of $K_{1.44}Mn(Fe[CN]_6)_{0.9}\times 0.4H_2O$ (KMFCN). The cyclic voltammogram of KMFCN was measured in two-electrode K half cell with conventional carbonate-based electrolyte [0.5M $KPF_6$ / EC:DEC (1:1, v:v)] in the potential range of 2.5-4.5 V $vs$ $K^+/K$ at scan rate of 100 $\mu V \cdot s^{-1}$ (Figure 4.6c). It shows three distinguishable peaks: a pair of peaks is located at 3.75 V and 4.24 V $vs$ $K^+/K$ on cathodic and anodic scans, respectively, which relate to $Fe^{3+}/Fe^{2+}$ redox. The peak-to-peak distance being more 400 mV originates from the formation of thick and resistive surface layers on electrodes causing a huge polarization in carbonate-based electrolyte. The appearance of a peak at 3.87 V $vs$ $K^+/K$ on cathodic scan corresponds to the $Mn^{3+}/Mn^{2+}$ redox. Since the shape and width of cathodic and anodic peaks differ, the second anodic peak might not be distinctive on cathodic scan. The specific discharge capacity of KMFCN is 112 $mA \cdot h \cdot g^{-1}$.
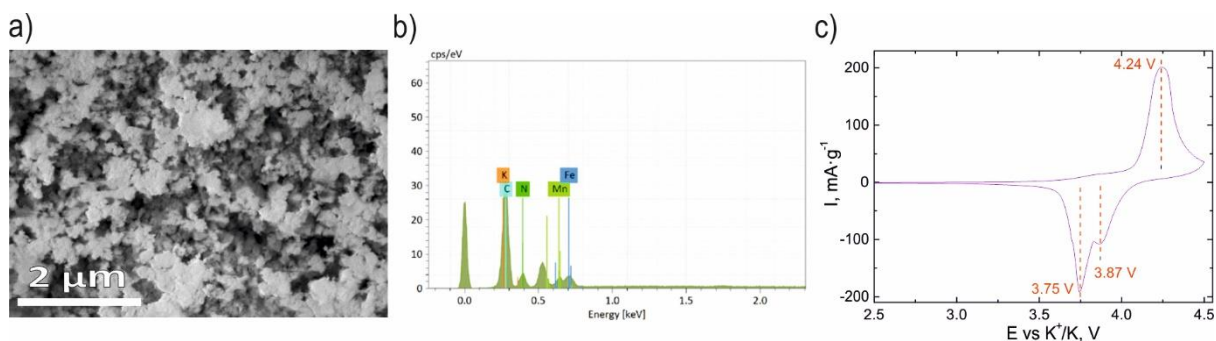


Figure 4.6. a) The SEM image and b) EDX spectra of the KMFCN powder; c) normalized cyclic voltammetry curve measured at scan rate of 100 $\mu V \cdot s^{-1}$ of K cell with KMFCN positive composite electrode and [0.5M $KPF_6$ / EC:DEC(1:1, v:v)] electrolyte solution .

**$KVOPO_4$ cathode material characterization**

$KVOPO_4$ (KVPO) was selected to examine with electrolytes elaborated in presented research for PIBs as the positive electrode with polyanionic structure. KVPO was prepared by thermal decomposition of the hydrothermally synthesized $K_3(VO)(HV_2O_3)(PO_4)_2(HPO_4)$ ( = "$KVOPO_4\times 1/3H_2O$") precursor as described in Chapter 3. KVPO exhibits $KTiOPO_4$-type structure comprising $VO_6$ octahedra and $PO_4$ tetrahedra[67]. Figure 4.7 demonstrates XRPD patterns

of $K_3(VO)(HV_2O_3)(PO_4)_2(HPO_4)$ and KVPO compounds refined using the Rietveld method. XRPD profile of KVPO could be indexed in orthorhombic unit cell ($a$=12.8105 ± 0.0003 Å; $b$=10.44511 ± 0.00017 Å; $c$=6.36641 ± 0.00012 Å; α=β=γ=90°) with space group $Pn2_1a$. The calculated lattice parameters coincide with the published data[67].
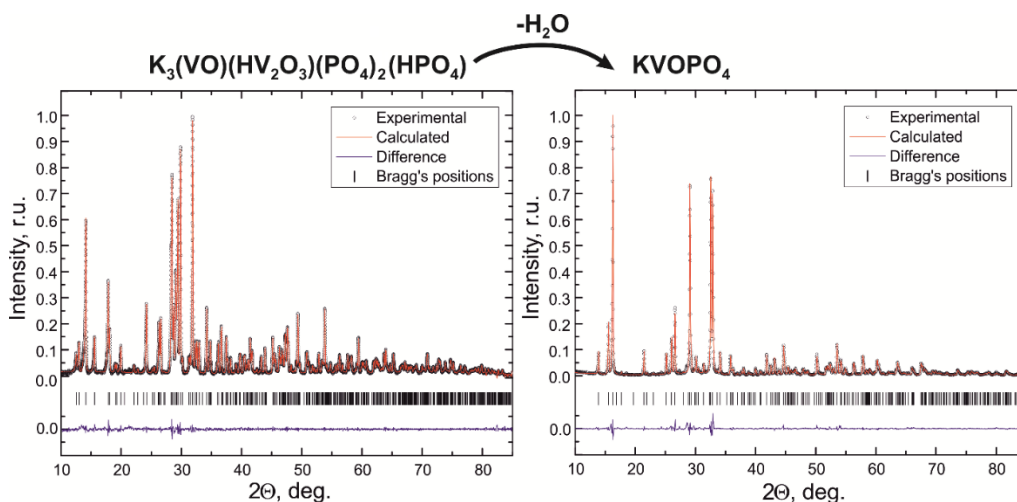


Figure 4.7. The experimental, calculated and difference XRPD profiles for the $K_3(VO)(HV_2O_3)(PO_4)_2(HPO_4)$ precursor (left) and the synthesized $KVOPO_4$ powder (right) after the Rietveld refinement.

The $KVOPO_4$ powder consists of particles with the average size of about 1 μm that agglomerate into larger clusters with the average size of about 20 μm (Figure 4.8a). The electrochemical properties of KVPO positive electrode were measured in two-electrode K cell with conventional carbonate-based electrolyte [0.5M $KPF_6$ / EC:DEC (1:1, v:v)] in the potential range of 2.0-4.5 V $vs$ $K^+/K$ (Figure 4.8b,c). The cyclic voltammogram demonstrates two pairs of peaks located at 2.54/2.93 V $vs$ $K^+/K$ and at 3.99/4.23 V $vs$ $K^+/K$ on cathodic/anodic curve parts respectively (Figure 4.8b). The additional peak emerges at 3.82 V $vs$ $K^+/K$ on anodic scan. The electrode polarization that accounts for the enlarged peak-to-peak distance is also evidenced in K half cell with the KVPO positive electrode. The KVPO cathode delivers the specific discharge capacity of 57 mA·h·g$^{-1}$ accompanied by CE value of 47% at the first cycle at current density C/20 (Figure 4.8c). The capacity retention is observed to be 63 % upon the increase in the cycling rate from C/20 to 5C despite the enough large size of KVPO particles. The galvanostatic curves exhibit stepwise profile corresponding to $V^{4+}/V^{5+}$ redox. The enhanced cut-off potential up to 4.8 V $vs$ $K^+/K$ causes the poor performance of K cell with KVPO positive cathode that might stem from the electrolyte oxidation. The elaborated electrolyte stability can facilitate the electrochemical activity of more $K^+$-ions resulting in the increased reversible capacity values.
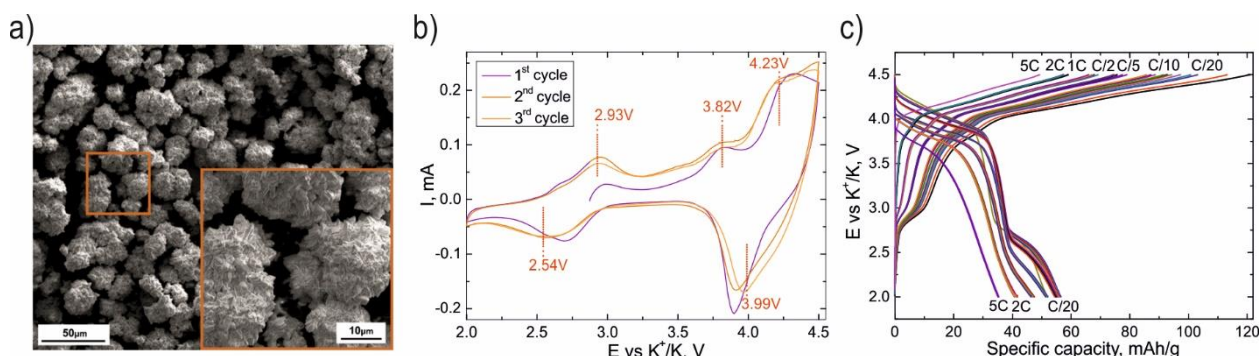
Figure 4.8. a) The scanning electron microscopy (SEM) image of the KVOPO$_4$ sample illustrating the material's morphology; b) cyclic voltammetry curves measured at scan rate of 100 µV·s$^{-1}$ and c) rate performance test of K cell with KVOPO$_4$ positive composite electrode and [0.5M KPF$_6$ / EC:DEC(1:1, v:v)] electrolyte solution .

**Conclusion**

The electrode materials for further research were synthesized and characterized. The K$_{1.44}$Mn(Fe[CN]$_6$)$_{0.9}$×0.4H$_2$O sample comprising particles with a size less than 400 nm possesses the advantages as the positive electrode in PIB owing to the open framework structure. The synthesized KVOPO$_4$ compound, exhibiting the KTiOPO$_4$-type structure, could not compete with other cathodes for K cells in terms of specific discharge capacity values. However, it could still serve as the positive electrode with polyanionic structure to examine various electrolyte compositions. The hard carbon microspheres obtained upon the hydrothermal carbonization technique (T$^I$=180°C; t=16 h) with subsequent annealing at T$^{II}$=1500°C exhibit the specific discharge capacity values in the range of 220-250 mA·h·g$^{-1}$ in K half cells with [0.5 M KPF$_6$ / EC: DEC (1: 1 by volume ratio)] electrolyte. The presence of so-called "nanosized" particles significantly contributes to the irreversible capacity loss at the first cycles. The enhanced content of "nanospheres" leads to lower CE values during the first formation cycles and to a faster degradation of K cells. The presence of ""nanosphere"" particles might be eliminated via the addition of ethanol rinsing intermediate step, the increased annealing temperature, appropriate choice of precursors, and the variation of HTC parameter. The optimized synthesis conditions enhance the CE value up to 67% at the first cycle and the capacity retention up to 89% upon 30 cycles.

## Chapter 5. Electrolyte salt concentration effect on electrode performance in diglyme-based K$^+$-ion batteries

### Aluminum current collector passivation

An important issue limiting practical implementation of the electrolyte is its stability against current collector corrosion within the working potential range. In order to estimate the potentials at which the Al current collector corrosion occurs, two-electrode K half-cells with Al working electrodes and KPF$_6$/G2 electrolyte solutions of different KPF$_6$ concentrations were assembled. The Al surface passivation by the PF$_6^-$ anion was described earlier[142] and was also observed in all our experiments: the reduced current density value in the second cycle in comparison with the first cycle indicates a slower rate of Al oxidation due to the passivation layer formation (Figure 5.1a). Enhanced electrolyte stability against Al current collector corrosion was obtained upon increasing the KPF$_6$ salt concentration (Figure 5.1b), which is in line with that reported for Li-ion batteries[143,144]. Thus, [2.5 M KPF$_6$/G2] electrolyte solution can be utilized with positive electrodes and, hence, in K full cells. The origin of the improved electrolyte stability against Al current collector oxidation with salt concentration increase should be identified. So, Raman measurements to examine the spatial organization of the ions and molecules in the solution were performed.
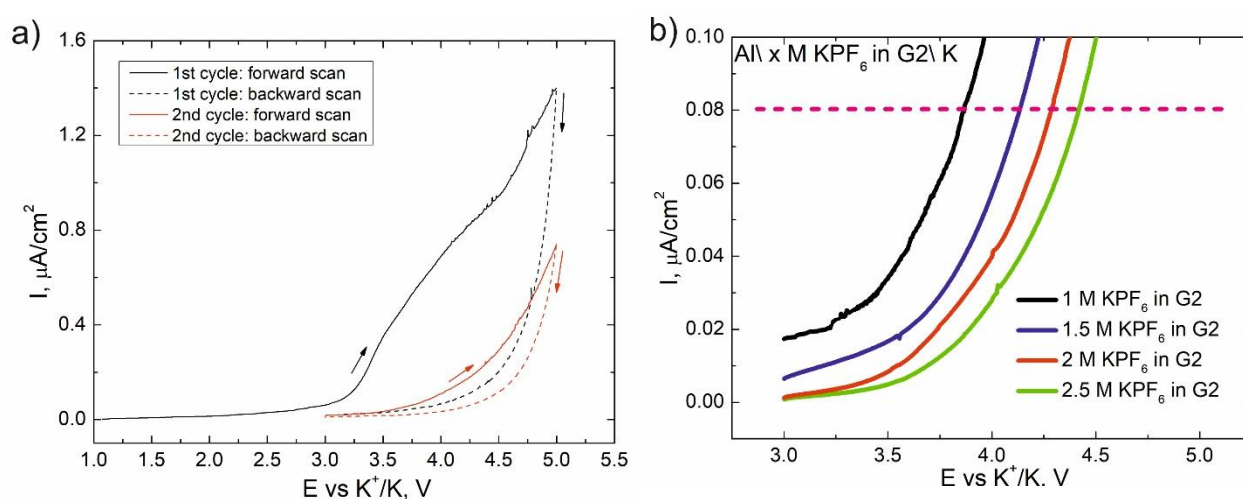
Figure 5.1. a) Cyclic voltammetry performed for K half-cell with aluminum working electrode in 1M KPF$_6$/G2 at 100 µV/s scan rate; b) cycling of the K half-cell with different electrolyte concentrations up to 5.3 V vs K$^+$/K representing the electrolyte stability against aluminum current collector corrosion. The cut-off current is 0.08 µA/cm$^2$ (being 10 times higher than the background current).

### Spatial organization of electrolyte solutions with different salt concentrations

In order to probe the spatial organization of the ions and molecules in the solution (often referred to as "solution structure"), the Raman spectroscopy measurements were conducted on pure

diglyme and KPF$_6$/G2 electrolyte solutions with different salt concentrations. The obtained spectra reveal a set of characteristic bands at 800-860 cm$^{-1}$, a so-called "breathing mode"[145,146], corresponding to the combination of the C–O–C stretching and CH$_2$ rocking modes of the solvent molecules (figure 5.2a). The Raman spectrum of pure diglyme exhibits 3 overlapping peaks residing at ~ 805, 825 and 850 cm$^{-1}$ as previously reported[145,147,148]. Two additional peaks of "perturbed" solvent molecules at 840 and 864 cm$^{-1}$ emerge simultaneously for all the KPF$_6$/G2 solutions as a result of the blue shift of the vibrational band due to the ion-dipole attraction between the dissociated K$^+$ ion and the carbonyl oxygen of the solvent molecule[148]. The mentioned shift is much smaller compared to that for the LiPF$_6$/G2 solutions[145,149] due to a weaker interaction between K$^+$ ions and carbonyl oxygens (the weaker ion-dipole binding arises from the less charge density due to the larger radius of K$^+$-ion compared to Li$^+$). According to the reported data[148], the K$^+$-ion has two feasible types of a 6-fold coordination with the solvent molecules and PF$_6^-$ ions in the diglyme solution: namely the contact ion pair (CIP-III) and solvent-separated ion pair (SSIP) associates. CIP-III implies the K$^+$ cation to be coordinated to a single PF$_6^-$ anion through three fluorine atoms and to a single diglyme molecule through three oxygen atoms (Figure 5.2b, left). In SSIP, it is coordinated to a pair of diglyme molecules through six oxygen atoms (Figure 5.2b, right).

The peak at 740 cm$^{-1}$ corresponds to the P-F stretching of the uncoordinated PF$_6^-$ [149] while its shift becomes a distinctive feature indicating the bonding formation between the anion and K$^+$ ions through fluorine atoms. As it shows no significant shift (Figure 5.2a), we can infer that: (i) no cation-anion aggregates (PF$_6$-anion interacting with two or more K$^+$-ions) formed as reported for concentrated electrolytes[149–151]; (ii) herein, we cannot definitely distinguish between the CIP-III and SSIP associates because the reported theoretical peak position difference is less than 1 cm$^{-1}$ (note that spectral dispersion is 2 cm$^{-1}$).

As the "breathing mode" consists of five overlapping peaks, the peak deconvolution using a Lorentzian function was executed to quantify the proportions of free and coordinated solvent molecules (figure 5.2c; figure 5.3, table 5.1). With increasing salt concentration, the total integral intensity of the "perturbed" peaks enhances, and that of "unperturbed" peaks declines indicating a reducing number of free solvent ("unperturbed") molecules. The redistribution of integral intensities for the peaks of the same type (unpertubed or perturbed) might be connected with specific interactions between ions and solvent molecules[152].

Thus, we demonstrate a decrease of the free solvent molecule population upon increasing the salt concentration in the K$^+$-based electrolytes similar to that reported for other non-aqueous Li$^+$-based electrolyte solutions[143,144,153,154] which eventually enhances the oxidation potential of the electrolyte. Moreover, the preferential reduction of PF$_6^-$ anion interacting with K$^+$-ions results in

the anion-derived SEI[153]. Furthermore, the formation of the passivation layer on the Al surface occurs due to reduced solubility of $AlF_3$ in electrolytes with less free solvent molecules resulting in lowering Al current collector corrosion[143,144]. Hence, a better electrochemical performance is anticipated due to formation of a stable SEI layer and suppression of the Al oxidation with increasing electrolyte concentration. Thus, the influence of the electrolyte compositional and structural changes as a function of the salt concentration on the electrochemical behavior of the $K^+$-ion cells is important to resolve as discussed below.
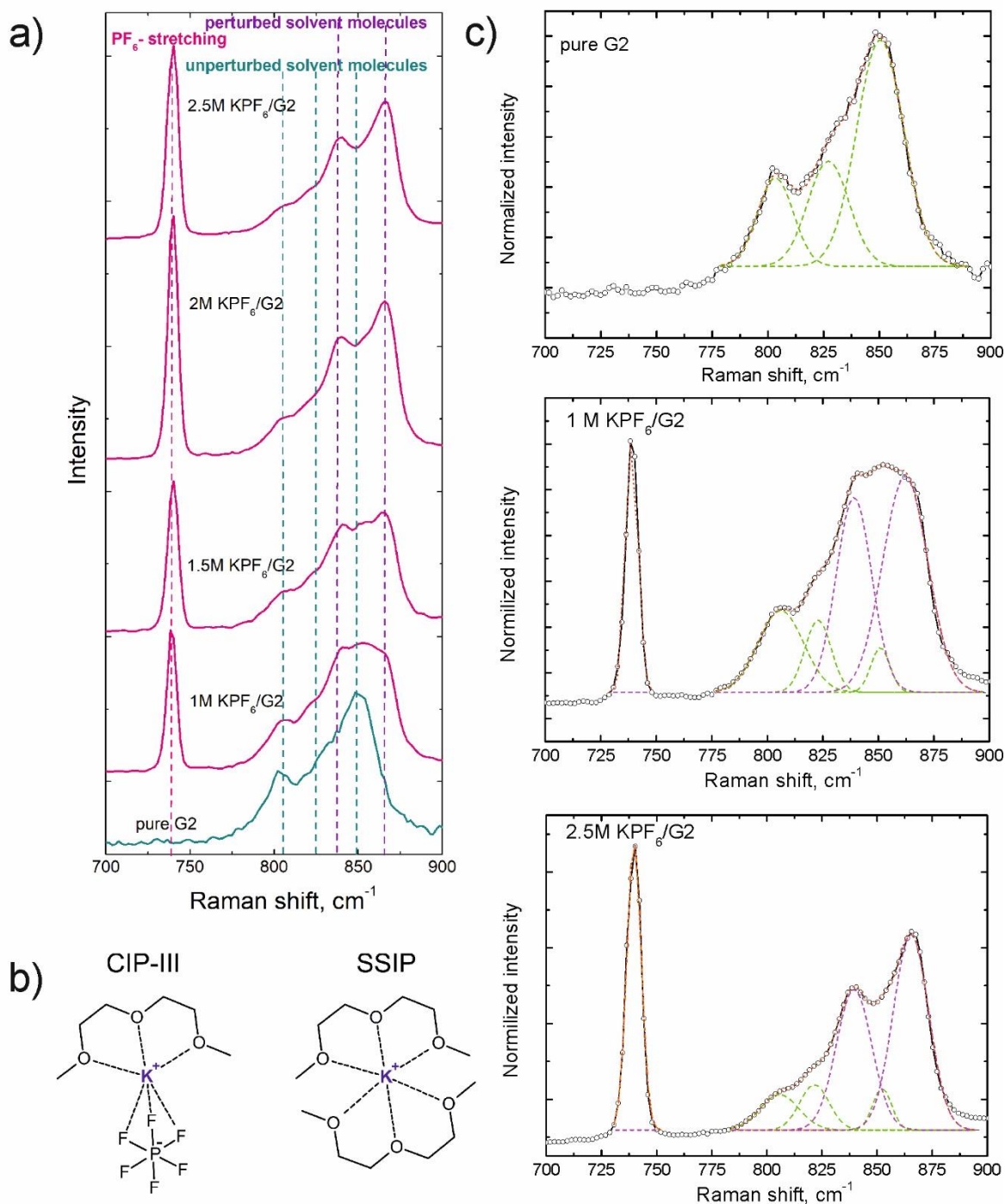


Figure 5.2. a) Raman spectra of the diglyme-based electrolytes with different $KPF_6$ salt concentrations. b) Representation of the anticipated solvated $K^+$-ion coordinations as contact-ion-

pairs (CIP) and solvent-separated ion pair (SSIP) associates. c) Deconvolution of peaks at the breathing mode (green dash lines correspond to the unperturbed solvent molecules and violet dash lines – to the perturbed ones).
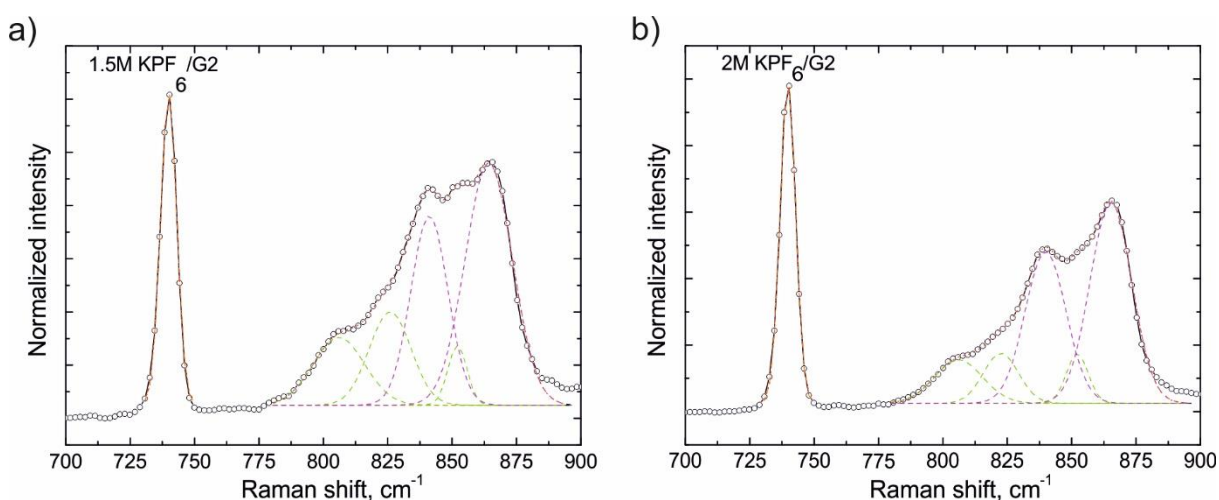


Figure 5.3. Deconvoluted Raman spectra of a) 1.5M $KPF_6$/G2 and b) 2M $KPF_6$/G2 electrolyte solutions.

Table 5.1. The fractions of the calculated integral intensities of deconvoluted peaks from Raman spectra corresponding to perturbed and unperturbed solvent molecules for the electrolytes with different salt concentration.

| Electrolyte solution | 1M $KPF_6$/G2 | 1.5M $KPF_6$/G2 | 2M $KPF_6$/G2 | 2.5M $KPF_6$/G2 |
|---|---|---|---|---|
| Fraction of the unperturbed solvent molecules, % | 25 | 21 | 16 | 15 |
| Fraction of the perturbed solvent molecules, % | 75 | 79 | 84 | 85 |

**KVPO cathode performance in diglyme-based electrolyte**

Two-electrode half-cells with KVPO working electrodes and diglyme-based electrolytes with different $KPF_6$ salt concentration (1M; 1.5M; 2M; 2.5M) were assembled and cycled at a 0.1C rate (13.3 $mA \cdot g^{-1}$ corresponding to the theoretical capacity of 133 $mA \cdot g^{-1}$) in the 2.5-4.5 V *vs* $K^+$/K potential range for 30 cycles. According to the XRPD data measured for the pristine and cycled electrodes, the KVPO structure is preserved (Figure 5.4, Figure A1, Table A1).

Figure 5.4. XRPD patterns for KVOPO$_4$ pristine electrodes and electrodes on Al foil cycled upon 30 cycles in electrolytes with different salt concentrations (* - peaks correspond to conductive additive being present in the cathode composite; # - peaks correspond to the KPF$_6$ salt crystallized at the electrode surface after galvanostatic measurements).

The half-cell with the 2M KPF$_6$/G2 electrolyte solution exhibits the highest initial discharge specific capacity (53 mAh·g$^{-1}$) and good capacity retention (81%) after 30 cycles at 0.1C charge and discharge rates (Figure 5.5a,b). The delivered capacity is slightly lower than that reported by Chihara et al.[67], which may be attributed to the synthesis procedure resulting in a different particle morphology or to the higher upper cutoff potential of 5.0 V used in their research as opposed to 4.5 V in the present study. In the 1M KPF$_6$/G2 electrolyte solution KVPO shows a dramatic parasitic oxidation current arising from the electrolyte degradation due to a larger population of free-solvent molecules at this concentration, which further explains the lowest discharge capacity values and low coulombic efficiencies (Figure 5.5). The other reason for the variation of the initial discharge capacity comes from the overpotential of the K metal anode.



Figure 5.5. Galvanostatic measurements of K$^+$-ion half-cells comprised of KVPO electrode and electrolytes of different concentrations, at a C/10 scan rate. a) Charge and discharge curves in the 10$^{th}$ cycle for each electrolyte concentration. b) Specific discharge capacity change upon cycling for different electrolyte concentrations. c) Coulombic efficiency changes upon cycling for different concentrations.

To estimate the resistance of the SEI layer leading to the large overpotential of K metal anode, the EIS measurements were performed in symmetric K cells in the potentiostatic mode. The PEIS spectra are analyzed using the proposed equivalent scheme (Figure 5.6c) in MEISP program. A large semicircle in the high-frequency region corresponds to the passivated film impedance on the potassium surface. Since a symmetric cell consists of two K|electrolyte interfaces, the interfacial resistances represent a doubling of a single K electrode. As no potential is applied upon measurements, only processes associated with the solid electrolyte interphase (SEI) formed on the K metal and the double layer charging are assumed to occur. Hence, SEI resistance and double layer capacitance are reflected by $R_{SEI}$ and $C_{dl}$, respectively. The Nyquist plot intercept with the horizontal axis in high-frequency region is attributed to the solution resistance value ($R_{sol}$). The area-specific solution resistance reduces with increasing concentration of $KPF_6$ (Table 5.2, Figure 5.6).

The evidenced tendency is ascribed to enhanced ion conductivity of the electrolyte, similar to that reported for the $NaPF_6$ in diglyme[155] and for $LiPF_6$ in carbonate-based solutions[156]. Moreover, the interfacial impedance corresponding to the area-specific SEI resistance shows a non-monotonic concentration dependence, being the highest for the 1M $KPF_6$/G2 solutions, reaching its minimum for the 2M $KPF_6$ solution and increasing again for the 2.5M $KPF_6$/G2 solution. This behavior probably originates from the thickness or composition variations of the SEI layer (Table 5.2, Figure 5.6).



Figure 5.6. a) Impedance spectra of the K symmetric cells with different electrolyte concentrations; b) the enlargement of the high-frequency range; c) the equivalent circuit scheme implemented for MEISP calculations.

Table 5.2. The solution area specific resistance $R_{sol}$ and solid electrolyte interphase area specific resistance $R_{SEI}$ values calculated using MEISP software in the K symmetric cells with different electrolyte concentrations.

| Electrolyte | $R_{sol}$, $\Omega*cm^2$ | $R_{SEI}$, $\Omega *cm^2$ |
|---|---|---|
| 1 M KPF$_6$ in G2 | 54.7±5.9 | 237.7±47.0 |
| 1.5 M KPF$_6$ in G2 | 37.9±6.5 | 65.2±16.6 |
| 2 M KPF$_6$ in G2 | 29.8±3.2 | 3.8±2.6 |
| 2.5 M KPF$_6$ in G2 | 27.6±3.3 | 9.9±3.1 |

The obtained $R_{SEI}$ – dependence versus salt concentration is in good correspondence with the initial discharge capacities of KVPO observed in KPF$_6$/G2 solutions. The presence of a resistive film induces a potential drop at the interface resulting in the reduced capacity values as described by modeling for Li-ion cells[16] and experimentally validated[157,158]. Consequently, the apparent initial specific discharge capacities for KVPO at different salt concentrations strongly depend on the interfacial resistance ($R_{SEI}$) on the K-metal anode, which was measured in the K symmetric cells (Table 5.2).

Moreover, the continuous capacity loss occurring in the (1M-2M) KPF$_6$/G2 electrolyte solutions is mainly due to the formation of an unstable SEI layer on the K metal surface in less concentrated electrolytes[14]. The SEI film growth observed in impedance spectra measured with time evolution (Figure 5.7) leads to higher $R_{SEI}$ values being responsible for the capacity fade on cycling.
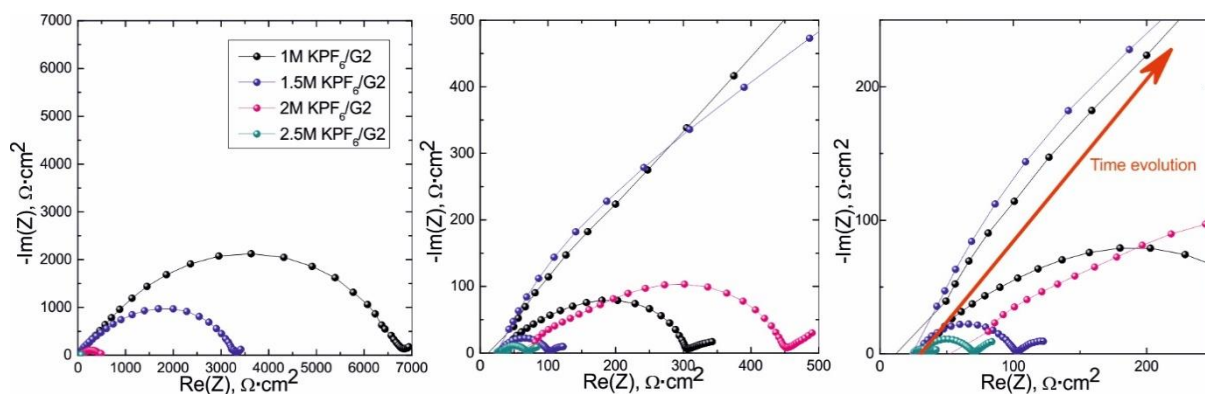


Figure 5.7. Impedance spectra of the K symmetric cells with different electrolyte concentrations showing the changes with time evolution at different scales.

Hence, the electrochemical performance of the K$^+$-ion cell constructed with an anode other than metallic K is expected to show a better performance. However, the capacity retention of 98% in the 2.5M KPF$_6$/G2 electrolyte solution indicates stable cycling where the capacity fade is not a result of the anode reactivity. Such electrochemical behavior for the cell with the highest electrolyte concentration is tentatively attributed to the minimum number of the free solvent

molecules leading to the lowest overpotential at the K metal due to a stable and thinner SEI film formed on the anode surface. The presence of irreversible redox processes in the 1M $KPF_6$/G2 electrolyte solution is evidenced by the coulombic efficiency (CE) vs. cycle number dependence (Figure 5.5c): the CE value does not exceed 50%, whereas the CE values for the 2M $KPF_6$/G2 and 2.5M $KPF_6$/G2 electrolyte solutions reach 86%. These results truly support the assumption that strongly coordinated solvent molecules are not preferentially reduced to form SEI layers, rather than the anions, which are predominantly reduced to form passivating and thicker SEI layers.

**KMFCN cathode performance in diglyme-based electrolyte**

To understand the influence of electrolyte solution structure on the different cathode material performance, KMFCN was cycled in a K half-cell using the whole set of electrolyte solutions at a 0.1C rate (14.8 mA·$g^{-1}$) in the 2.5-4.5 V vs. $K^+$/K potential range. According to the XRPD analysis, all electrodes after 30 cycles maintain the parent structure (Figure 5.8, Figure A2, Table A2).
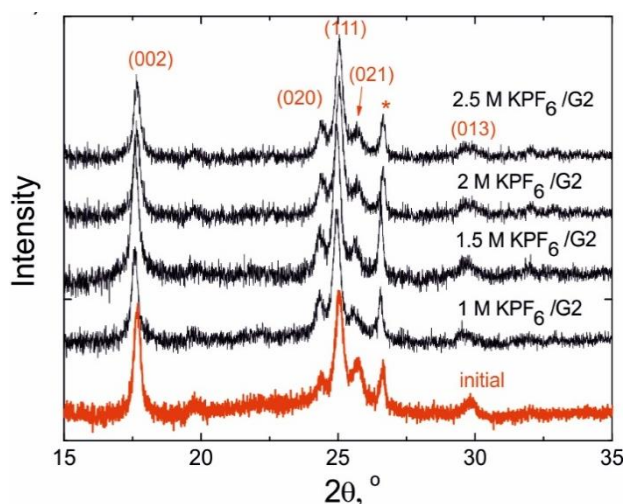


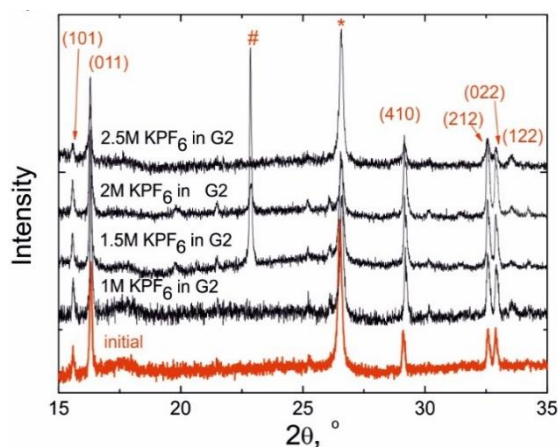Figure 5.8. XRPD patterns for $K_{1.44}Mn(Fe[CN]_6)_{0.9} \times 0.4H_2O$ pristine electrodes and electrodes on Al foil cycled upon 30 cycles in electrolytes with different salt concentrations (* - peaks correspond to conductive additive being present in the cathode composite)

Figure 5.9a demonstrates the charge/discharge profile of the 10th cycle for K half-cells having different electrolyte concentrations. The two plateaus on the discharge curve correspond to the $Fe^{3+}/Fe^{2+}$ (3.95 V vs $K^+$/K) and $Mn^{3+}/Mn^{2+}$ (4.05 V vs $K^+$/K) redox processes. The capacity loss in the K half-cells also occurs with the KMFCN working electrode (Figure 5.9b). In the highest concentration electrolyte solution, 2.5M $KPF_6$/G2 the capacity fade related to the KMFCN cathode contrasts with the stable cycling of the KVPO cathode, and could be tentatively ascribed to the manganese dissolution as reported for the $Li^+$-systems[159,160]. However, the capacity retention increases to 68% for the higher electrolyte concentrations compared to 30% for 1M $KPF_6$/G2, which is attributed to a smaller amount of free solvent molecules at the higher electrolyte salt

concentrations resulting in a thinner surface passivation layers and enhanced electrolyte stability against other redox processes occurring at the electrode surfaces upon cycling. This behavior is expected because the oxidation stability of the solvent molecules solvating metal ions enhances compared to the oxidation potential of the free solvent molecules[161]. The highest specific discharge capacity for the first cycle is 105 mAh·g$^{-1}$ in the 2.5M KPF$_6$/G2 electrolyte, which is lower than a previously reported value of 141 mAh·g$^{-1}$ [44]. The difference in reversible capacity is tentatively explained by the different water content and K:Fe ratio of the K$_x$Mn[Fe(CN)$_6$]$_y$×nH$_2$O materials synthesized for the two studies: K$_{1.75}$Mn[Fe(CN)$_6$]$_{0.93}$×0.16H$_2$O in [44] and K$_{1.44}$Mn[Fe(CN)$_6$]$_{0.9}$×0.4H$_2$O in our study. The coulombic efficiency exceeds 78% upon 30 cycles (Figure 5.9c).
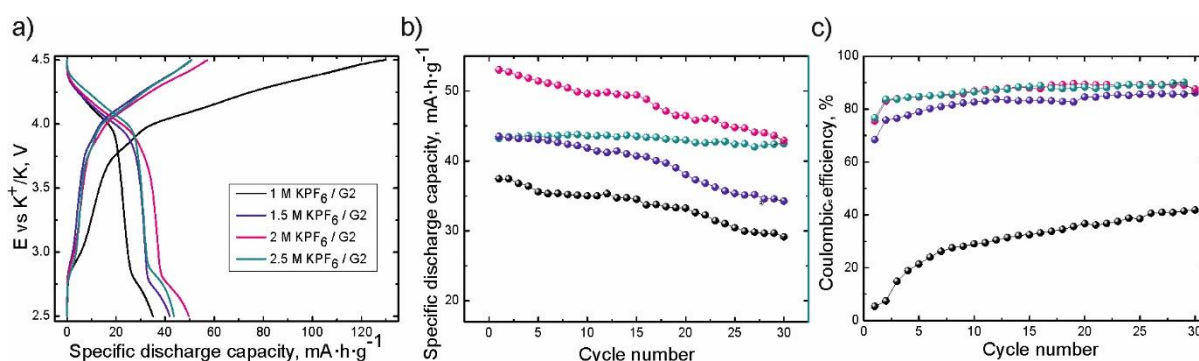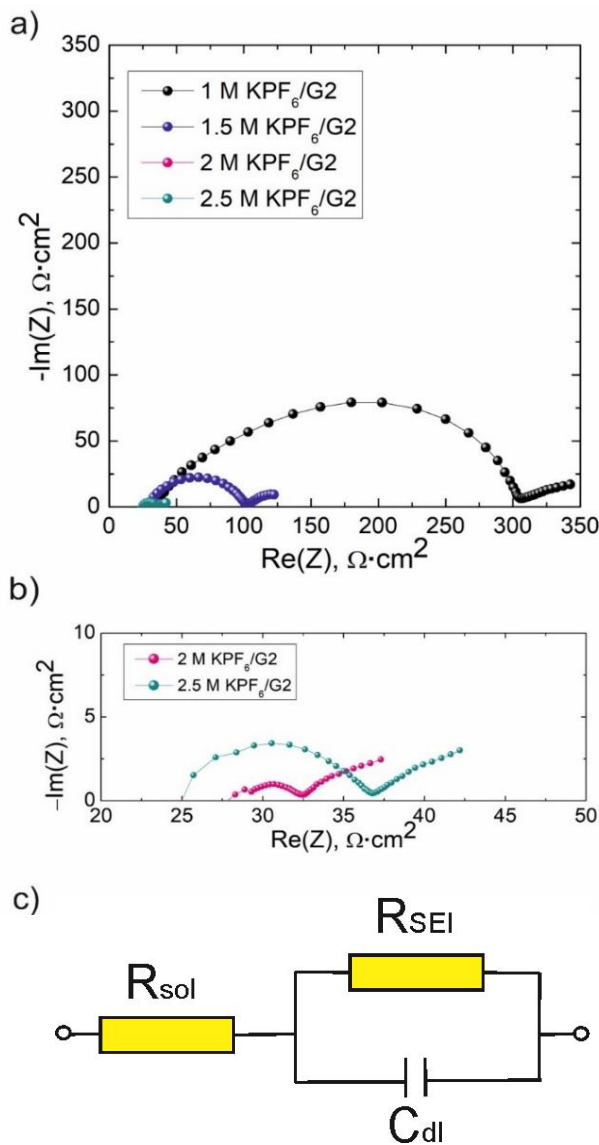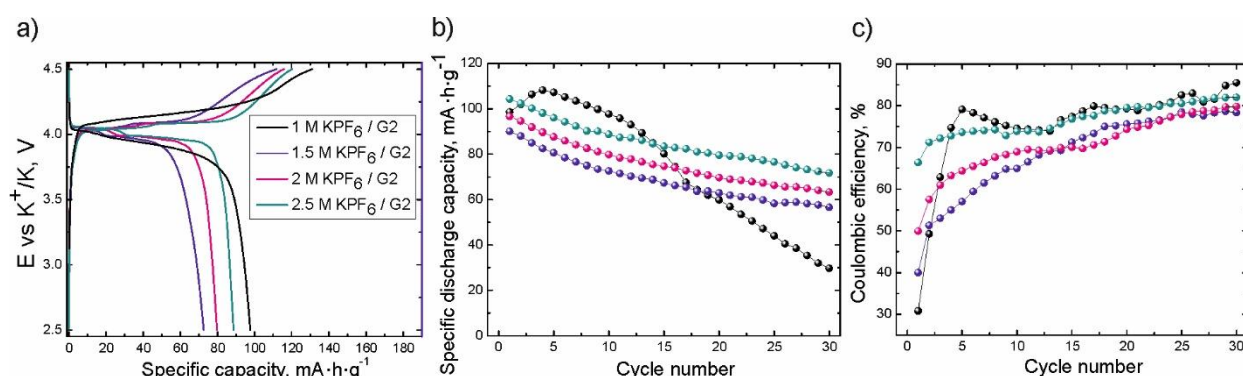


Figure 5.9. Galvanostatic measurements of K$^+$-ion half-cells comprised of KMFCN cathodes and electrolytes of different concentrations at a 0.1C rate. a) Charge and disc      harge curves of the tenth cycle for each electrolyte solution. b) Specific discharge capacity vs. cycle number for different electrolyte concentrations. c) Coulombic efficiency vs. cycling for different electrolyte concentrations.

**HC anode performance in diglyme-based electrolyte**

Finally, two-electrode K$^+$-ion half-cells with HC working electrodes and various electrolytes were assembled and cycled at 0.1C rate (30 mA·g$^{-1}$) in the 0.1-2.5 V vs. K$^+$/K potential range for 30 cycles. The discharge/charge curve profiles do not vary with the electrolyte salt concentration (Figure 5.10a). The initial capacity value of the hard carbon (HC) anode in K$^+$-ion half-cells is shown in the Figure 5.10b. The pronounced increase in cathode specific discharge capacity with electrolyte concentration is not observed for the anode in the present electrolyte solutions, indicating a minor electrolyte concentration effect on the HC surface chemistry during cycling. Coulombic efficiency is higher in more concentrated electrolyte solutions at the first cycle(Figure 5.10c) that can be associated with the anion-derived SEI layer formation enabling the effective HC protection, as was detected in Na-ion cells[131]. However, the presented results could also be

tentatively attributed to the irreversible $K^+$-ion insertion into the HC structure. Nonetheless, several additional studies of this issue are required.

In summary, a pronounced effect of the electrolyte salt concentration on the cathode specific discharge capacity has been observed. An increase in the discharge capacity with the electrolyte salt concentration is accounted for the smaller free solvent molecule number, providing enhanced electrolyte stability against other limiting redox processes (e.g. Al electrode passivation and solvent oxidation processes). As the HC anodes were shown to be not affected by the electrolyte salt concentration, the low coulombic efficiency values in the first cycle can be accounted for the irreversible $K^+$ ion intercalation into the HC framework which requires further elucidation as to anode-dependent processes.
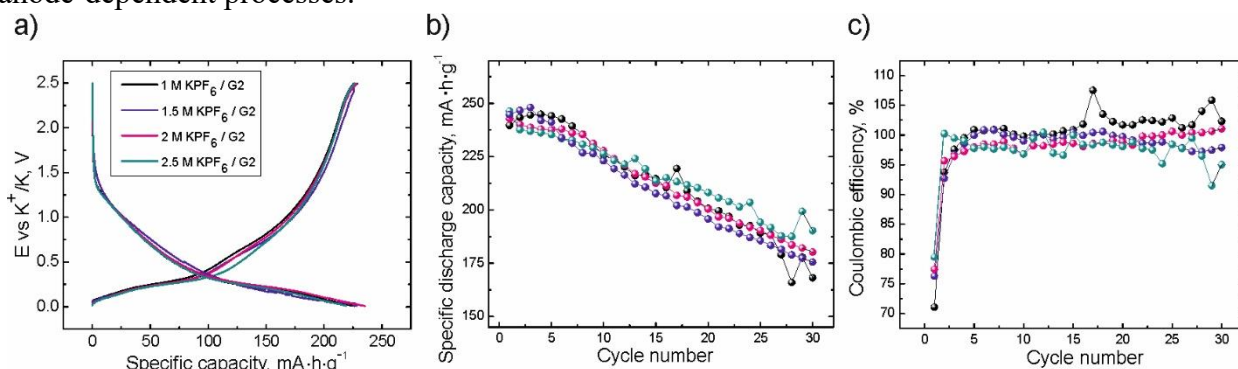


Figure 5.10. Galvanostatic measurements of $K^+$-ion half-cells with an HC electrode at a 0.1C scan rate. a) Charge and discharge curves in the 10th cycle for each electrolyte concentration. b) Specific discharge capacity changes upon cycling for different electrolyte concentrations. c) Coulombic efficiency changes upon cycling for different electrolyte concentrations.

**K full cell**

To demonstrate the practical significance of the obtained results, a comparative investigation of full cells consisting of KMFCN cathode and HC anode was performed using both the ether-based and conventional carbonate-based electrolytes with anode-to-cathode capacity ratio of ~3 to prevent the effect of the irreversible anode capacity change on the full battery performance. In the carbonate electrolyte, the optimal amount of the $KPF_6$ salt added to the EC:DEC (1:1, v:v) solvent mixture while remaining a transparent solution was 0.5M (at electrolyte concentrations higher than 0.5 M the $KPF_6$ salt readily deposits on the separator, electrode surface and cell components). As the K full cell cycling was performed to prove the feasibility of $K^+$-ion battery implementation at the 0.6C rate (90 mA·g$^{-1}$), which is considerably higher than the 0.1C rate used for the galvanostatic measurements in the K half-cells, the electrolyte salt concentration effect on the (de)insertion rate becomes important. Since the enhanced salt concentration could result in the reduced intercalation rate and, hence, the cell electrochemical performance declines at the practically important discharge current rates which are predominantly higher than 0.1C[162]. Here,

the 1.5M KPF$_6$/G2 electrolyte solution was chosen to overcome possible kinetic hindrances at the higher current rate (however, the full cell using the 2.5 M KPF$_6$/G2 electrolyte solution with the highest concentration was cycled and compared to the full cell using the carbonate-based electrolytes in Figure 5.12). Although the initial cell capacity was higher for the carbonate-based electrolyte (121 mAh·g$^{-1}$ of cathode) than for the ether-based electrolyte (105 mAh·g$^{-1}$ of cathode), capacity retention is better for the latter one (Figure 5.11a). The capacity retention of 86 % after 300 cycles at 0.6C rate with a specific capacity value of 90 mAh·g$^{-1}$ of cathode was observed for the 1.5M KPF$_6$/G2 electrolyte, whereas the carbonate-based electrolyte demonstrated only 66% capacity retention after 300 cycles at the 0.6C rate, as well as a lower specific capacity value of 80 mAh·g$^{-1}$ of cathode (Figure 5.11a). Moreover, in 1.5M KPF$_6$/G2 the specific discharge capacity stabilizes after 125 cycles, whereas it keeps decreasing in the 0.5M KPF$_6$/EC:DEC solution. However, the CE vs. cycling curves are quite similar (Figure 5.11b). The charge and discharge curves at the last cycle are also presented for both electrolyte solutions (Figure 5.11c). The full cell with the HC anode exhibits better specific discharge capacity and capacity retention than the full cells comprised of the Prussian Blue analogue cathode, carbonate-based electrolyte, and non-HC carbonaceous anodes[44,53]. Moreover, the attained electrochemical characteristics exceed those reported for K full cells consisting of the Prussian Blue analogue cathode and ether-based electrolyte, in which the specific discharge capacity is below 90 mAh·g$^{-1}$ of cathode[57,85,163]. The applied strategy to tune salt concentration in ether-based electrolyte solutions was also reported to attain the enhanced cycle stability of K full cell comprising graphite anode and K$_2$Mn[Fe(CN)$_6$] cathode[87]. The utilization of highly concentrated [5.6 mol·kg$^{-1}$ KFSI/G3+0.5wt%VC] leads to the discharge capacity of 106 mAh·g$^{-1}$ of cathode after 100 cycles. Furthermore, the observed findings are in line with other studies on electrolyte composition optimization that enhances the stable cycling of K full cell delivering the initial discharge capacity value of 105 mAh·g$^{-1}$ of cathode[78,164]. Hence, the present results demonstrate improved K full cell performance when using the diglyme-based electrolytes with the proper concentration of the KPF$_6$ salt and a hard carbon anode. Highly concentrated electrolyte solutions may be a useful instrument for further K$^+$-ion battery development.
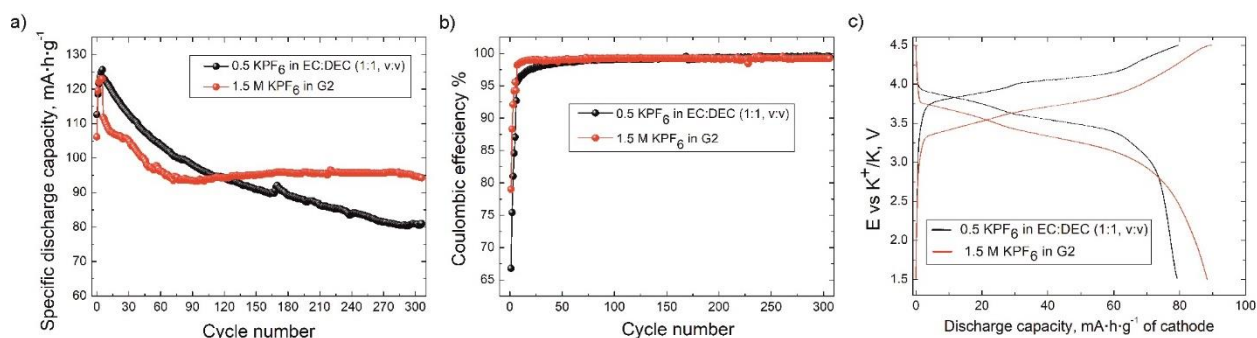
Figure 5.11. Comparison of galvanostatic measurements of K full cells comprised of KMFCN cathode and HC anode with carbonate-based and ether-based electrolytes. a) Variation in the specific discharge capacity with cycle number, b) Dependence of the coulombic efficiency on the cycle number, and c) Charge and discharge curves at the 300$^{th}$ cycle. The current density equals 0.1C during first five cycles, the further cycling was performed at 0.6C current density
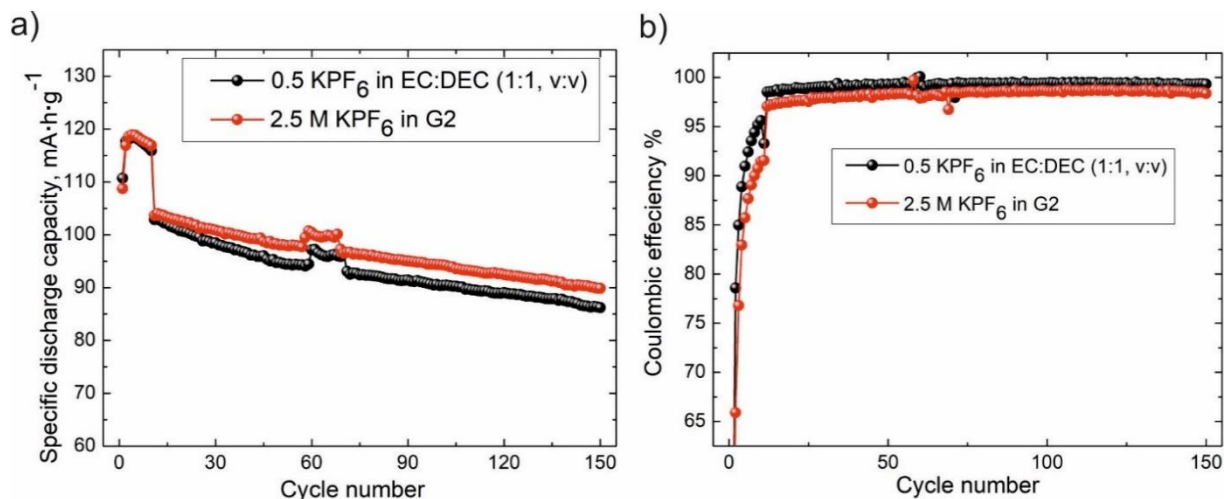


Figure 5.12. Comparison of galvanostatic measurements of K full cells comprised of KMFCN cathode and HC anode with carbonate-based and ether-based electrolytes. a) Variation in the specific discharge capacity with the cycle number; b) Dependence of the Coulombic efficiency on the cycle number.

**Conclusion**

The impact of the salt concentration on the performance of KVOPO$_4$ and K$_{1.44}$Mn(Fe[CN]$_6$)$_{0.9}$×0.4H$_2$O cathodes and hard-carbon anode is clearly shown. An increase of the KPF$_6$ salt concentration results in a reduced number of free diglyme molecules. Hence, all redox processes associated with solvent molecule's oxidation are minimized, explaining the enhanced electrochemical performance of KVOPO$_4$ and K$_{1.44}$Mn(Fe[CN]$_6$)$_{0.9}$×0.4H$_2$O positive electrodes in the K half-cells. The maximum specific discharge capacities of the KVOPO$_4$ and K$_{1.44}$Mn(Fe[CN]$_6$)$_{0.9}$×0.4H$_2$O cathodes are attained in the diglyme-based electrolytes with the highest KPF$_6$ concentrations of 2 and 2.5 M, respectively. Furthermore, a full cell based on K$_{1.44}$Mn(Fe[CN]$_6$)$_{0.9}$×0.4H$_2$O and HC exhibits stable discharge capacity of ∼90 mA·h·g$^{-1}$ after 125 cycles. However, the specific reasons for the observed HC behavior in the concentrated electrolytes should be clarified in the future research. Albeit, the similar performance of HC electrode in all [x M KPF$_6$/G2] solutions, the outstanding performance of full K cell with HC negative electrode is attained in more concentrated electrolyte compositions.

**Chapter 6. Electrolyte salt concentration effect on the SEI layer evolution on HC surface.**

No significant difference was observed for K half cells comprising HC negative electrode and diglyme-based electrolyte with various $KPF_6$ salt contents in Chapter 5. However, the full cell demonstrated the improved performance with pre-loaded HC electrodes in electrolytes with enhanced concentrations that could arise from the anion-derived solid electrolyte interphase (SEI) layers[131]. After cycling in diglyme-based electrolyte solutions, the electrodes are retrieved from the K half cells after discharge step and washed in G2 during a couple of hours to remove traces of $KPF_6$ from the HC surface. Then dried electrodes were located into the special vacuum vessel to transfer inside XPS chamber without surface exposure to air. The collected XPS spectra were measured using a 200 µm X-ray beam size to gain more statistics. The pristine HC electrode contains C (83.4 at.%), O (15.3 at.%) and Na (1.3 at.%) atoms. The presence of Na arises from the addition of Na-CMC binder to the negative electrode composite. The contribution of Na-CMC binder and conductive additive surfaces to the obtained XPS signal is not accounted for in the present research. We strived to overcome it via probing several spots from the retrieved electrodes and analyzing the average output data.

Figure 6.1a illustrates the observed C1s XPS spectra for the retrieved HC composite electrodes cycled in K half cells with the concentrated electrolyte solution [2.5M $KPF_6$ /G2]. The four detected peaks are associated with O-C=O (~289.8 eV), C-O (~287.9 eV), C-C/C-H (~286.4 eV) and $K_x$-HC (~284.9 eV) bonds respectively. The peak located at ~284.9 eV at C1s spectra is assigned to the potassiated HC ($K_x$-HC). Eshetu et al.[165] claimed that this peak reflects the thickness of the SEI layer. However, from the present data, it's complicated to identify whether the SEI thickness changes during cycling since the peak intensity depends both on the component content and its allocation in the surface film versus $z$-axis. The SEI thickness will be determined from the further results of HAADF-STEM measurements. Figure 6.1b reveals the presence of two peaks in the F1s XP spectra which are associated with the K-F (~684.6 eV) and $K_xPO_yF_z$ (~689.4 eV) bonding.
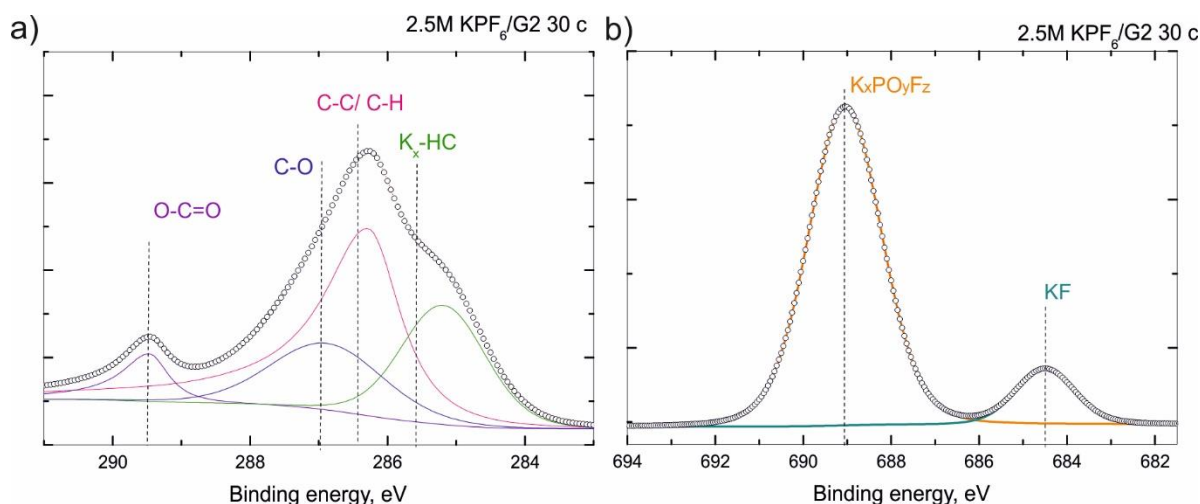
Figure 6.1. Deconvolution of peaks at C1s (a) and F1s (b) XPS spectra of HC composite electrodes retrieved after 30 full charge/discharge cycles from K half cell with 2.5 M KPF$_6$/G2 electrolyte solution.

Figure 6.2 depicts the XPS spectra changes versus the KPF$_6$ salt concentration increase in electrolyte solutions. The distinguishable difference concerns the intensity of peak associated with K$_x$PO$_y$F$_z$ (~689.4 eV) bonding: the peak intensity is significantly declined in the SEI formed in dilute diglyme-based electrolyte (Figure 6.2b). It should be noted that both KF and K$_2$CO$_3$ might destroy the transport properties of formed surface layers as it was published recently[166], though LiF and NaF are reported to improve the transport properties of SEI film in Li$^+$- and Na$^+$-systems[167].
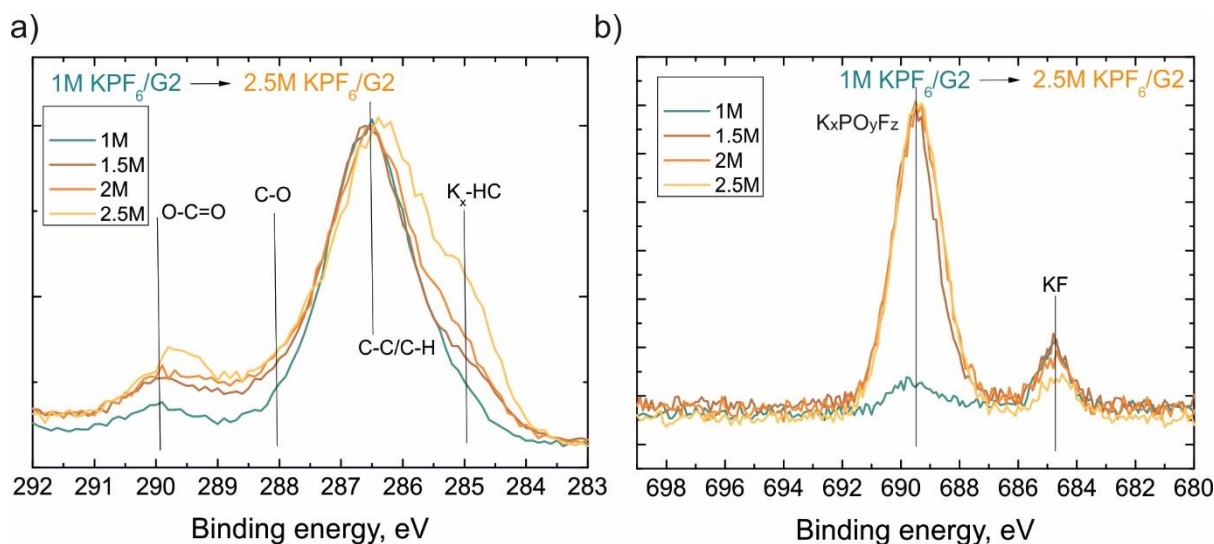


Figure 6. 2. (a) C1s and (b) F1s XPS spectra of HC composite electrodes retrieved after 30 full charge/discharge cycles from K half cell with 1M; 1.5M; 2M and 2.5 M KPF$_6$/G2 electrolyte solutions

The HAADF-STEM characterization coupled with STEM-EDX mapping of 30 times cycled HC electrode surface reveals the absence of thick SEI formation (Figure 6.3). Either the modified

upper layer of HC particle or the formation of thin SEI film with the thickness of less than 15 nm is evident after cycling in K cell with [2.5 M KPF$_6$ / G2] electrolyte solution. This modified layer or SEI film contains C, O, F and K elements that coincide with the XPS measurements.
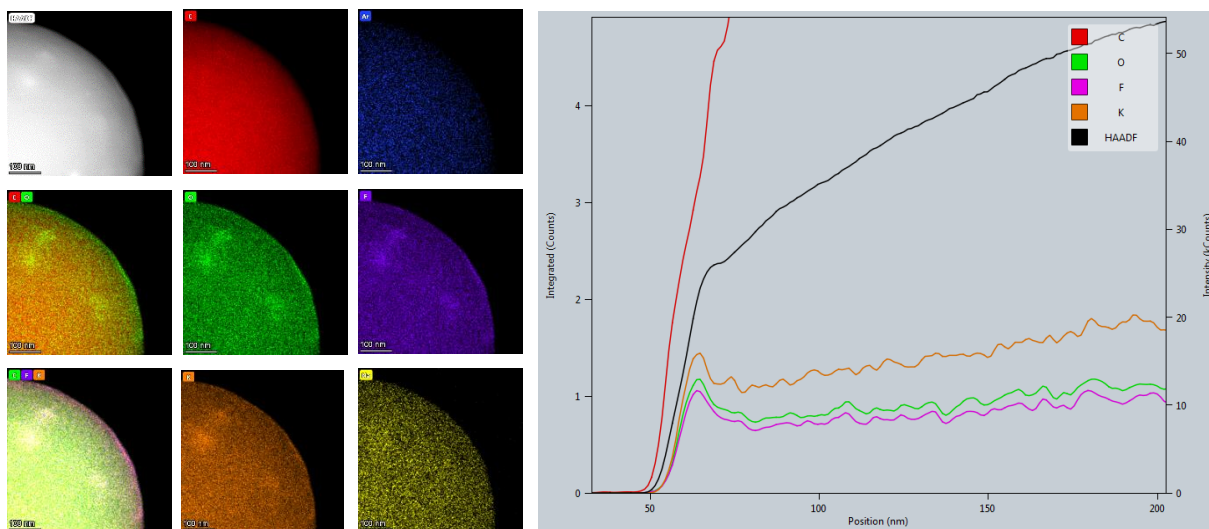


Figure 6.3. TEM characterization of the HC surface after 30 charge/discharge cycles in the (2.5M KPF6 in G2) electrolyte: (a) HAADF-STEM image, individual elemental STEM-EDX maps, and mixed color-coded EDX maps. (b) EDX signal intensity profiles across the surface of the HC particle.

**Chapter 7. Electrolyte additive effect on SEI formation on HC surface in K$^+$-ion batteries**

Herein, we probe vinylene carbonate (VC) as an electrolyte additive for PIBs batteries due to its ability to form the uniform and flexible SEI on anodes[168,169]. The positive impact of vinylene carbonate (VC) on carbonaceous anode materials in Li-ion batteries in terms of decreasing irreversible capacity and improving cycling stability was demonstrated in a number of literature reports[170–172]. VC is believed to decompose before the SEI formation thus suppressing the two-electron reduction of ethylene carbonate (EC). Hereinafter, we intend to investigate the SEI layer properties via a strategy of VC addition to the carbonate-based electrolyte. The electrochemical study of the HC electrode performance in the electrolyte with and without VC in PIBs is complemented by probing the morphology and composition of the SEI films to comprehend an electrolyte additive effect on the SEI formation and stability evolution upon cycling.

**Electrochemical measurements**

The electrolyte solutions with different VC (1, 2 and 4 wt. %) and FEC (5 wt.%, 50 wt.%) concentrations are probed electrochemically. Since FEC is usually added in a larger amount because it does not destroy metal-ion battery cell kinetics, while VC is added in minimal concentrations to improve SEI elasticity without a loss of its transport properties[173]. The cyclic voltammetry (CV) curves were registered at a scan rate of 100 µV·s$^{-1}$ in K half cells with hard carbon electrode utilizing different electrolyte solutions (Figure 7.1): 0.5M KPF$_6$/EC:DEC (1:1, v:v); 0.5M KPF$_6$/EC:DEC (1:1, v:v) +1 wt.% VC; KPF$_6$/EC:DEC (1:1, v:v) +5 wt.% FEC and KPF$_6$/EC:DEC (1:1, v:v) +50 wt.% FEC. The reduction current corresponding to the electrolyte component decomposition occurs at 1.7 V vs K$^+$/K at the forward scan in bare carbonate-based electrolyte (Figure 7.1a). Whereas, in electrolyte with VC (Figure 7.1b), the VC reduction with the subsequent electrolyte decomposition starts at the lower potential – ~1.45 V vs K$^+$/K. The K half cells with the HC electrodes and FEC as the electrolyte additive exhibit poor electrochemical behavior (Figure 7.1c,d) indicating enormous electrolyte degradation. Moreover, as no anodic peak is evidenced at forward CV scans for both FEC concentrations, we suggest the formation of insulating surface layers blocking K$^+$-ion diffusion through the electrode/electrolyte interface. The larger FEC concentration tunes only peak current whereas the additive reduction process is anyway preferential in the potential range than the other electrolyte component decomposition[6]. Thereby, the FEC additive was excluded from further consideration due to its clear negative effect in PIBs.
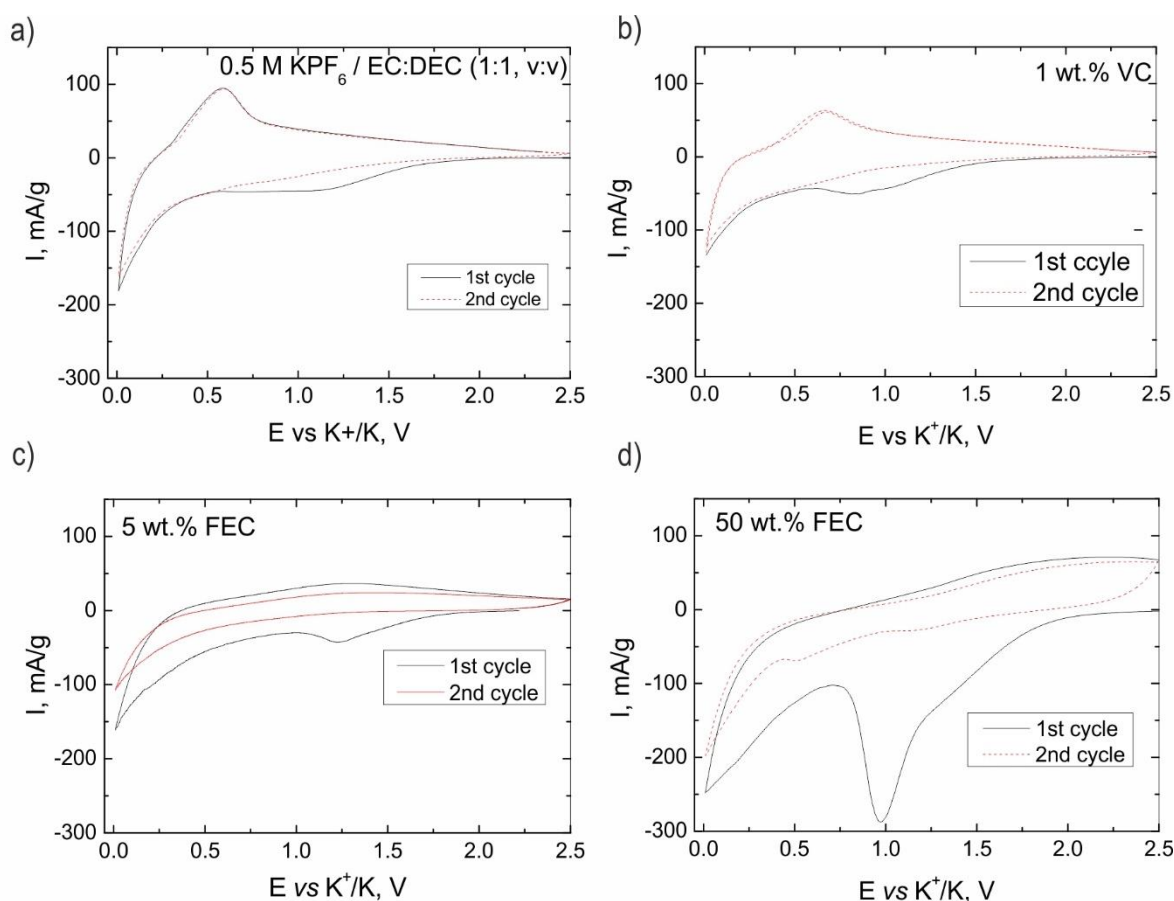
Figure 7.1. Normalized cyclic voltammetry curves measured with a scan rate of 100 $\mu V \cdot s^{-1}$ for the first two cycles in K half cells with hard carbon electrode in the potential range 0.010 – 2.5 V vs $K^+/K$ in (a) 0.5M $KPF_6$/EC:DEC (1:1, v:v), (b) 0.5M $KPF_6$/EC:DEC (1:1, v:v) +1 wt.% VC, and (c) $KPF_6$/EC:DEC (1:1, v:v) +5 wt.% FEC and (d) $KPF_6$/EC:DEC (1:1, v:v) +50 wt.% FEC electrolyte solutions. The black solid line shows the first cycle and the red dash line – the second cycle.

The electrochemical data of the HC electrodes cycled in K half cells with pristine and VC-containing carbonate-based electrolytes are reported in Figure 7.2. The HC electrodes were further retrieved after 30 full charge/discharge cycles to investigate the SEI layers with electron microscopy tools. The difference of CV curve shapes (Figure 7.2a) between first two charge scans can tentatively be ascribed to differences in polarization of K metal. On the first charge the irreversible capacity loss (ICL) mainly arises from the SEI formation but it also may originate from the formation of soluble reduction products[6] or from trapping of $K^+$ inside the HC structure as it was suggested in Chapter 5 and reported for the Li-ion systems[6]. In Figure 7.2a the ICL values on the first cycle vary in the range of 35 - 40% of the total charge capacity, with slightly smaller ICL value in the pristine carbonate-based electrolyte compared to the VC-containing solutions. However, in the pristine carbonate-based electrolyte the ICL occurs during whole 30

96

charge/discharge cycles (Figure 7.2c) denoting continuous parasitic reactions. CE value achieves >99% in the 0.5M $KPF_6$/EC:DEC (1:1, v:v) +4 wt.% VC electrolyte already at the third cycle (Figure 7.2c). Other K half cells with the electrolyte with smaller VC concentrations also exhibit the reduced ICL value and the CE value >98% after 4-13 cycles depending on the VC concentration. The initial discharge capacity decreases with enhancing the VC content (Figure 7.2b) that coincides with the earlier published data[172]. The observed variation of capacity values could originate from the reactive K metal which is used as a counter electrode in K half cells[85,174]. The same trends are preserved in Figure 7.3 illustrating the distribution of electrochemical data collected from three K-half cells for each electrolyte composition.
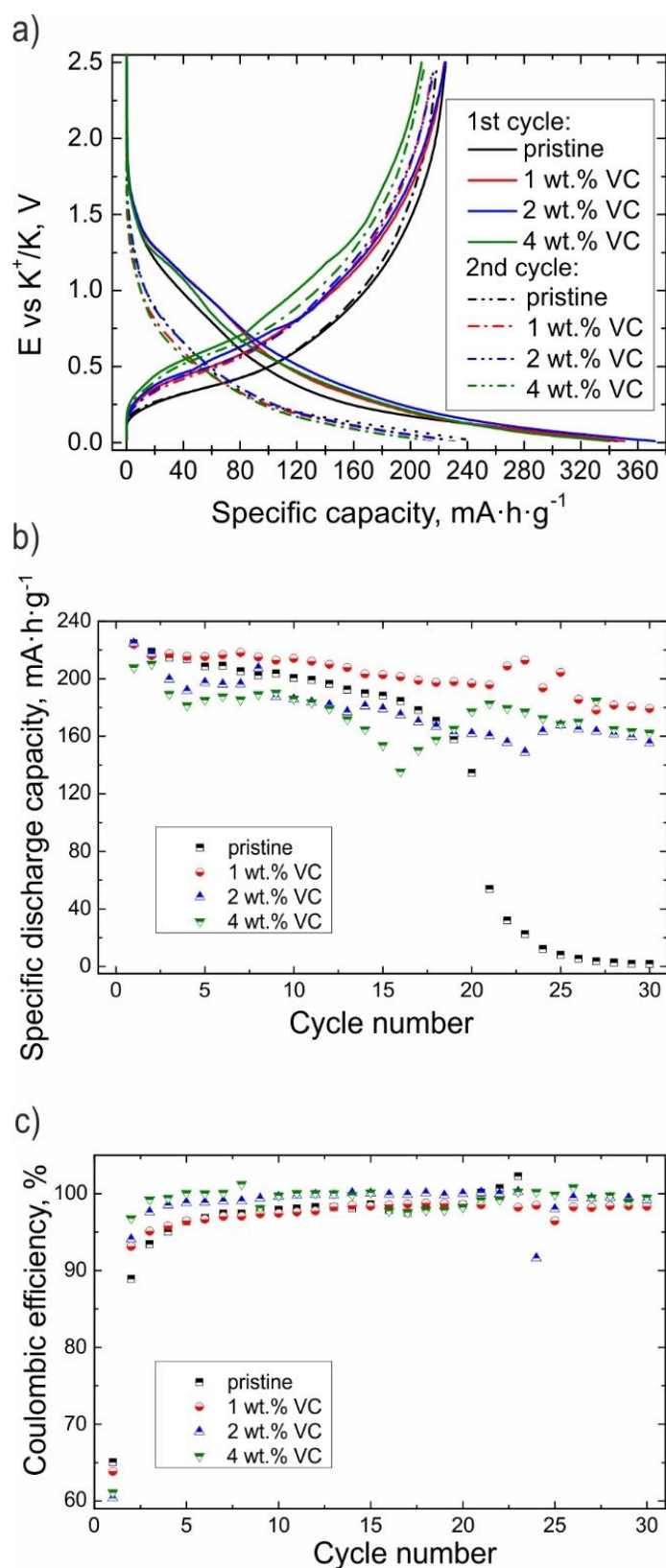
Figure 7.2. Galvanostatic measurements in the K-half cells with the HC electrode and carbonate-based electrolyte without and with VC additive in different concentrations: a) galvanostatic curves of two first cycles measured in the potential range of 0.010 – 2.5 V vs K$^+$/K (the solid and dashed lines correspond to the first and second cycle, respectively); the dependences of the specific discharge capacity (b) and Coulombic efficiency (c) on the cycle number.

To distinguish the potential ranges, in which the $K^+$ intercalation, electrolyte decomposition and VC reduction intervene, the differential capacity (DC) plots are analyzed. In our experiments the enhanced reduction current corresponding to $K^+$ intercalation and the SEI formation is observed at the range of ~0.01-0.5 V vs $K^+/K$ respectively on the DC plots for all electrolyte compositions (Figure 7.4). Addition of VC results in emergence of the extra peak at ~1.25 V vs $K^+/K$ which corresponds to VC reduction preceding the decomposition of other electrolyte components. It confirms the role of VC as an electrolyte additive in PIBs due to the polymerization reaction of open VC or EC radical anions with the VC molecules that is thermodynamically more favorable than reacting with the EC molecules[175].
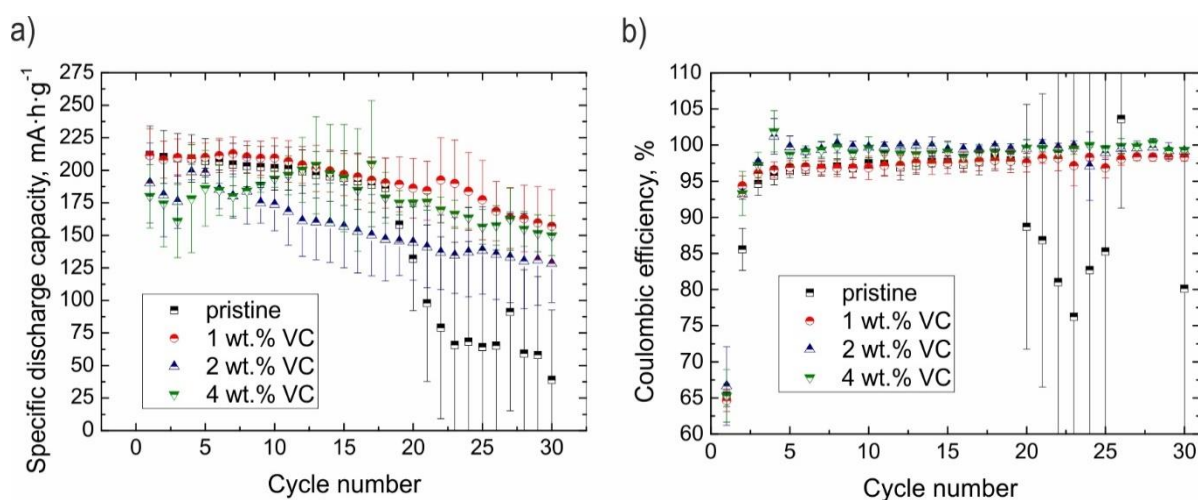


Figure 7.3. The average distribution of the dependences of the specific discharge capacity (a) and Coulombic efficiency (b) versus cycle number with error bars provided for three K-half cells with the HC electrode and carbonate-based electrolyte without and with VC additive in different concentrations: detected in the potential range of 0.010 – 2.5 V vs $K^+/K$.

It is difficult to determine the voltage at which the SEI is formed on the HC electrode from the presented galvanostatic measurements. Generally, it depends on the electrolyte composition, the experimental conditions (for instance, current density and temperature) and the catalytic properties of HC surface. In the case of the carbonaceous anode in Li-ion systems, the potential of the SEI formation is published to be lower than 1 V vs $Li^+/Li$[176,177]. However, our *in situ* AFM measurements demonstrate that the SEI formation starts at 1.0-1.5 V vs $K^+/K$ for solutions with
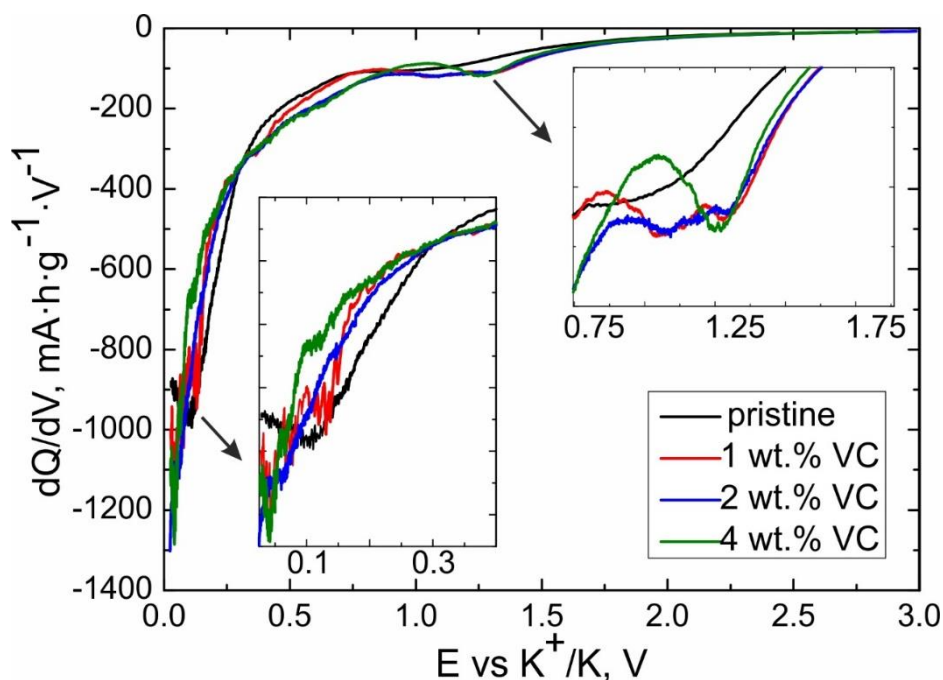
Figure 7.4. Differential capacity plots measured for the first cathodic scan in K half cells with HC electrode in the potential range 0.010 – 2.5 V vs K$^+$/K in all set of electrolyte solutions: 0.5 KPF$_6$/EC:DEC(1:1, v:v); 0.5M KPF$_6$/EC:DEC (1:1, v:v) +1 wt.% VC; 0.5M KPF$_6$/EC:DEC (1:1, v:v) +2 wt.% VC and 0.5M KPF$_6$/EC:DEC (1:1, v:v) +4 wt.% VC

**Evolution of SEI layer formation by in situ AFM measurements**

*In situ* AFM measurements are performed inside an Ar-filled glove box on cross-sections of a fresh HC electrode embedded in epoxy resin. A piece of K foil is used as a reference and a counter electrode, respectively. The K foil is gently scratched by a stainless tweezer in order to expose fresh shiny surface and quickly placed in an AFM cell which was filled with the electrolyte. After that, the open-circuit voltage (OCV) drop from 3 V to 2.0-2.5 V is achieved and stabilized. Without these steps intensive bubble formation is observed and the bubbles floating and stacking around the cantilever (figure 7.5) terminated AFM measurements by interfering with the detection laser.
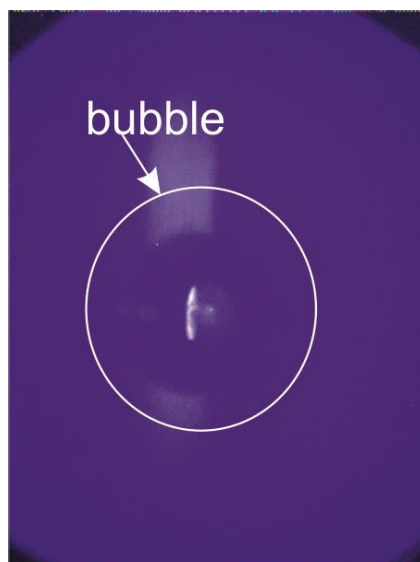
Figure 7.5. Optical image of a bubble that cut the detection laser beam above the AFM cantilever.

Figure 7.7 illustrates CV curves recorded at 1 mV·s$^{-1}$ scan rate and corresponding *in situ* AFM topography images of the HC surface. The registered shape of the CV curve differs from the conventional duck-shape CV curves obtained in the K half cells (Figure 7.1a,b). One possible reason is that the electrode area implemented in the AFM setup is about $7.1 \cdot 10^{-8}$ m$^2$ (Figure 7.6) that is 10000 times smaller than the macroelectrode area and only 100 times larger than the area of an ultramicroelectrode (generally, an electrode with a radius of less than 25 μm[9]), those utilization results in vanishing the duck-shape peak at CV curve under slow scan rates[9,178].



Figure 7.6. The optical image of HC electrode part embedded in epoxy resin for AFM measurements illustrating the geometric size of the anode.
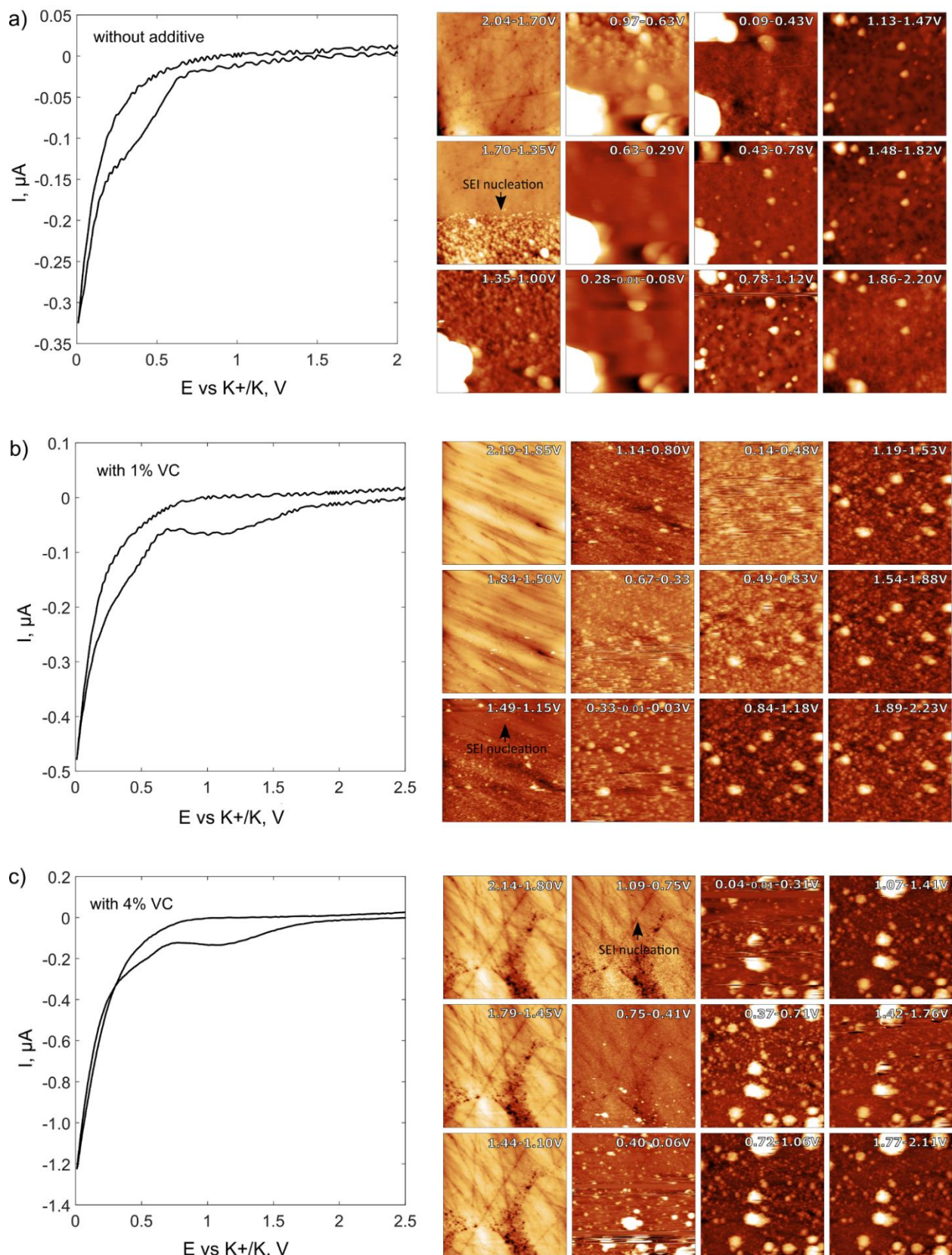
Figure 7.7. CV curves and corresponding in situ AFM topography images of HC surface in (a) 0.5M KPF$_6$/EC:DEC (1:1, v:v) "pristine" without additive, (b) 0.5M KPF$_6$/EC:DEC (1:1, v:v) +1 wt.% VC, and (c) KPF$_6$/EC:DEC (1:1, v:v) +4 wt.% VC electrolyte solutions. Scan size is 4×4 μm. The slow scan direction is from top to bottom. The numbers at the top right corner of each in-

situ scan is a voltage range of the image acquisition: the left number – the image top, the right number – the image bottom. The arrows indicate SEI nucleation.

In the pristine 0.5M KPF$_6$/EC:DEC (1:1, v:v) electrolyte solution SEI nucleation is detected at about 1.5V as appearance of a stable surface deposit (Figure 7.7a). The small reduction current associated with the electrolyte component decomposition is poorly distinguishable at the CV curve due to the current oscillations, but is observed in the K half cells (Figure 7.1a). At about 1.4V the surface is completely covered by porous SEI. Upon further SEI growth large particles on surface are typically observed, which contaminate the cantilever and affect detailed imaging of the SEI evolution. The particles disappear in the anodic cycle at about 1 V, and dense uniform SEI layer is formed with separate particles protruding above the SEI which are tentatively ascribed to the bottom inorganic SEI film. The SEI formed on HC in Li-ion batteries is mainly composed of electrolyte salt reduction products[6]. We suppose the SEI layer formation accompanied by electrolyte component decomposition continues at the subsequent charge/discharge cycles leading to the thick loose and mushy SEI film observed via SEM measurements below.

In the 0.5M KPF$_6$/EC:DEC (1:1, v:v) +1 wt.% VC electrolyte solution SEI nucleation is detected at about 1.4V and complete surface coverage is achieved at 1.1V (Figure 7.7b). At this stage the SEI surface is mostly composed of particles less than 50 nm in diameter with inclusions of particles of ~200 nm in size (see Figure 7.8). As the anodic current corresponding to the VC reduction occurs at 1.65 V vs K$^+$/K, we inferred the VC reduction products do not precipitate on the HC surface themselves. However, their reaction with the electrolyte shifts the SEI nucleation to lower potential than in a pristine carbonate-based electrolyte and changes the SEI composition. During further cycling the particle's size increased to ~100 nm and ~500 nm, respectively, and at about 0.1 V in the anodic cycle the SEI stabilized. The final SEI surface structure is similar to the one formed in the pristine electrolyte, but with slightly higher roughness (the root mean square average of profile height deviations from the mean line, Rms, 30 nm vs 18 nm). The larger particles appear to be agglomerates of smaller 50-100 nm particles.
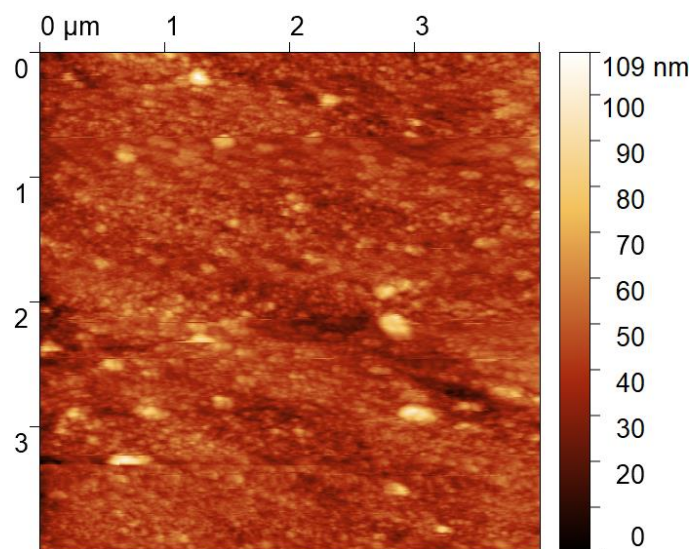
Figure 7.8. The in situ AFM topography image of HC surface in the 0.5M $KPF_6$/EC:DEC (1:1, v:v) +1 wt.% VC electrolyte solution illustrating particles less than 50 nm in diameter with inclusions of particles of ~200 nm in size

In the 0.5M $KPF_6$/EC:DEC (1:1, v:v) +4 wt.% VC electrolyte solution the SEI nucleation is detected at ~0.9 V and complete uniform surface coverage is achieved at ~0.8V (Figure 7.7c). Thus, the enhanced VC addition further decreased the SEI nucleation potential. The SEI thickness further grows (traces of scratches disappeared) and at 0.5V new 100-200 nm agglomerates of particles appear. The SEI topography is stabilized around 0.3 V in the anodic cycle with up to 1 μm agglomerations of 50-200 nm particles, which remain stable till the end of cycling. Note that for all samples before SEI nucleation a viscous surface layer is detected by cantilever's vibration amplitude damping.

The CV curves measured during the AFM measurements possess oscillations. The oscillation amplitude decreases with increase of the VC content in the electrolyte (Figure 7.7). The observed periodical electrochemical oscillations are tentatively associated with the bubble generation from the electrode surface. Bubbles are observed during *in situ* AFM in an optical microscope (Figure 7.5). It is worth to mention that electrochemical oscillations could arise from three processes occurring at the electrode surface including 1) the periodic precipitation and dissolution of products, 2) cyclical changes of intermediate valence ions, and 3) bubble generation[179].

The mentioned above intensive gas formation in the pristine electrolyte solution indicates the continuous solvent decomposition in the course of cycling. The suggested gaseous products are believed to be $C_2H_4$, $H_2$, $CO_2$, $CH_4$ as it was published for the carbonate-based solution decay (EC, DEC) evidenced in Li- and Na-ion batteries[180]. However, the VC addition prevents electrolyte decomposition as gas emission is dumped in the [0.5M $KPF_6$ in EC:DEC + 4% wt.VC] electrolyte.

It agrees well with the published data about positive effect of VC on suppression of gas emission[168]. Hereinafter, the additive could preclude the formation of large amount of gases which is vital for the further PIB commercialization.

**Morphology and chemical composition of the cycled HC electrodes**

After cycling in different electrolyte solutions, the electrodes are retrieved from the K half cells after discharge step and washed in DEC during a couple of hours to remove traces of $KPF_6$ from the HC surface. This treatment is required despite it might partially dissolve organic components owing to higher solubilities of the potassium organic compounds (e.g., potassium alkyl carbonates and potassium alkoxides)[17,117]. Observations of the interior HC microstructure are performed on cracked microspheres in the electrode after 30 charge/discharge cycles in the [0.5M $KPF_6$ in EC:DEC + 4% wt.VC] electrolyte The HR-TEM image (Figure 7.9a) reveals that HC consists of curled graphitic layers which locally form "packets" and "cages". The shape of the C-K EELS edge of the pristine HC agrees with the observed structure being very similar to that in partially graphitized amorphous carbon. The C-K edge consists of a strong pre-peak at 285.5 eV originating from the $1s \rightarrow \pi^*$ electronic transition and a peak at 292.7 eV from the $1s \rightarrow \sigma^*$ transition (Figure 7.9c). In the HC material under study we did not detect any dome-like accumulation of graphitic packets as alleged earlier in the literature[181,182]. The structure of the C-K EELS edge of the cycled HC looks very similar to that of the pristine one, except of two clear peaks at 297.5 and 300.1 eV belonging to the K-$L_{2,3}$ edge (Figure 7.9c). This indicates that significant amount of K remains irreversibly trapped in HC.

HAADF-STEM imaging allows us to define the positions in HC, which are responsible for irreversible K trapping. The contrast in the HAADF-STEM image scales roughly as $Z^2$ (Z – is the average atomic number), thus potassium (Z = 19) and carbon (Z = 6) can be reliably discerned. HAADF-STEM image in Figure 7.9b shows a packet of graphitic layers (visible as layers of grey dots marked with black arrowheads) with virtually no scattering power in the interlayer space. In contrast to that, the cages (marked with white arrowheads) clearly contain K ions visible as prominently brighter dots. Thus, one may conclude that the positions between the graphitic layers intercalate $K^+$-ion in a reversible manner whereas the cages serve as traps for the K atoms.
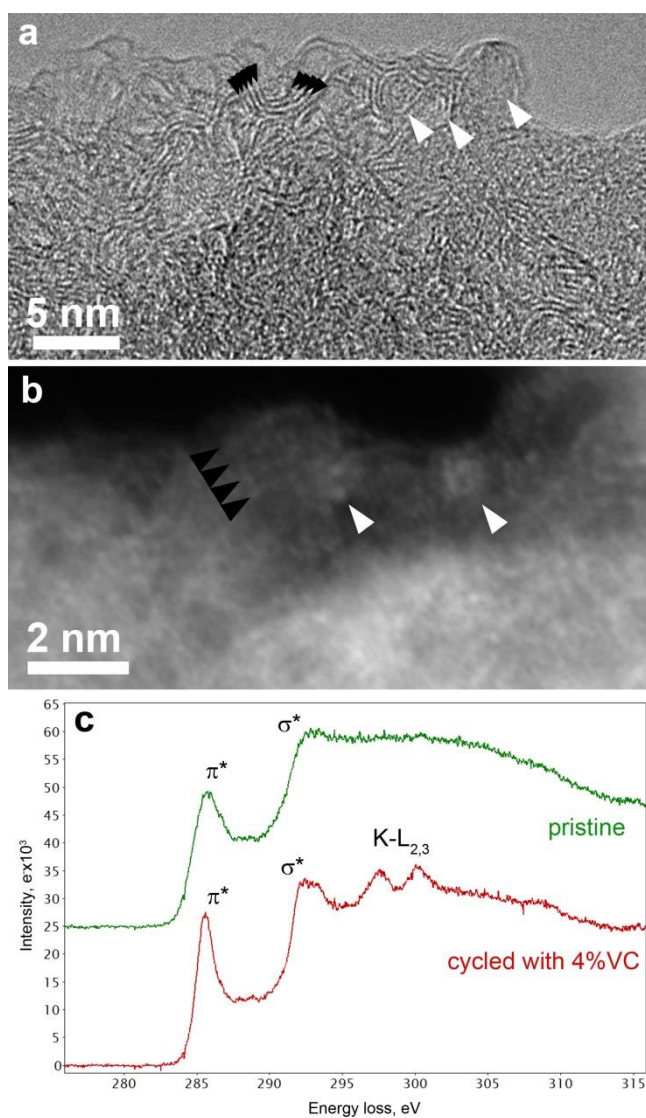
Figure 7.9. The HC microstructure upon 30 charge/discharge cycles in the [0.5M KPF$_6$ in EC:DEC + 4% wt.VC] electrolyte: (a) HR-TEM image indicates the presence of packets of curved graphitic layers (black arrowheads) and round cages (white arrowheads); (b) HAADF-STEM image shows graphitic packets (black arrowheads) with no remaining potassium and cages (white arrowheads) where the K atoms are trapped; (c) C-K EELS edges in the pristine and 30 times cycled HC.
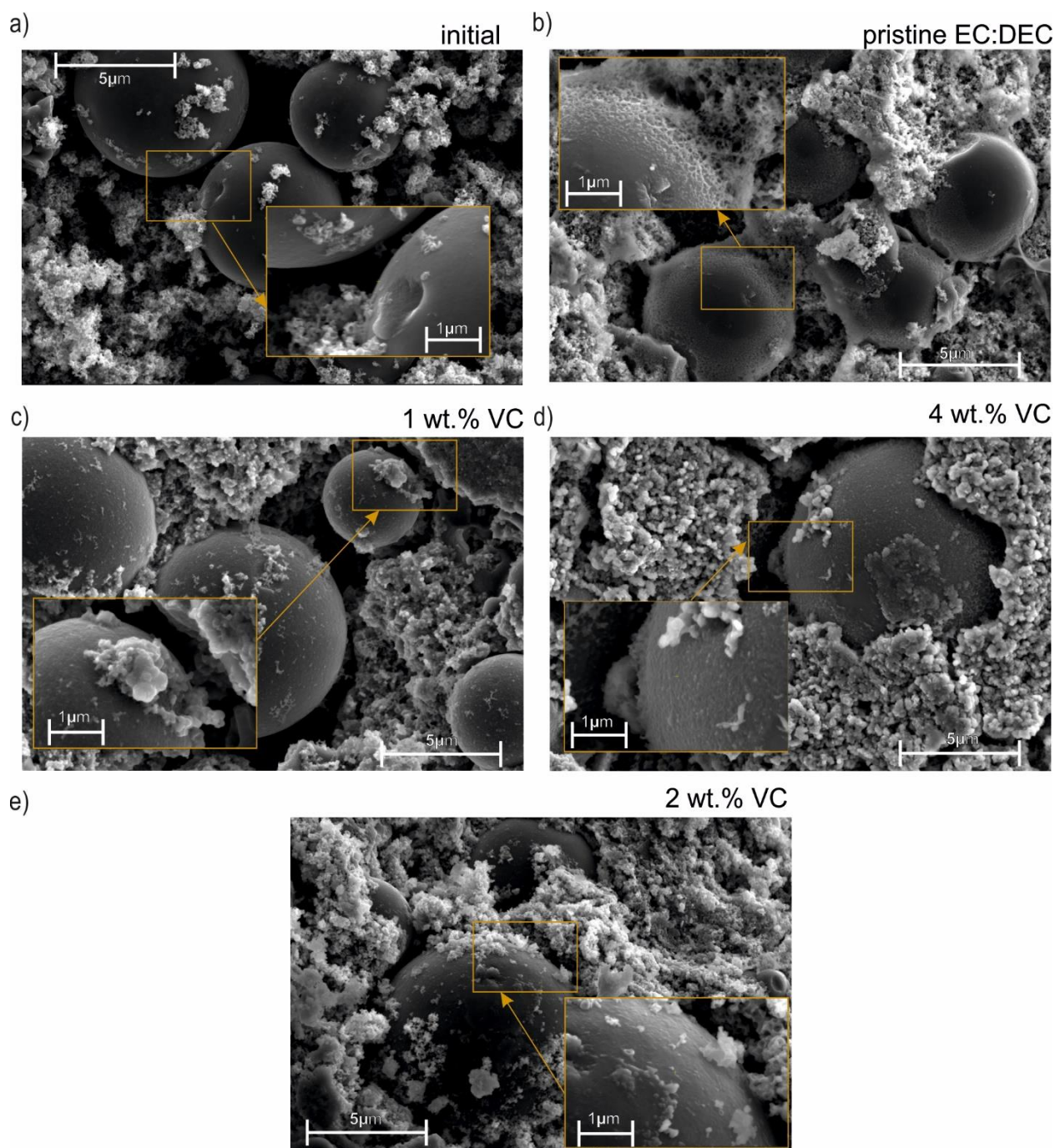
Figure 7.10. The scanning electron microscopy (SEM) image of the hard carbon anode illustrating the initial electrode morphology (a) and the morphology change after 30 cycles in the pristine carbonate-based electrolyte (b) 0.5 KPF$_6$/EC:DEC(1:1, v:v) and in electrolyte solutions containing 1 wt.% VC (c), 4 wt.% VC (d) and 2 wt.% VC (e) in the potential range 0.010 – 2.5 V vs K$^+$/K.

Figures 7.10 show changes in the electrode morphology depending on the electrolyte composition. The HC particles of the initial electrode possess the smooth surface (Figure 7.10a) whereas the heap of vague shape corresponds to the Na-CMC binder and carbon additive. Upon cycling in the pristine carbonate-based electrolyte, the HC surface appears to be very uneven (Figure 7.10b). The uneven layer covering the HC sphere distinguishes in the composition from

the main particle and, hence, it is assigned to the formation of the SEI film (Figure 7.11, table 7.1). A significant part of the surface of HC spheres appears to be intact indicating that SEI is either not formed or it is very thin. Other parts of the spheres are covered with crumble porous substance. Ideally, the passivating film should be uniformly distributed over the HC surface to provide the stable electrochemical behavior. Otherwise, the presence of open areas results in the continuous electrolyte decomposition at higher current densities. Thus, one possible implication of this is that the detected drastic capacity fade of K-half cell with the pristine carbonate-based electrolyte solution could be attributed to uneven SEI formation. Furthermore, the continuous reduction of electrolyte components leads to observed ICL and lower values of CE during cycling as discussed above. More information on the structure and composition of the SEI layer formed in the pristine carbonate-based electrolyte can be inferred from the HAADF-STEM imaging and STEM-EDX mapping (Figure 7.12). The surface of the HC spheres is decorated with the particles (Figure 7.12a,b) which may acquire faceted shape (Figure 7.12b) indicating their crystalline nature. STEM-EDX mapping shows that beneath the particle there is a continuous layer with the thickness of ~100 nm. Both particles and layer consist of K, O and F with no or very minor carbon component. Thus, SEI in the pristine carbonate-based electrolyte is formed mainly by inorganic components that are supported by the previous research works introducing $A_2CO_3$ (where A- alkali metal Li, Na, K) as the major SEI component with small inclusions of alkyl carbonates, oligomeric species of polyethylene oxide, and oxalates, and alkali metal fluorides[6,170,183].
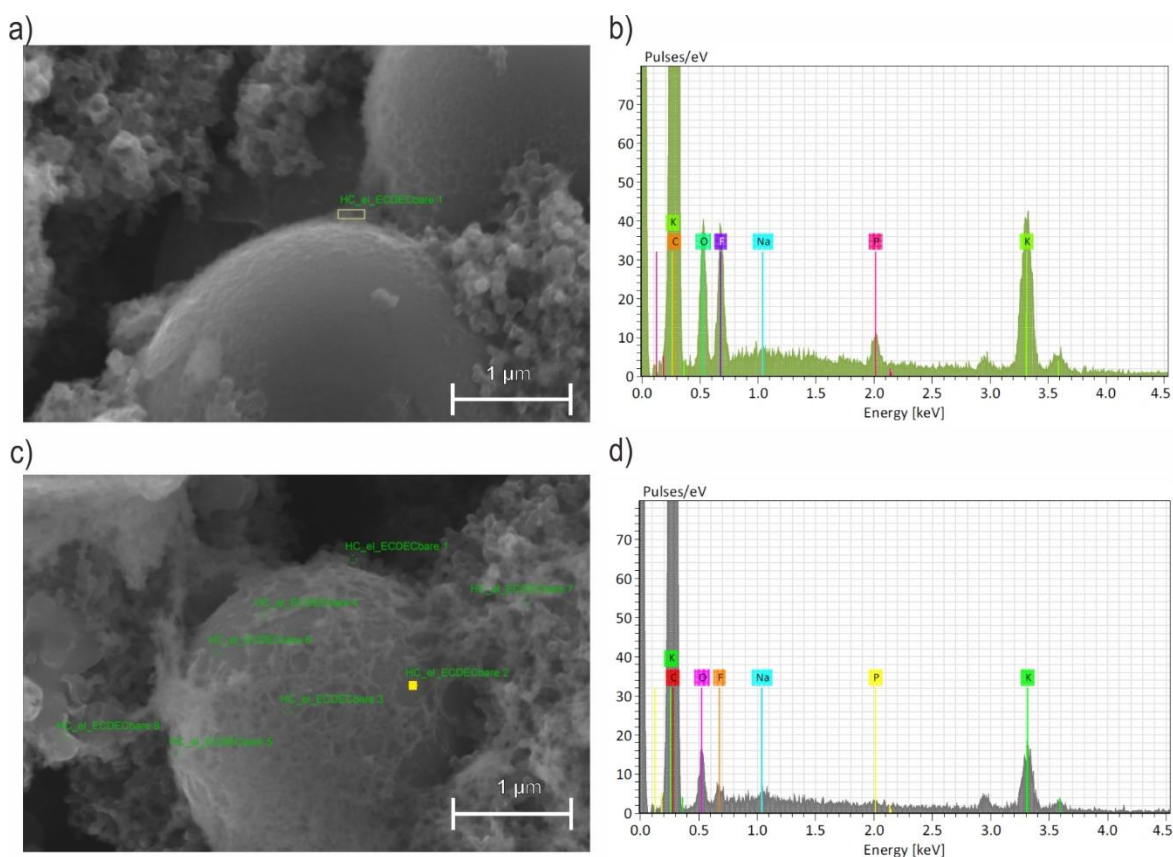
Figure 7.11. The scanning electron microscopy (SEM) images (a,c) and corresponding Energy-dispersive X-ray spectroscopy (EDX) spectra (b,d) measured from the marked yellow area which illustrate the morphology and composition of the hard carbon anode after 30 cycles in pristine 0.5 $KPF_6$/EC:DEC(1:1, v:v) in the potential range $0.010 – 2.5$ V vs $K^+$/K.

Table 7.1. Energy-dispersive X-ray spectroscopy (EDX) data for two hard carbon areas presented at Figure 7.11a,c illustrating the distinction in their composition

| Element | Hard carbon area from Figure 7.12a, mass.% | Hard carbon area from Figure 7.12c, mass.% |
|---|---|---|
| C | 79.02 | 89.59 |
| O | 5.82 | 3.37 |
| K | 12.74 | 6.95 |
| P | 0 | 0.09 |
| F | 2.42 | 0 |
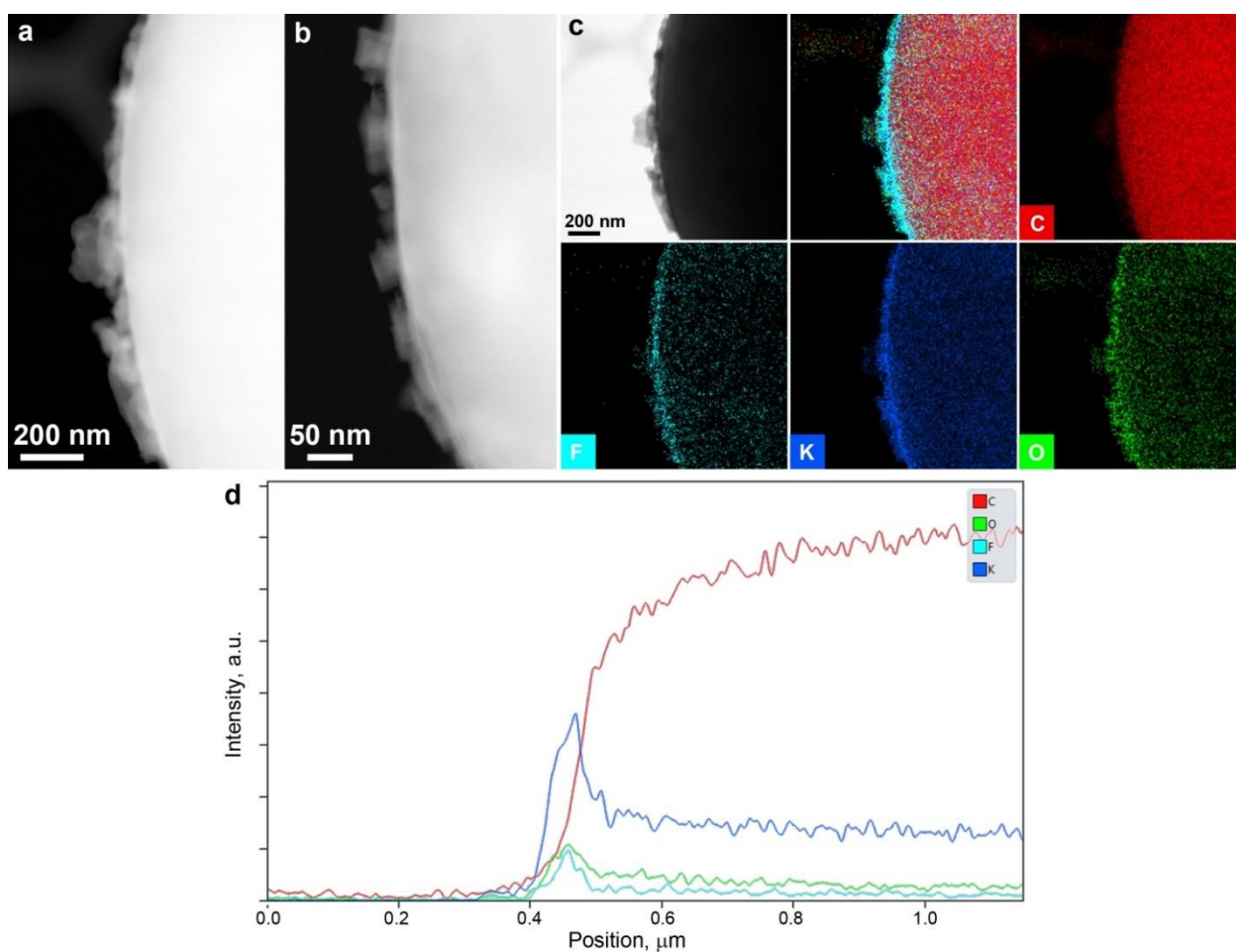


Figure 7.12. TEM characterization of the SEI layer formed after 30 charge/discharge cycles in the [0.5M $KPF_6$ in EC:DEC] electrolyte: a,b) HAADF-STEM images of the surface layers at two

different HC particles; c) HAADF-STEM image, individual elemental STEM-EDX maps and a mixed color-coded EDX map; d) EDX signal intensity profiles across the surface of the HC particle.

The formation of a dense and uniformly distributed SEI layer on the HC surface is observed on the electrodes cycled in the electrolyte with 1% and 4% VC addition (Figure 7.10c,d). VC is reported to improve the mechanical properties of the SEI layer in metal-ion batteries, particularly to increase its elasticity and resistance to HC expansion/contraction in the course of cycling[168,169]. TEM observations on the HC electrodes cycled in the electrolyte with VC additive reflect significant difference in the SEI structure and composition compared to that in the pristine electrolyte.
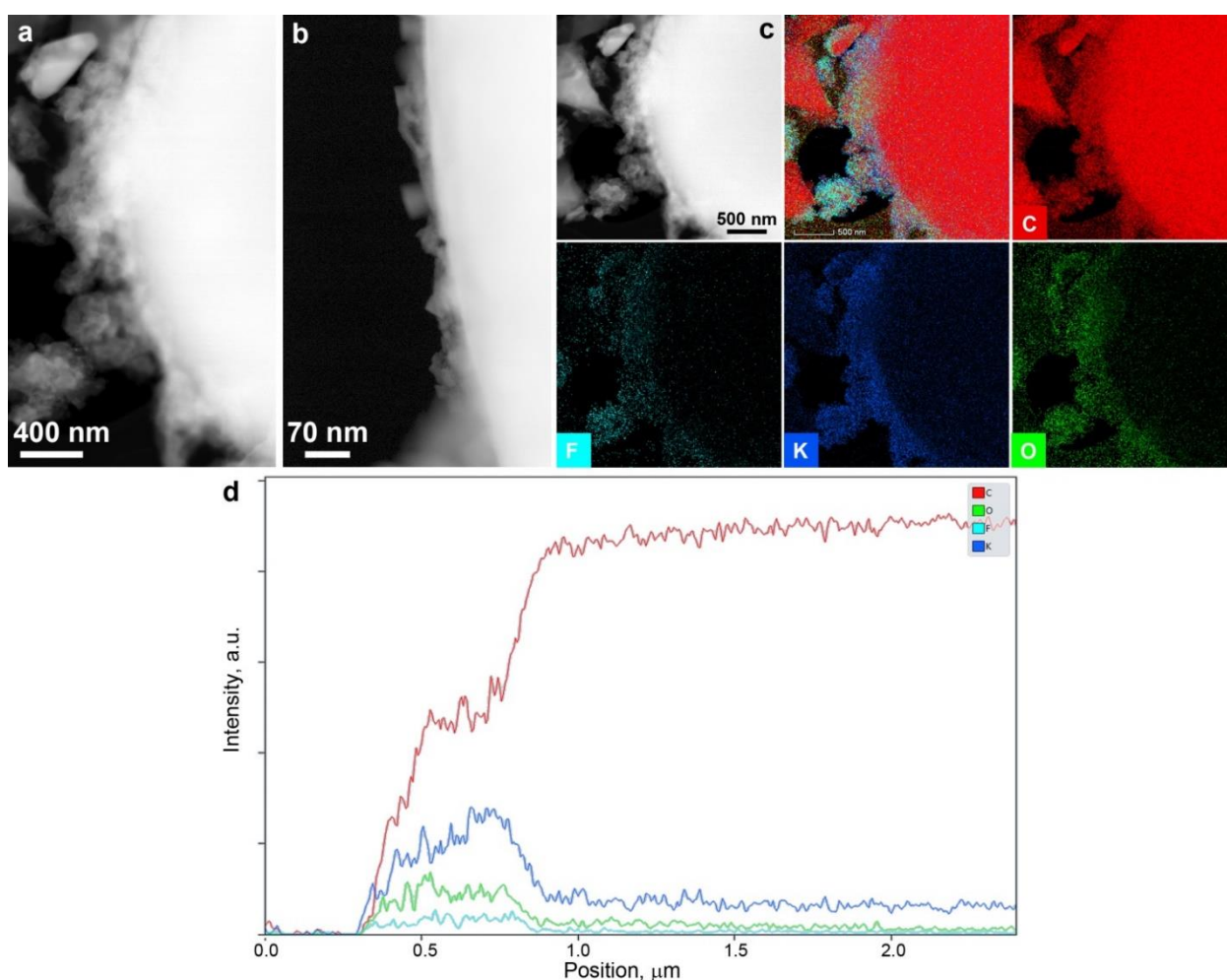


Figure 7.13. TEM characterization of the SEI layer formed after 30 charge/discharge cycles in the [0.5M KPF$_6$ in EC:DEC] electrolyte with 1% VC: a,b) HAADF-STEM images of the surface layers at two different HC particles; c) HAADF-STEM image, individual elemental STEM-EDX maps and a mixed color-coded EDX map; d) EDX signal intensity profiles across the surface of the HC particle.

HAADF-STEM images demonstrate that with 1% VC the SEI layer is thicker compared to that in the pristine electrolyte and reaches the thickness of 0.5 μm (Figure 7.13a). At the same time, the areas are present where the SEI is significantly thinner (Figure 7.13b) and contains faceted crystals reminiscent to the inorganic SEI component observed in the pristine electrolyte. STEM-EDX mapping of the thicker parts of SEI show that it also contains K, O and F, but also a lot of carbon (Figure 7.13c,d). Thus, the formation of $K_2CO_3$, $K_2C_2O_4$, $K_2O$, KF, semicarbonates K-O-C, polyolefins, carboxylates; potassium alkyl decarbonate salts (potassium vinylene dicarbonate $(CHOCO_2K)_2$, potassium divinylene dicarbonate $(CH=CHOCO_2K)_2$, potassium divinylene dialkoxide $(CH=CHOK)_2$) upon the reduction of electrolyte components is anticipated[6,184,185]. Similar observations have also been made on the SEI formed in the electrolyte with 4% VC (Figure 7.14).
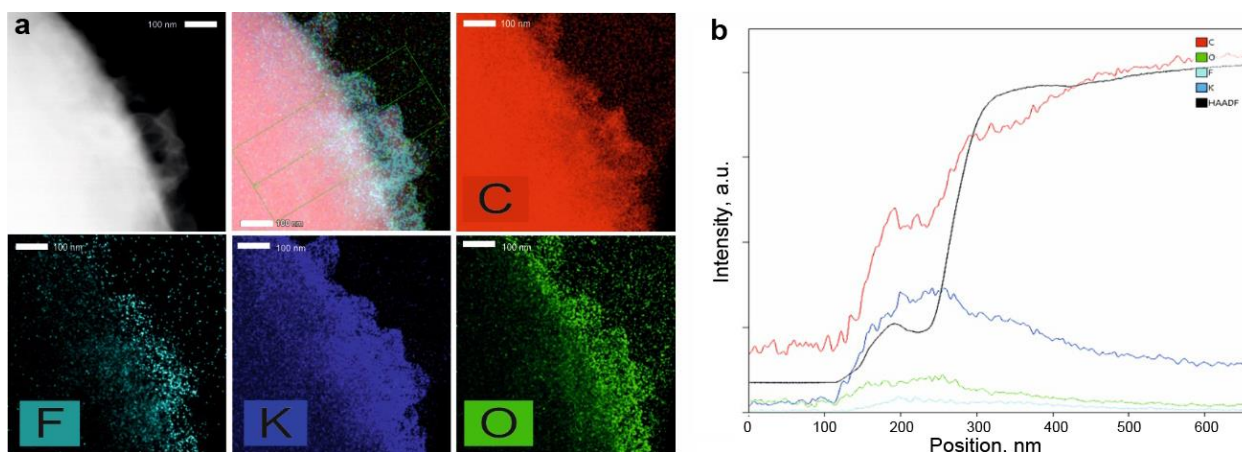


Figure 7. 14. TEM characterization of the SEI layer formed after 30 charge/discharge cycles in the [0.5M $KPF_6$ in EC:DEC] electrolyte with 4% VC: a) HAADF-STEM image, individual elemental STEM-EDX maps and a mixed color-coded EDX map; b) EDX and HAADF signal intensity profiles across the surface of the HC particle.

The other observed fact is related to extrusion of Na atoms from a binder Na-CMC under substitution with K (Figure 7.15). Thus, irreversible consumption of $K^+$-ions by a binder also contributes to increasing ICL value. However, EELS and EDX data did not reveal $Na^+$ ions in the HC electrode bulk (Figure 7.16). Moreover, the HC electrode composites with a Na-CMC binder are published to demonstrate improved capacity retention and cycle stability over commonly used polyvinylidene fluoride (PVDF) in $K^+$-systems[122,186].
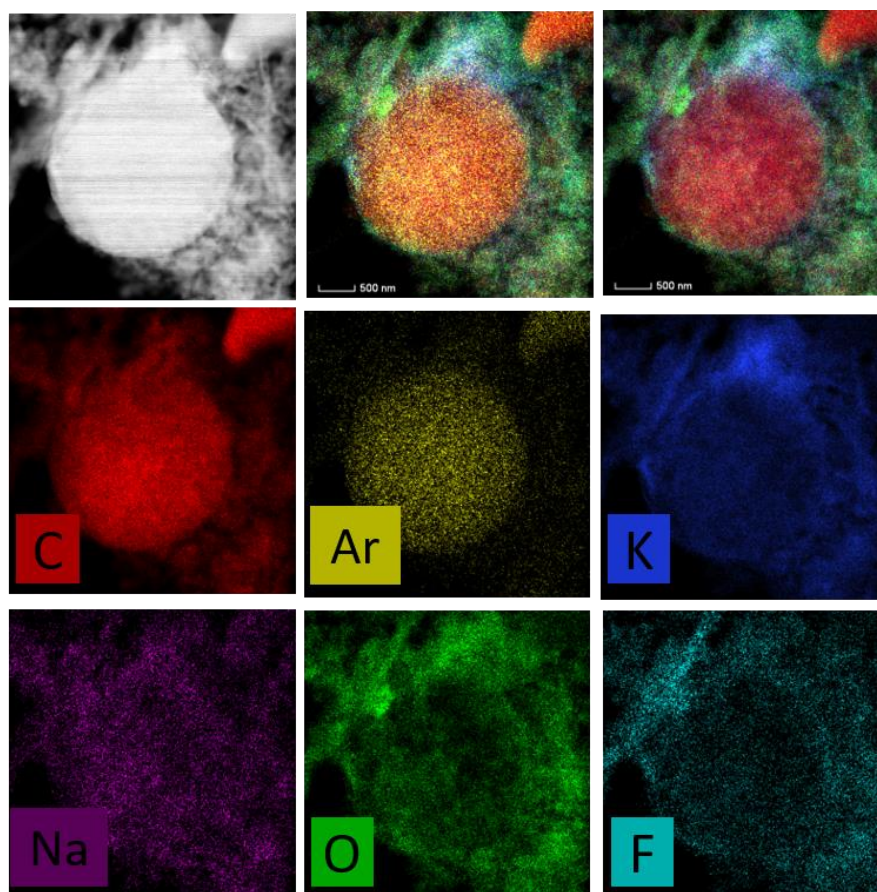
Figure 7.15. HAADF-STEM images accomplished with mapping by EDX illustrate the distribution of C, F, K, O, Ar and Na over HC particles after 30 cycles in pristine 0.5M $KPF_6$/EC:DEC (1:1, v:v).
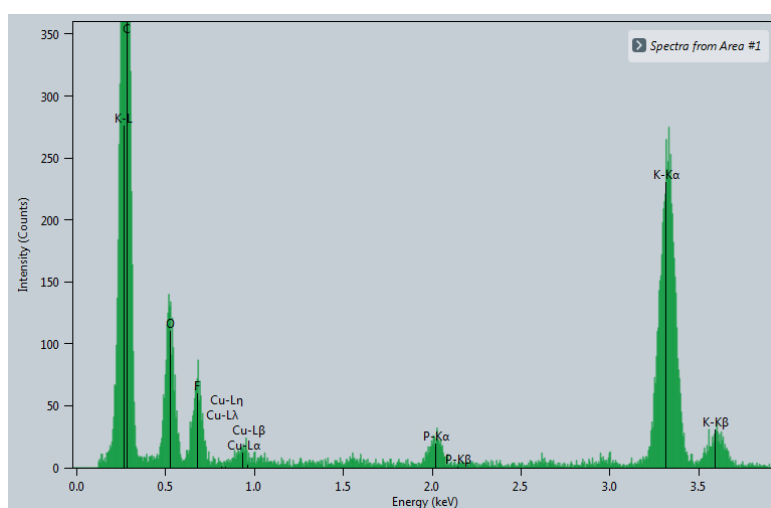


Figure 7.16. Typical EDX spectrum of HC particles after 30 cycles in pristine 0.5M $KPF_6$/EC:DEC (1:1, v:v).

Figure 7.17 schematically summarizes the hypothesized process of SEI formation and growth with and without the VC additive. In a pristine carbonate-based solution, the SEI layer starts to form when electrolyte components (solvent molecules and salt anions) decompose on the

HC surface. We assume that the subsequent intercalation of $K^+$-ions results in the particle expansion and the SEI cracking. Freshly exposed HC surface reacts with the electrolyte components forming new SEI that further diminishes the CE values. When VC is added, its reduction shifts the SEI nucleation potential to lower values as compared with the pristine electrolyte solution and changes its composition. The findings of this study suggest that the modified SEI layer with more polymeric components possesses higher elasticity and survives the HC expansion/contraction during $K^+$ intercalation/ deintercalation.
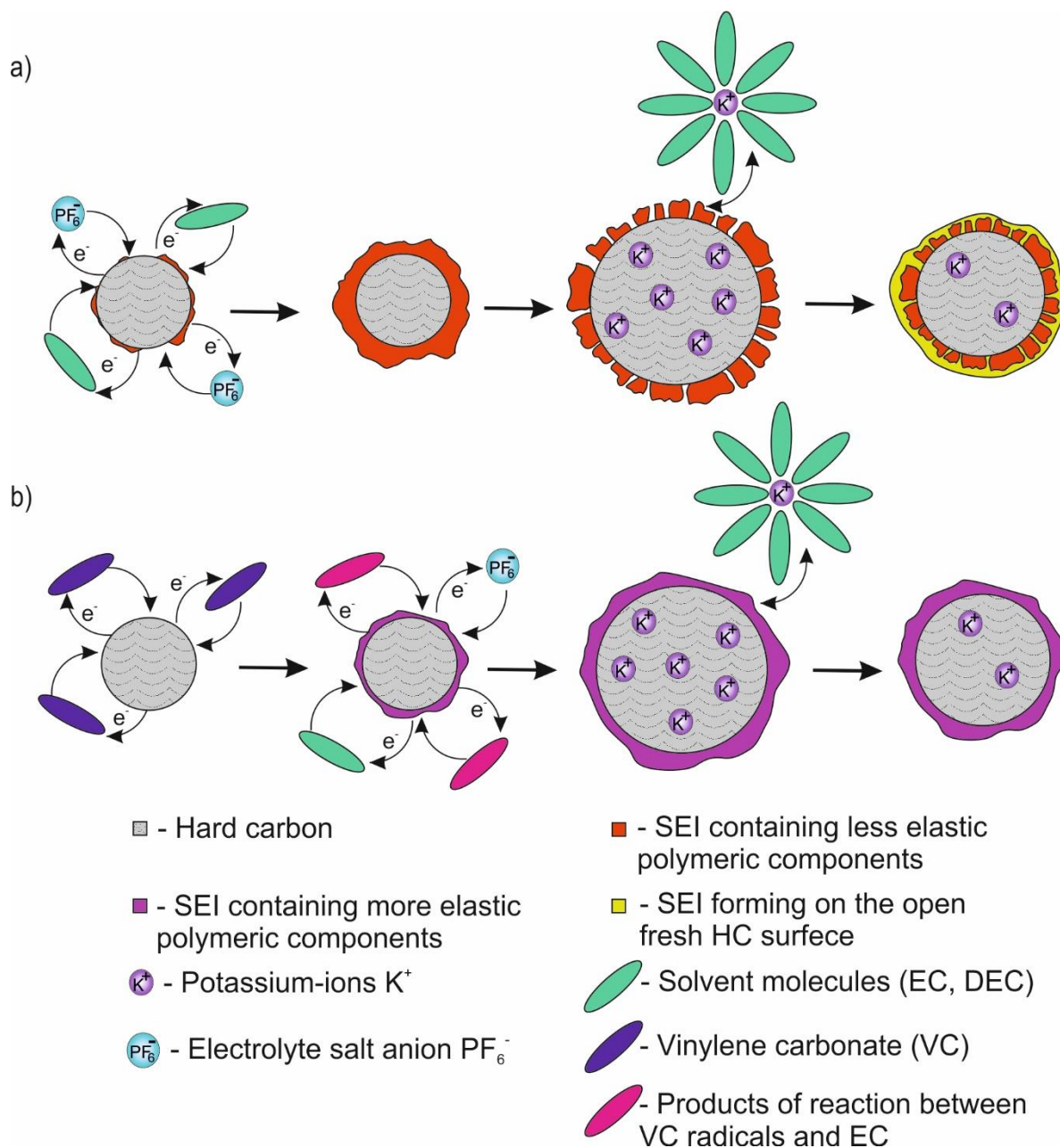


Figure 7. 17. Schematic of SEI formation on HC surface in electrolyte solutions without (a) and with (b) the VC electrolyte additive (the coordination number for K+ equals 8 in carbonate-based electrolytes[76])

**Conclusion**

A combination of electrochemical measurements, in situ AFM, SEM and TEM imaging and spectroscopy observations reflects several origins of irreversible capacity loss (ICL) in hard carbon (HC) negative electrode material for $K^+$-ion batteries. The internal HC structure is built of curled graphitic layers either arranged into "packets" of few nm in size or forming "cages" 1-2 nm in diameter. The positions between the graphitic layers within the packets are available for reversible $K^+$ (de)intercalation, whereas the cages trap the $K^+$ irreversibly thus contributing to ICL. Electrolyte additives play crucial role in enhancing/reducing the ICL affecting the onset potential for SEI formation, its structure, composition and stability. In pristine carbonate-based electrolyte SEI is formed mainly by inorganic components consisting of K, O and F, whereas the VC additive brings substantial carbon-based component to the SEI. One may speculate that this presumably polymeric organic component improves the mechanical properties of the SEI making it more resistant towards fracturing and more effectively preventing the electrolyte decomposition process thus reducing ICL. Additional contribution to ICL is made by the Na-carboxymethyl cellulose binder where $Na^+$ is exchanged by $K^+$ resulting in irreversible loss of potassium. These factors must be taken into account in the future design of PIBs.

**Chapter 8. Summary and Outlook**

The foremost findings of the present study are crucial for $K^+$-ion battery elaboration and are listed below:

1.  The hydrothermal carbonization technique ($T^I = 180°C$; t=16 h) with subsequent annealing at $T^{II} = 1500°C$ was elaborated to attain superb electrochemical performance of hard carbon microspheres as negative electrodes in K cells. The presence of "nanosized" particles significantly contributes to the irreversible capacity loss at the first cycles. The enhanced content of "nanospheres" leads to lower CE values during the first formation cycles and to a faster degradation of the PIB with a [0.5 M $KPF_6$ / EC: DEC (1: 1 by volume ratio)] electrolyte solution. The optimized synthesis conditions enhance the CE value up to 67% at the first cycle and the capacity retention up to 89% upon 30 cycles in K half cell utilizing carbonate-based electrolyte solution.

2.  A decrease in free solvent molecule number with increasing electrolyte concentration is found in [$x$ M $KPF_6$/G2] electrolytes (where $x$=1; 1.5; 2; 2.5), which results in a better aluminum current collector stability, formation of thinner solid electrolyte interphase (SEI) passivation layers, and further inhibition of solvent degradation redox processes occurring at the electrode surface upon cycling. The $KVOPO_4$ and $K_{1.44}Mn[Fe(CN)_6]_{0.9} \times 0.4H_2O$ cathodes exhibit an enhanced specific discharge capacity (54 and 105 $mA \cdot h \cdot g^{-1}$, respectively) in $K^+$-ion cells with the highest electrolyte concentrations (2 and 2.5 M $KPF_6$ in diglyme, respectively) at a 0.1 C rate.

3.  The capacity retention of 86 % after 300 cycles at 0.6C rate with a specific capacity value of 90 $mAh \cdot g^{-1}$ of cathode was observed for K full cell comprising $K_{1.44}Mn[Fe(CN)_6]_{0.9} \times 0.4H_2O$ and HC electrodes with ether-based electrolyte solution.

4.  The internal HC structure is built of curled graphitic layers either arranged into "packets" of few nm in size or forming "cages" 1-2 nm in diameter. The positions between the graphitic layers within the packets are available for reversible $K^+$ (de)intercalation, whereas the cages trap the $K^+$ irreversibly thus contributing to ICL.

5.  Electrolyte additives play crucial role in enhancing/reducing the ICL affecting the onset potential for SEI formation, its structure, composition and stability. In pristine carbonate-based electrolyte SEI is formed mainly by inorganic components consisting of K, O and F, whereas the VC additive brings substantial carbon-based component to the SEI. One may speculate that this presumably polymeric organic component improves the mechanical properties of the SEI making it more resistant towards fracturing and more effectively preventing the electrolyte decomposition process thus reducing ICL.

Apparently, the numerous issues should be addressed to organic electrolyte solution to design K full cell with prolonged cycle life and high energy density characteristics such as electrolyte oxidative stability, Al current collector corrosion and the ability to form the stable passivation layer that conducts $K^+$-ions on both cathode and anode sides. Yet the electrolyte choice is unique for each pair of negative and positive electrodes. Indeed, the measurements in K half cell to examine intrinsic properties of electrode material should be conducted carefully with the respect to K metal as the capacity fade might originate from growing thick layer on its surface.

Regarding, the K full cell comprising KMFCN and HC electrodes, further development of ether-based electrolyte solution composition should contain the concentration optimization of electrolyte additive with the reduction potential preceding the solvent reduction like VC, ethylene sulfite (ES) or 4-chloromethyl-1,3,2-dioxathiolane-2-oxide (CMDO). Presumably, this approach facilitates the stable SEI formation on HC surface and, thus, preventing electrolyte decomposition and decreasing the irreversible capacity loss. Furthermore, safety issues arise concerning the emission of CN groups in the case of thermal runaway. Thereby, the electrolyte additive acting as CN gas scavenger must be developed to elaborate safe $K^+$-ion battery.

Furthermore, concentrated KFSI-based electrolyte benefits the electrochemical performance of K full cell comprising carbonaceous negative electrodes since it sufficiently passivates the anode surface and possess oxidative stability against Al current collector corrosion. However, high cost of KFSI salt does not approach the requirements from stationary storage market. Hence, future research should be focused on elaboration of $KPF_6$/KFSI binary-salt solutions or artificial SEI design. The artificial thin SEI layer formation in concentrated KFSI-based electrolyte before cycling might be a proper compromise between the utilization of expensive KFSI salt and its profit in stable SEI formation on hard carbon anode.

## Bibliography

(1)    Ralon, P.; Taylor, M.; Ilas, A.; Diaz-Bone, H.; Kairies, K.-P. *"Electricity Storage and Renewables: Costs and Markets to 2030.";* Abu Dhabi, 2017.

(2)    Посыпанко, Н.; Баранов, М.; Костюк, Р. Накопители энергии в России: инъекция устойчивого развития - VYGON.Consulting.

(3)    Huggins, R. A. (Robert A. Advanced Batteries : Materials Science Aspects. **2008**, 474.

(4)    Nikitina, V. A. Charge Transfer Processes in the Course of Metal-Ion Electrochemical Intercalation. *Curr. Opin. Electrochem.* **2020**, *19*, 71–77. https://doi.org/10.1016/J.COELEC.2019.10.006.

(5)    Chekushkin, P. M.; Merenkov, I. S.; Smirnov, V. S.; Kislenko, S. A.; Nikitina, V. A. The Physical Origin of the Activation Barrier in Li-Ion Intercalation Processes: The Overestimated Role of Desolvation. *Electrochim. Acta* **2021**, *372*, 137843. https://doi.org/10.1016/J.ELECTACTA.2021.137843.

(6)    Peled, E.; Menkin, S. Review—SEI: Past, Present and Future. *J. Electrochem. Soc.* **2017**, *164* (7), A1703–A1719. https://doi.org/10.1149/2.1441707JES.

(7)    Jow, T. R.; Delp, S. A.; Allen, J. L.; Jones, J.-P.; Smart, M. C. Factors Limiting Li+ Charge Transfer Kinetics in Li-Ion Batteries. *J. Electrochem. Soc.* **2018**, *165* (2), A361. https://doi.org/10.1149/2.1221802JES.

(8)    Keefe, A. S.; Buteau, S.; Hill, I. G.; Dahn, J. R. Temperature Dependent EIS Studies Separating Charge Transfer Impedance from Contact Impedance in Lithium-Ion Symmetric Cells. *J. Electrochem. Soc.* **2019**, *166* (14), A3272. https://doi.org/10.1149/2.0541914JES.

(9)    Bard, Allen J.; Faulkner, Larry, R. Electrochemical Methods: Fundmanentals and Applications. *Electrochem. METHODS Fundmanentals Appl.* **2001**, 1–833.

(10)   Aurbach, D.; Levi, M. D.; Levi, E. A Review on the Solid-State Ionics of Electrochemical Intercalation Processes: How to Interpret Properly Their Electrochemical Response. *Solid State Ionics* **2008**, *21–26* (179), 742–751. https://doi.org/10.1016/J.SSI.2007.12.070.

(11)   Li, Y.; Chen, H.; Lim, K.; Deng, H. D.; Lim, J.; Fraggedakis, D.; Attia, P. M.; Lee, S. C.; Jin, N.; Moškon, J.; Guan, Z.; Gent, W. E.; Hong, J.; Yu, Y.-S.; Gaberšček, M.; Islam, M. S.; Bazant, M. Z.; Chueh, W. C. Fluid-Enhanced Surface Diffusion Controls Intraparticle Phase Transformations. *Nat. Mater. 2018 1710* **2018**, *17* (10), 915–922. https://doi.org/10.1038/s41563-018-0168-4.

(12)   Kubota, K.; Dahbi, M.; Hosaka, T.; Kumakura, S.; Komaba, S. Towards K-Ion and Na-Ion Batteries as "Beyond Li-Ion." *Chem. Rec.* **2018**, *18* (4), 459–479. https://doi.org/10.1002/tcr.201700057.

(13) Jian, Z.; Luo, W.; Ji, X. Carbon Electrodes for K-Ion Batteries. *J. Am. Chem. Soc.* **2015**, *137* (36), 11566–11569. https://doi.org/10.1021/JACS.5B06809.

(14) Nikitina, V. A.; Kuzovchikov, S. M.; Fedotov, S. S.; Khasanova, N. R.; Abakumov, A. M.; Antipov, E. V. Effect of the Electrode/Electrolyte Interface Structure on the Potassium-Ion Diffusional and Charge Transfer Rates: Towards a High Voltage Potassium-Ion Battery. *Electrochim. Acta* **2017**, *258*, 814–824. https://doi.org/10.1016/j.electacta.2017.11.131.

(15) Fedotov, S. S.; Samarin, A. S.; Nikitina, V. A.; Aksyonov, D. A.; Sokolov, S. A.; Zhugayevych, A.; Stevenson, K. J.; Khasanova, N. R.; Abakumov, A. M.; Antipov, E. V. Reversible Facile Rb+ and K+ Ions de/Insertion in a KTiOPO4-Type RbVPO4F Cathode Material. *J. Mater. Chem. A* **2018**, *6* (29), 14420–14430. https://doi.org/10.1039/c8ta03839b.

(16) Ramadass, P.; Haran, B.; White, R.; Popov, B. N. Mathematical Modeling of the Capacity Fade of Li-Ion Cells. *J. Power Sources* **2003**, *123* (2), 230–240. https://doi.org/10.1016/S0378-7753(03)00531-7.

(17) Hosaka, T.; Kubota, K.; Hameed, A. S.; Komaba, S. Research Development on K-Ion Batteries. *Chem. Rev.* **2020**, *120* (14), 6358–6466. https://doi.org/10.1021/ACS.CHEMREV.9B00463.

(18) Shirane, T.; Kanno, R.; Kawamoto, Y.; Takeda, Y.; Takano, M.; Kamiyama, T.; Izumi, F. Structure and Physical Properties of Lithium Iron Oxide, LiFeO 2 , Synthesized by Ionic Exchange Reaction. *Solid State Ionics* **1995**, No. 79, 227–233.

(19) Claude Delmas, M.; Fouassier, C.; Hagenmuller, P. Stabilite Relative Des Environnements Octaedrique et Prismatique Triangulaire Dans Les Oxydes Lamellaires Alcalins AxMO2 (x ⩽ 1). *Mater. Res. Bull.* **1976**, *11* (12), 1483–1488. https://doi.org/10.1016/0025-5408(76)90098-2.

(20) Hoffmann, L.; Hoppe, R. Zur Kenntnis Des A-LiFeO2-Typs. *ZAAC - J. Inorg. Gen. Chem.* **1977**, *430* (1), 115–120. https://doi.org/10.1002/ZAAC.19774300111.

(21) Kubota, K.; Kumakura, S.; Yoda, Y.; Kuroki, K.; Komaba, S. Electrochemistry and Solid-State Chemistry of NaMeO2 (Me = 3d Transition Metals). *Adv. Energy Mater.* **2018**, *8* (17), 1703415. https://doi.org/10.1002/AENM.201703415.

(22) Rouxel, J. Sur Un Diagramme Ionicité-Structure Pour Les Composes Intercalaires Alcalins Des Sulfures Lamellaires. *J. Solid State Chem.* **1976**, *17* (3), 223–229. https://doi.org/10.1016/0022-4596(76)90126-2.

(23) Shannon, R. D.; IUCr. Revised Effective Ionic Radii and Systematic Studies of Interatomic Distances in Halides and Chalcogenides. *urn:issn:0567-7394* **1976**, *32* (5), 751–767. https://doi.org/10.1107/S0567739476001551.

(24) Kim, H.; Seo, D. H.; Urban, A.; Lee, J.; Kwon, D. H.; Bo, S. H.; Shi, T.; Papp, J. K.; McCloskey, B. D.; Ceder, G. Stoichiometric Layered Potassium Transition Metal Oxide for Rechargeable Potassium Batteries. *Chem. Mater.* **2018**, *30* (18), 6532–6539. https://doi.org/10.1021/ACS.CHEMMATER.8B03228/SUPPL_FILE/CM8B03228_SI_00 1.PDF.

(25) Wang, X.; Xu, X.; Niu, C.; Meng, J.; Huang, M.; Liu, X.; Liu, Z.; Mai, L. Earth Abundant Fe/Mn-Based Layered Oxide Interconnected Nanowires for Advanced K-Ion Full Batteries. *Nano Lett.* **2017**, *17* (1), 544–550. https://doi.org/10.1021/ACS.NANOLETT.6B04611/SUPPL_FILE/NL6B04611_SI_001.P DF.

(26) Hoppe, R.; Sabrowsky, H. Oxoscandate Der Alkalimetalle: KScO2 Und RbScO2. *Zeitschrift für Anorg. und Allg. Chemie* **1965**, *339* (3–4), 144–154. https://doi.org/10.1002/ZAAC.19653390305.

(27) Delmas, C.; Devalette, M.; Fouassier, C.; Hagenmuller, P. Les Phases KXCrO2 (X ⩽ 1). *Mater. Res. Bull.* **1975**, *10* (5), 393–398. https://doi.org/10.1016/0025-5408(75)90010-0.

(28) Vaalma, C.; Giffin, G. A.; Buchholz, D.; Passerini, S. Non-Aqueous K-Ion Battery Based on Layered K 0.3 MnO 2 and Hard Carbon/Carbon Black . *J. Electrochem. Soc.* **2016**, *163* (7), A1295–A1299. https://doi.org/10.1149/2.0921607JES/XML.

(29) Kim, S. H.; Kim, S. J.; Oh, S. M. Preparation of Layered MnO2 via Thermal Decomposition of KMnO4 and Its Electrochemical Characterizations. *Chem. Mater.* **1999**, *11* (3), 557–563. https://doi.org/10.1021/CM9801643.

(30) Gaillot, A. C.; Drits, V. A.; Manceau, A.; Lanson, B. Structure of the Synthetic K-Rich Phyllomanganate Birnessite Obtained by High-Temperature Decomposition of KMnO4. Substructures of K-Rich Birnessite from 1000°C Experiment. *Microporous Mesoporous Mater.* **2007**, *98* (1–3), 267–282. https://doi.org/10.1016/J.MICROMESO.2006.09.010.

(31) Kim, H.; Seo, D. H.; Kim, J. C.; Bo, S. H.; Liu, L.; Shi, T.; Ceder, G. Investigation of Potassium Storage in Layered P3-Type K0.5MnO2 Cathode. *Adv. Mater.* **2017**, *29* (37), 1702480. https://doi.org/10.1002/ADMA.201702480.

(32) Jansen, M.; Chang, F. M.; Hoppe, R. Zur Kenntnis von KMnO2. *Zeitschrift für Anorg. und Allg. Chemie* **1982**, *490* (1), 101–110. https://doi.org/10.1002/ZAAC.19824900112.

(33) Delmas, C.; Fouassier, C.; Hagenmuller, P. Les Bronzes de Cobalt KxCoO2 (x < 1). L'oxyde KCoO2. *J. Solid State Chem.* **1975**, *13* (3), 165–171. https://doi.org/10.1016/0022-4596(75)90114-0.

(34) Jansen, M.; Hoppe, R. Zur Kenntnis Der Oxocobaltate AxCo2O4 Mit A = Cs, Rb, K. *Zeitschrift für Anorg. und Allg. Chemie* **1974**, *408* (2), 97–103.

https://doi.org/10.1002/ZAAC.19744080202.

(35) Hironaka, Y.; Kubota, K.; Komaba, S. P2- and P3-KxCoO2 as an Electrochemical Potassium Intercalation Host. *Chem. Commun.* **2017**, *53* (26), 3693–3696. https://doi.org/10.1039/C7CC00806F.

(36) Wang, X.; Hu, P.; Niu, C.; Meng, J.; Xu, X.; Wei, X.; Tang, C.; Luo, W.; Zhou, L.; An, Q.; Mai, L. New-Type K0.7Fe0.5Mn0.5O2 Cathode with an Expanded and Stabilized Interlayer Structure for High-Capacity Sodium-Ion Batteries. *Nano Energy* **2017**, *35*, 71–78. https://doi.org/10.1016/J.NANOEN.2017.03.026.

(37) Deng, T.; Fan, X.; Chen, J.; Chen, L.; Luo, C.; Zhou, X.; Yang, J.; Zheng, S.; Wang, C. Layered P2-Type K0.65Fe0.5Mn0.5O2 Microspheres as Superior Cathode for High-Energy Potassium-Ion Batteries. *Adv. Funct. Mater.* **2018**, *28* (28), 1800219. https://doi.org/10.1002/ADFM.201800219.

(38) Choi, J. U.; Kim, J.; Hwang, J. Y.; Jo, J. H.; Sun, Y. K.; Myung, S. T. K0.54[Co0.5Mn0.5]O2: New Cathode with High Power Capability for Potassium-Ion Batteries. *Nano Energy* **2019**, *61*, 284–294. https://doi.org/10.1016/J.NANOEN.2019.04.062.

(39) Choi, J. U.; Ji Park, Y.; Jo, J. H.; Jung, Y. H.; Ahn, D. C.; Jeon, T. Y.; Lee, K. S.; Kim, H.; Lee, S.; Kim, J.; Myung, S. T. An Optimized Approach toward High Energy Density Cathode Material for K-Ion Batteries. *Energy Storage Mater.* **2020**, *27*, 342–351. https://doi.org/10.1016/J.ENSM.2020.02.025.

(40) Masese, T.; Yoshii, K.; Yamaguchi, Y.; Okumura, T.; Huang, Z. D.; Kato, M.; Kubota, K.; Furutani, J.; Orikasa, Y.; Senoh, H.; Sakaebe, H.; Shikano, M. Rechargeable Potassium-Ion Batteries with Honeycomb-Layered Tellurates as High Voltage Cathodes and Fast Potassium-Ion Conductors. *Nat. Commun. 2018 91* **2018**, *9* (1), 1–12. https://doi.org/10.1038/s41467-018-06343-6.

(41) Xiao, P.; Song, J.; Wang, L.; Goodenough, J. B.; Henkelman, G. Theoretical Study of the Structural Evolution of a Na2FeMn(CN)6 Cathode upon Na Intercalation. *Chem. Mater.* **2015**, *27* (10), 3763–3768. https://doi.org/10.1021/ACS.CHEMMATER.5B01132.

(42) Paolella, A.; Faure, C.; Timoshevskii, V.; Marras, S.; Bertoni, G.; Guerfi, A.; Vijh, A.; Armand, M.; Zaghib, K. A Review on Hexacyanoferrate-Based Materials for Energy Storage and Smart Windows: Challenges and Perspectives. *J. Mater. Chem. A* **2017**, *5* (36), 18919–18932. https://doi.org/10.1039/C7TA05121B.

(43) Qian, J.; Wu, C.; Cao, Y.; Ma, Z.; Huang, Y.; Ai, X.; Yang, H. Prussian Blue Cathode Materials for Sodium-Ion Batteries and Other Ion Batteries. *Adv. Energy Mater.* **2018**, *8* (17), 1702619. https://doi.org/10.1002/AENM.201702619.

(44)  Bie, X.; Kubota, K.; Hosaka, T.; Chihara, K.; Komaba, S. A Novel K-Ion Battery: Hexacyanoferrate(Ii)/Graphite Cell. *J. Mater. Chem. A* **2017**, *5* (9), 4325–4330. https://doi.org/10.1039/c7ta00220c.

(45)  Xue, L.; Li, Y.; Gao, H.; Zhou, W.; Lü, X.; Kaveevivitchai, W.; Manthiram, A.; Goodenough, J. B. Low-Cost High-Energy Potassium Cathode. *J. Am. Chem. Soc.* **2017**, *139* (6), 2164–2167. https://doi.org/10.1021/JACS.6B12598/SUPPL_FILE/JA6B12598_SI_003.CIF.

(46)  Liao, J.; Hu, Q.; Yu, Y.; Wang, H.; Tang, Z.; Wen, Z.; Chen, C. A Potassium-Rich Iron Hexacyanoferrate/Dipotassium Terephthalate@carbon Nanotube Composite Used for K-Ion Full-Cells with an Optimized Electrolyte. *J. Mater. Chem. A* **2017**, *5* (36), 19017–19024. https://doi.org/10.1039/C7TA05460B.

(47)  Song, J.; Wang, L.; Lu, Y.; Liu, J.; Guo, B.; Xiao, P.; Lee, J. J.; Yang, X. Q.; Henkelman, G.; Goodenough, J. B. Removal of Interstitial H2O in Hexacyanometallates for a Superior Cathode of a Sodium-Ion Battery. *J. Am. Chem. Soc.* **2015**, *137* (7), 2658–2664. https://doi.org/10.1021/JA512383B/SUPPL_FILE/JA512383B_SI_002.CIF.

(48)  Wang, L.; Song, J.; Qiao, R.; Wray, L. A.; Hossain, M. A.; Chuang, Y. De; Yang, W.; Lu, Y.; Evans, D.; Lee, J. J.; Vail, S.; Zhao, X.; Nishijima, M.; Kakimoto, S.; Goodenough, J. B. Rhombohedral Prussian White as Cathode for Rechargeable Sodium-Ion Batteries. *J. Am. Chem. Soc.* **2015**, *137* (7), 2548–2554. https://doi.org/10.1021/JA510347S/SUPPL_FILE/JA510347S_SI_001.PDF.

(49)  Eftekhari, A. Potassium Secondary Cell Based on Prussian Blue Cathode. *J. Power Sources* **2004**, *126* (1–2), 221–228. https://doi.org/10.1016/J.JPOWSOUR.2003.08.007.

(50)  Zhu, Y. H.; Yin, Y. Bin; Yang, X.; Sun, T.; Wang, S.; Jiang, Y. S.; Yan, J. M.; Zhang, X. B. Transformation of Rusty Stainless-Steel Meshes into Stable, Low-Cost, and Binder-Free Cathodes for High-Performance Potassium-Ion Batteries. *Angew. Chemie Int. Ed.* **2017**, *56* (27), 7881–7885. https://doi.org/10.1002/ANIE.201702711.

(51)  Wu, X.; Jian, Z.; Li, Z.; Ji, X. Prussian White Analogues as Promising Cathode for Non-Aqueous Potassium-Ion Batteries. *Electrochem. commun.* **2017**, *77*, 54–57. https://doi.org/10.1016/J.ELECOM.2017.02.012.

(52)  Chong, S.; Chen, Y.; Zheng, Y.; Tan, Q.; Shu, C.; Liu, Y.; Guo, Z. Potassium Ferrous Ferricyanide Nanoparticles as a High Capacity and Ultralong Life Cathode Material for Nonaqueous Potassium-Ion Batteries. *J. Mater. Chem. A* **2017**, *5* (43), 22465–22471. https://doi.org/10.1039/C7TA08139A.

(53)  Zhang, C.; Xu, Y.; Zhou, M.; Liang, L.; Dong, H.; Wu, M.; Yang, Y.; Lei, Y. Potassium Prussian Blue Nanoparticles: A Low-Cost Cathode Material for Potassium-Ion Batteries.

*Adv. Funct. Mater.* **2017**, *27* (4). https://doi.org/10.1002/adfm.201604307.

(54)  Luo, Y.; Shen, B.; Guo, B.; Hu, L.; Xu, Q.; Zhan, R.; Zhang, Y.; Bao, S.; Xu, M. Potassium Titanium Hexacyanoferrate as a Cathode Material for Potassium-Ion Batteries. *J. Phys. Chem. Solids* **2018**, *122*, 31–35. https://doi.org/10.1016/J.JPCS.2018.06.014.

(55)  Islas-Vargas, C.; Guevara-García, A.; Oliver-Tolentino, M.; Ramos-Sánchez, G.; González, I.; Galván, M. Experimental and Theoretical Investigation on the Origin of the High Intercalation Voltage of K 2 Zn 3 [Fe(CN) 6 ] 2 Cathode . *J. Electrochem. Soc.* **2019**, *166* (3), A5139–A5145. https://doi.org/10.1149/2.0231903JES/XML.

(56)  Deng, L.; Yang, Z.; Tan, L.; Zeng, L.; Zhu, Y.; Guo, L. Investigation of the Prussian Blue Analog Co3[Co(CN)6]2 as an Anode Material for Nonaqueous Potassium-Ion Batteries. *Adv. Mater.* **2018**, *30* (31), 1802510. https://doi.org/10.1002/ADMA.201802510.

(57)  Hosaka, T.; Kubota, K.; Kojima, H.; Komaba, S. Highly Concentrated Electrolyte Solutions for 4 v Class Potassium-Ion Batteries. *Chem. Commun.* **2018**, *54* (60), 8387–8390. https://doi.org/10.1039/c8cc04433c.

(58)  He, G.; Nazar, L. F. Crystallite Size Control of Prussian White Analogues for Nonaqueous Potassium-Ion Batteries. *ACS Energy Lett.* **2017**, *2* (5), 1122–1127. https://doi.org/10.1021/ACSENERGYLETT.7B00179.

(59)  Chen, R.; Huang, Y.; Xie, M.; Zhang, Q.; Zhang, X.; Li, L.; Wu, F. Preparation of Prussian Blue Submicron Particles with a Pore Structure by Two-Step Optimization for Na-Ion Battery Cathodes. *ACS Appl. Mater. Interfaces* **2016**, *8* (25), 16078–16086. https://doi.org/10.1021/ACSAMI.6B04151.

(60)  Moritomo, Y.; Urase, S.; Shibata, T. Enhanced Battery Performance in Manganese Hexacyanoferrate by Partial Substitution. *Electrochim. Acta* **2016**, *210*, 963–969. https://doi.org/10.1016/J.ELECTACTA.2016.05.205.

(61)  Jiang, L.; Lu, Y.; Zhao, C.; Liu, L.; Zhang, J.; Zhang, Q.; Shen, X.; Zhao, J.; Yu, X.; Li, H.; Huang, X.; Chen, L.; Hu, Y. S. Building Aqueous K-Ion Batteries for Energy Storage. *Nat. Energy 2019 46* **2019**, *4* (6), 495–503. https://doi.org/10.1038/s41560-019-0388-0.

(62)  Li, Z.; Dadsetan, M.; Gao, J.; Zhang, S.; Cai, L.; Naseri, A.; Jimenez-Castaneda, M. E.; Filley, T.; Miller, J. T.; Thomson, M. J.; Pol, V. G. Revealing the Thermal Safety of Prussian Blue Cathode for Safer Nonaqueous Batteries. *Adv. Energy Mater.* **2021**, *11* (42), 2101764. https://doi.org/10.1002/AENM.202101764.

(63)  Manthiram, A.; Goodenough, J. B. Lithium Insertion into Fe2(SO4)3 Frameworks. *J. Power Sources* **1989**, *26* (3–4), 403–408. https://doi.org/10.1016/0378-7753(89)80153-3.

(64)  Manthiram, A.; Goodenough, J. B. Lithium Insertion into Fe2(MO4)3 Frameworks: Comparison of M = W with M = Mo. *J. Solid State Chem.* **1987**, *71* (2), 349–360.

https://doi.org/10.1016/0022-4596(87)90242-8.

(65) Hosaka, T.; Shimamura, T.; Kubota, K.; Komaba, S. Polyanionic Compounds for Potassium-Ion Batteries. *Chem. Rec.* **2019**, *19* (4), 735–745. https://doi.org/10.1002/TCR.201800143.

(66) Park, W. B.; Han, S. C.; Park, C.; Hong, S. U.; Han, U.; Singh, S. P.; Jung, Y. H.; Ahn, D.; Sohn, K. S.; Pyo, M. KVP2O7 as a Robust High-Energy Cathode for Potassium-Ion Batteries: Pinpointed by a Full Screening of the Inorganic Registry under Specific Search Conditions. *Adv. Energy Mater.* **2018**, *8* (13). https://doi.org/10.1002/AENM.201703099.

(67) Chihara, K.; Katogi, A.; Kubota, K.; Komaba, S. KVPO4F and KVOPO4 toward 4 Volt-Class Potassium-Ion Batteries. *Chem. Commun.* **2017**, *53* (37), 5208–5211. https://doi.org/10.1039/c6cc10280h.

(68) Han, J.; Li, G. N.; Liu, F.; Wang, M.; Zhang, Y.; Hu, L.; Dai, C.; Xu, M. Investigation of K3V2(PO4)3/C Nanocomposites as High-Potential Cathode Materials for Potassium-Ion Batteries. *Chem. Commun.* **2017**, *53* (11), 1805–1808. https://doi.org/10.1039/C6CC10065A.

(69) Lin, X.; Huang, J.; Tan, H.; Huang, J.; Zhang, B. K3V2(PO4)2F3 as a Robust Cathode for Potassium-Ion Batteries. *Energy Storage Mater.* **2019**, *16*, 97–101. https://doi.org/10.1016/J.ENSM.2018.04.026.

(70) Recham, N.; Rousse, G.; Sougrati, M. T.; Chotard, J. N.; Frayret, C.; Mariyappan, S.; Melot, B. C.; Jumas, J. C.; Tarascon, J. M. Preparation and Characterization of a Stable FeSO4F-Based Framework for Alkali Ion Insertion Electrodes. *Chem. Mater.* **2012**, *24* (22), 4363–4370. https://doi.org/10.1021/CM302428W.

(71) Lander, L.; Rousse, G.; Abakumov, A. M.; Sougrati, M.; Van Tendeloo, G.; Tarascon, J. M. Structural, Electrochemical and Magnetic Properties of a Novel KFeSO4F Polymorph. *J. Mater. Chem. A* **2015**, *3* (39), 19754–19764. https://doi.org/10.1039/C5TA05548B.

(72) Jian, Z.; Liang, Y.; Pérez, I. A. R.; Yao, Y.; Ji, X. Poly(Anthraquinonyl Sulfide) Cathode for Potassium-Ion Batteries. *Electrochem. commun.* **2016**, *71*, 5–8. https://doi.org/10.1016/J.ELECOM.2016.07.011.

(73) Chen, Y.; Luo, W.; Carter, M.; Zhou, L.; Dai, J.; Fu, K.; Lacey, S.; Li, T.; Wan, J.; Han, X.; Bao, Y.; Hu, L. Organic Electrode for Non-Aqueous Potassium-Ion Batteries. *Nano Energy* **2015**, *18*, 205–211. https://doi.org/10.1016/J.NANOEN.2015.10.015.

(74) Fan, L.; Ma, R.; Wang, J.; Yang, H.; Lu, B. An Ultrafast and Highly Stable Potassium–Organic Battery. *Adv. Mater.* **2018**, *30* (51). https://doi.org/10.1002/ADMA.201805486.

(75) Hameed, A. S.; Katogi, A.; Kubota, K.; Komaba, S. A Layered Inorganic–Organic Open Framework Material as a 4 V Positive Electrode with High-Rate Performance for K-Ion

Batteries. *Adv. Energy Mater.* **2019**, *9* (45). https://doi.org/10.1002/AENM.201902528.

(76)  Pham, T. A.; Kweon, K. E.; Samanta, A.; Lordi, V.; Pask, J. E. Solvation and Dynamics of Sodium and Potassium in Ethylene Carbonate from Ab Initio Molecular Dynamics Simulations. *J. Phys. Chem. C* **2017**, *121* (40), 21913–21920. https://doi.org/10.1021/ACS.JPCC.7B06457/ASSET/IMAGES/MEDIUM/JP-2017-06457P_0009.GIF.

(77)  Okoshi, M.; Yamada, Y.; Komaba, S.; Yamada, A.; Nakai, H. Theoretical Analysis of Interactions between Potassium Ions and Organic Electrolyte Solvents: A Comparison with Lithium, Sodium, and Magnesium Ions. *J. Electrochem. Soc.* **2017**, *164* (2), A54–A60. https://doi.org/10.1149/2.0211702JES/XML.

(78)  Hosaka, T.; Matsuyama, T.; Kubota, K.; Yasuno, S.; Komaba, S. Development of KPF6/KFSA Binary-Salt Solutions for Long-Life and High-Voltage K-Ion Batteries. *ACS Appl. Mater. Interfaces* **2020**, *12* (31), 34873–34881. https://doi.org/10.1021/ACSAMI.0C08002/ASSET/IMAGES/LARGE/AM0C08002_0007.JPEG.

(79)  Kim, H. J.; Voronina, N.; Yashiro, H.; Myung, S. T. Highly Concentrated Electrolyte Enabling High-Voltage Application of Metallic Components for Potassium-Ion Batteries. *J. Power Sources* **2021**, *510*, 230436. https://doi.org/10.1016/J.JPOWSOUR.2021.230436.

(80)  Komaba, S.; Itabashi, T.; Kaplan, B.; Groult, H.; Kumagai, N. Enhancement of Li-Ion Battery Performance of Graphite Anode by Sodium Ion as an Electrolyte Additive. *Electrochem. commun.* **2003**, *5* (11), 962–966. https://doi.org/10.1016/J.ELECOM.2003.09.003.

(81)  Yamada, Y.; Iriyama, Y.; Abe, T.; Ogumi, Z. Kinetics of Lithium Ion Transfer at the Interface between Graphite and Liquid Electrolytes: Effects of Solvent and Surface Film. *Langmuir* **2009**, *25* (21), 12766–12770. https://doi.org/10.1021/LA901829V.

(82)  Ota, H.; Shima, K.; Ue, M.; Yamaki, J. ichi. Effect of Vinylene Carbonate as Additive to Electrolyte for Lithium Metal Anode. *Electrochim. Acta* **2004**, *49* (4), 565–572. https://doi.org/10.1016/J.ELECTACTA.2003.09.010.

(83)  Zhao, W.; Ji, Y.; Zhang, Z.; Lin, M.; Wu, Z.; Zheng, X.; Li, Q.; Yang, Y. Recent Advances in the Research of Functional Electrolyte Additives for Lithium-Ion Batteries. *Curr. Opin. Electrochem.* **2017**, *6* (1), 84–91. https://doi.org/10.1016/J.COELEC.2017.10.012.

(84)  Zhang, W.; Pang, W. K.; Sencadas, V.; Guo, Z. Understanding High-Energy-Density Sn4P3 Anodes for Potassium-Ion Batteries. *Joule* **2018**, *2* (8), 1534–1547. https://doi.org/10.1016/J.JOULE.2018.04.022.

(85)  Xiao, N.; McCulloch, W. D.; Wu, Y. Reversible Dendrite-Free Potassium Plating and

Stripping Electrochemistry for Potassium Secondary Batteries. *J. Am. Chem. Soc.* **2017**, *139* (28), 9475–9478. https://doi.org/10.1021/jacs.7b04945.

(86) Fan, L.; Chen, S.; Ma, R.; Wang, J.; Wang, L.; Zhang, Q.; Zhang, E.; Liu, Z.; Lu, B. Ultrastable Potassium Storage Performance Realized by Highly Effective Solid Electrolyte Interphase Layer. *Small* **2018**, *14* (30), 1801806. https://doi.org/10.1002/SMLL.201801806.

(87) Hosaka, T.; Matsuyama, T.; Kubota, K.; Tatara, R.; Komaba, S. KFSA/Glyme Electrolytes for 4 V-Class K-Ion Batteries. *J. Mater. Chem. A* **2020**, *8* (45), 23766–23771. https://doi.org/10.1039/D0TA08851J.

(88) Pekka Peljo; H. Girault, H. Electrochemical Potential Window of Battery Electrolytes: The HOMO–LUMO Misconception. *Energy Environ. Sci.* **2018**, *11* (9), 2306–2309. https://doi.org/10.1039/C8EE01286E.

(89) Komaba, S.; Hasegawa, T.; Dahbi, M.; Kubota, K. Potassium Intercalation into Graphite to Realize High-Voltage/High-Power Potassium-Ion Batteries and Potassium-Ion Capacitors. *Electrochem. commun.* **2015**, *60*, 172–175. https://doi.org/10.1016/J.ELECOM.2015.09.002.

(90) Onuma, H.; Kubota, K.; Muratsubaki, S.; Ota, W.; Shishkin, M.; Sato, H.; Yamashita, K.; Yasuno, S.; Komaba, S. Phase Evolution of Electrochemically Potassium Intercalated Graphite. *J. Mater. Chem. A* **2021**, *9* (18), 11187–11200. https://doi.org/10.1039/D0TA12607A.

(91) Rüdorff, W.; Hofmann, U. Über Graphitsalze. *Zeitschrift für Anorg. und Allg. Chemie* **1938**, *238* (1), 1–50. https://doi.org/10.1002/ZAAC.19382380102.

(92) Kim, H.; Yoon, G.; Lim, K.; Kang, K. A Comparative Study of Graphite Electrodes Using the Co-Intercalation Phenomenon for Rechargeable Li, Na and K Batteries. *Chem. Commun.* **2016**, *52* (85), 12618–12621. https://doi.org/10.1039/C6CC05362A.

(93) Shimizu, M.; Koya, T.; Nakahigashi, A.; Urakami, N.; Yamakami, T.; Arai, S. Kinetics Study and Degradation Analysis through Raman Spectroscopy of Graphite as a Negative-Electrode Material for Potassium-Ion Batteries. *J. Phys. Chem. C* **2020**, *124* (24), 13008–13016. https://doi.org/10.1021/ACS.JPCC.0C03020/ASSET/IMAGES/LARGE/JP0C03020_0007.JPEG.

(94) Beltrop, K.; Beuker, S.; Heckmann, A.; Winter, M.; Placke, T. Alternative Electrochemical Energy Storage: Potassium-Based Dual-Graphite Batteries. *Energy Environ. Sci.* **2017**, *10* (10), 2090–2094. https://doi.org/10.1039/C7EE01535F.

(95) Fan, L.; Ma, R.; Zhang, Q.; Jia, X.; Lu, B. Graphite Anode for a Potassium-Ion Battery with

Unprecedented Performance. *Angew. Chemie* **2019**, *131* (31), 10610–10615. https://doi.org/10.1002/ANGE.201904258.

(96)    Adams, R. A.; Varma, A.; Pol, V. G. Temperature Dependent Electrochemical Performance of Graphite Anodes for K-Ion and Li-Ion Batteries. *J. Power Sources* **2019**, *410–411*, 124–131. https://doi.org/10.1016/J.JPOWSOUR.2018.11.007.

(97)    Wang, L.; Yang, J.; Li, J.; Chen, T.; Chen, S.; Wu, Z.; Qiu, J.; Wang, B.; Gao, P.; Niu, X.; Li, H. Graphite as a Potassium Ion Battery Anode in Carbonate-Based Electrolyte and Ether-Based Electrolyte. *J. Power Sources* **2019**, *409*, 24–30. https://doi.org/10.1016/J.JPOWSOUR.2018.10.092.

(98)    Xing, Z.; Qi, Y.; Jian, Z.; Ji, X. Polynanocrystalline Graphite: A New Carbon Anode with Superior Cycling Performance for K-Ion Batteries. *ACS Appl. Mater. Interfaces* **2017**, *9* (5), 4343–4351.
https://doi.org/10.1021/ACSAMI.6B06767/SUPPL_FILE/AM6B06767_SI_001.PDF.

(99)    Chen, J.; Yang, B.; Li, H.; Ma, P.; Lang, J.; Yan, X. Candle Soot: Onion-like Carbon, an Advanced Anode Material for a Potassium-Ion Hybrid Capacitor. *J. Mater. Chem. A* **2019**, *7* (15), 9247–9252. https://doi.org/10.1039/C9TA01653H.

(100)   Zhao, J.; Zou, X.; Zhu, Y.; Xu, Y.; Wang, C. Electrochemical Intercalation of Potassium into Graphite. *Adv. Funct. Mater.* **2016**, *26* (44), 8103–8110. https://doi.org/10.1002/ADFM.201602248.

(101)   Franklin, R. Crystallite Growth in Graphitizing and Non-Graphitizing Carbons. *Proc. R. Soc. London. Ser. A. Math. Phys. Sci.* **1951**, *209* (1097), 196–218. https://doi.org/10.1098/RSPA.1951.0197.

(102)   Anji Reddy, M.; Helen, M.; Groß, A.; Fichtner, M.; Euchner, H. Insight into Sodium Insertion and the Storage Mechanism in Hard Carbon. *ACS Energy Lett.* **2018**, *3* (12), 2851–2857.
https://doi.org/10.1021/ACSENERGYLETT.8B01761/SUPPL_FILE/NZ8B01761_SI_001.PDF.

(103)   TUINSTRA F; KOENIG JL. Raman Spectrum of Graphite. *J. Chem. Phys.* **2003**, *53* (3), 1126. https://doi.org/10.1063/1.1674108.

(104)   Thomsen, C.; Reich, S. Double Resonant Raman Scattering in Graphite. *Phys. Rev. Lett.* **2000**, *85* (24), 5214. https://doi.org/10.1103/PhysRevLett.85.5214.

(105)   Chen, M.; Wang, W.; Liang, X.; Gong, S.; Liu, J.; Wang, Q.; Guo, S.; Yang, H. Sulfur/Oxygen Codoped Porous Hard Carbon Microspheres for High-Performance Potassium-Ion Batteries. *Adv. Energy Mater.* **2018**, *8* (19), 1800171. https://doi.org/10.1002/AENM.201800171.

(106) Wang, Y.; Hu, Y. J.; Hao, X.; Peng, P.; Shi, J. Y.; Peng, F.; Sun, R. C. Hydrothermal Synthesis and Applications of Advanced Carbonaceous Materials from Biomass: A Review. *Adv. Compos. Hybrid Mater. 2020 33* **2020**, *3* (3), 267–284. https://doi.org/10.1007/S42114-020-00158-0.

(107) Li, R.; Wang, L.; Shahbazi, A. A Review of Hydrothermal Carbonization of Carbohydrates for Carbon Spheres Preparation. *Trends Renew. Energy* **2015**, *1* (1), 43–56. https://doi.org/10.17737/TRE.2015.1.1.009.

(108) Sevilla, M.; Fuertes, A. B. The Production of Carbon Materials by Hydrothermal Carbonization of Cellulose. *Carbon N. Y.* **2009**, *47* (9), 2281–2289. https://doi.org/10.1016/J.CARBON.2009.04.026.

(109) Sevilla, M.; Fuertes, A. B. Chemical and Structural Properties of Carbonaceous Products Obtained by Hydrothermal Carbonization of Saccharides. *Chem. – A Eur. J.* **2009**, *15* (16), 4195–4203. https://doi.org/10.1002/CHEM.200802097.

(110) Sun, P.; Heng, M.; Sun, S.; Chen, J. Direct Liquefaction of Paulownia in Hot Compressed Water: Influence of Catalysts. *Energy* **2010**, *35* (12), 5421–5429. https://doi.org/10.1016/J.ENERGY.2010.07.005.

(111) Falco, C.; Baccile, N.; Titirici, M. M. Morphological and Structural Differences between Glucose, Cellulose and Lignocellulosic Biomass Derived Hydrothermal Carbons. *Green Chem.* **2011**, *13* (11), 3273–3281. https://doi.org/10.1039/C1GC15742F.

(112) Romero-Anaya, A. J.; Ouzzine, M.; Lillo-Ródenas, M. A.; Linares-Solano, A. Spherical Carbons: Synthesis, Characterization and Activation Processes. *Carbon N. Y.* **2014**, *68*, 296–307. https://doi.org/10.1016/J.CARBON.2013.11.006.

(113) Yavari, S.; Malakahmad, A.; Sapari, N. B.; Yavari, S. Sorption Properties Optimization of Agricultural Wastes-Derived Biochars Using Response Surface Methodology. *Process Saf. Environ. Prot.* **2017**, *109*, 509–519. https://doi.org/10.1016/J.PSEP.2017.05.002.

(114) Liu, J.; Tian, P.; Ye, J.; Zhou, L.; Gong, W.; Lin, Y.; Ning, G. Hydrothermal Synthesis of Carbon Microspheres from Glucose: Tuning Sphere Size by Adding Oxalic Acid. *http://dx.doi.org/10.1246/cl.2009.948* **2009**, *38* (10), 948–949. https://doi.org/10.1246/CL.2009.948.

(115) Prabakar, S. J. R.; Han, S. C.; Park, C.; Bhairuba, I. A.; Reece, M. J.; Sohn, K.-S.; Pyo, M. Spontaneous Formation of Interwoven Porous Channels in Hard-Wood-Based Hard-Carbon for High-Performance Anodes in Potassium-Ion Batteries. *J. Electrochem. Soc.* **2017**, *164* (9), A2012–A2016. https://doi.org/10.1149/2.1251709JES/XML.

(116) Li, Y.; Adams, R. A.; Arora, A.; Pol, V. G.; Levine, A. M.; Lee, R. J.; Akato, K.; Naskar, A. K.; Paranthaman, M. P. Sustainable Potassium-Ion Battery Anodes Derived from Waste-

Tire Rubber. *J. Electrochem. Soc.* **2017**, *164* (6), A1234–A1238. https://doi.org/10.1149/2.1391706JES/XML.

(117) Yamamoto, H.; Muratsubaki, S.; Kubota, K.; Fukunishi, M.; Watanabe, H.; Kim, J.; Komaba, S. Synthesizing Higher-Capacity Hard-Carbons from Cellulose for Na- and K-Ion Batteries. *J. Mater. Chem. A* **2018**, *6* (35), 16844–16848. https://doi.org/10.1039/C8TA05203D.

(118) He, X.; Liao, J.; Tang, Z.; Xiao, L.; Ding, X.; Hu, Q.; Wen, Z.; Chen, C. Highly Disordered Hard Carbon Derived from Skimmed Cotton as a High-Performance Anode Material for Potassium-Ion Batteries. *J. Power Sources* **2018**, *396*, 533–541. https://doi.org/10.1016/J.JPOWSOUR.2018.06.073.

(119) Cao, W.; Zhang, E.; Wang, J.; Liu, Z.; Ge, J.; Yu, X.; Yang, H.; Lu, B. Potato Derived Biomass Porous Carbon as Anode for Potassium Ion Batteries. *Electrochim. Acta* **2019**, *293*, 364–370. https://doi.org/10.1016/J.ELECTACTA.2018.10.036.

(120) Wu, Z.; Wang, L.; Huang, J.; Zou, J.; Chen, S.; Cheng, H.; Jiang, C.; Gao, P.; Niu, X. Loofah-Derived Carbon as an Anode Material for Potassium Ion and Lithium Ion Batteries. *Electrochim. Acta* **2019**, *306*, 446–453. https://doi.org/10.1016/J.ELECTACTA.2019.03.165.

(121) Liu, M.; Jing, D.; Shi, Y.; Zhuang, Q. Superior Potassium Storage in Natural O/N–Doped Hard Carbon Derived from Maple Leaves. *J. Mater. Sci. Mater. Electron. 2019 309* **2019**, *30* (9), 8911–8919. https://doi.org/10.1007/S10854-019-01219-X.

(122) Jian, Z.; Hwang, S.; Li, Z.; Hernandez, A. S.; Wang, X.; Xing, Z.; Su, D.; Ji, X. Hard–Soft Composite Carbon as a Long-Cycling and High-Rate Anode for Potassium-Ion Batteries. *Adv. Funct. Mater.* **2017**, *27* (26). https://doi.org/10.1002/ADFM.201700324.

(123) Jian, Z.; Xing, Z.; Bommier, C.; Li, Z.; Ji, X. Hard Carbon Microspheres: Potassium-Ion Anode Versus Sodium-Ion Anode. *Adv. Energy Mater.* **2016**, *6* (3). https://doi.org/10.1002/AENM.201501874.

(124) Kubota, K.; Shimadzu, S.; Yabuuchi, N.; Tominaka, S.; Shiraishi, S.; Abreu-Sepulveda, M.; Manivannan, A.; Gotoh, K.; Fukunishi, M.; Dahbi, M.; Komaba, S. Structural Analysis of Sucrose-Derived Hard Carbon and Correlation with the Electrochemical Properties for Lithium, Sodium, and Potassium Insertion. *Chem. Mater.* **2020**, *32* (7), 2961–2977. https://doi.org/10.1021/ACS.CHEMMATER.9B05235/SUPPL_FILE/CM9B05235_SI_00 1.PDF.

(125) Zhang, J.; Lai, L.; Wang, H.; Chen, M.; Shen, Z. X. Energy Storage Mechanisms of Anode Materials for Potassium Ion Batteries. *Mater. Today Energy* **2021**, *21*, 100747. https://doi.org/10.1016/J.MTENER.2021.100747.

(126) Yang, J.; Ju, Z.; Jiang, Y.; Xing, Z.; Xi, B.; Feng, J.; Xiong, S. Enhanced Capacity and Rate Capability of Nitrogen/Oxygen Dual-Doped Hard Carbon in Capacitive Potassium-Ion Storage. *Adv. Mater.* **2018**, *30* (4), 1700104. https://doi.org/10.1002/ADMA.201700104.

(127) Huang, Y.; Wang, Y.; Bai, P.; Xu, Y. Storage Mechanism of Alkali Metal Ions in the Hard Carbon Anode: An Electrochemical Viewpoint. *ACS Appl. Mater. Interfaces* **2021**, *13* (32), 38441–38449. https://doi.org/10.1021/ACSAMI.1C12150/SUPPL_FILE/AM1C12150_SI_001.PDF.

(128) Liu, Y.; Dai, H.; Wu, L.; Zhou, W.; He, L.; Wang, W.; Yan, W.; Huang, Q.; Fu, L.; Wu, Y. A Large Scalable and Low-Cost Sulfur/Nitrogen Dual-Doped Hard Carbon as the Negative Electrode Material for High-Performance Potassium-Ion Batteries. *Adv. Energy Mater.* **2019**, *9* (34), 1901379. https://doi.org/10.1002/aenm.201901379.

(129) Wu, X.; Leonard, D. P.; Ji, X. Emerging Non-Aqueous Potassium-Ion Batteries: Challenges and Opportunities. *Chemistry of Materials*. American Chemical Society June 2017, pp 5031–5042. https://doi.org/10.1021/acs.chemmater.7b01764.

(130) Yamada, Y.; Furukawa, K.; Sodeyama, K.; Kikuchi, K.; Yaegashi, M.; Tateyama, Y.; Yamada, A. Unusual Stability of Acetonitrile-Based Superconcentrated Electrolytes for Fast-Charging Lithium-Ion Batteries. *J. Am. Chem. Soc.* **2014**, *136* (13), 5039–5046. https://doi.org/10.1021/JA412807W/SUPPL_FILE/JA412807W_SI_001.PDF.

(131) Takada, K.; Yamada, Y.; Watanabe, E.; Wang, J.; Sodeyama, K.; Tateyama, Y.; Hirata, K.; Kawase, T.; Yamada, A. Unusual Passivation Ability of Superconcentrated Electrolytes toward Hard Carbon Negative Electrodes in Sodium-Ion Batteries. *ACS Appl. Mater. Interfaces* **2017**, *9* (39), 33802–33809. https://doi.org/10.1021/acsami.7b08414.

(132) Wang, J.; Yamada, Y.; Sodeyama, K.; Watanabe, E.; Takada, K.; Tateyama, Y.; Yamada, A. Fire-Extinguishing Organic Electrolytes for Safe Batteries. *Nat. Energy 2017 31* **2017**, *3* (1), 22–29. https://doi.org/10.1038/s41560-017-0033-8.

(133) Wu, Z.; Zou, J.; Shabanian, S.; Golovin, K.; Liu, J. The Roles of Electrolyte Chemistry in Hard Carbon Anode for Potassium-Ion Batteries. *Chem. Eng. J.* **2022**, *427*, 130972. https://doi.org/10.1016/J.CEJ.2021.130972.

(134) Wang, H.; Yu, D.; Wang, X.; Niu, Z.; Chen, M.; Cheng, L.; Zhou, W.; Guo, L. Electrolyte Chemistry Enables Simultaneous Stabilization of Potassium Metal and Alloying Anode for Potassium-Ion Batteries. *Angew. Chemie Int. Ed.* **2019**, *58* (46), 16451–16455. https://doi.org/10.1002/ANIE.201908607.

(135) Luo, W.; Wan, J.; Ozdemir, B.; Bao, W.; Chen, Y.; Dai, J.; Lin, H.; Xu, Y.; Gu, F.; Barone, V.; Hu, L. Potassium Ion Batteries with Graphitic Materials. *Nano Lett.* **2015**, *15* (11), 7671–7677.

https://doi.org/10.1021/ACS.NANOLETT.5B03667/SUPPL_FILE/NL5B03667_SI_001.PDF.

(136) Guo, R.; Liu, X.; Wen, B.; Liu, F.; Meng, J.; Wu, P.; Wu, J.; Li, Q.; Mai, L. Engineering Mesoporous Structure in Amorphous Carbon Boosts Potassium Storage with High Initial Coulombic Efficiency. *Nano-Micro Lett.* **2020**, *12* (1), 1–12. https://doi.org/10.1007/S40820-020-00481-7/FIGURES/5.

(137) Petrícek, V.; Dušek, M.; Palatinus, L. Crystallographic Computing System JANA2006: General Features. *Zeitschrift fur Krist.* **2014**, *229* (5), 345–352. https://doi.org/10.1515/ZKRI-2014-1737.

(138) Luchkin, S. Y.; Lipovskikh, S. A.; Katorova, N. S.; Savina, A. A.; Abakumov, A. M.; Stevenson, K. J. Solid-Electrolyte Interphase Nucleation and Growth on Carbonaceous Negative Electrodes for Li-Ion Batteries Visualized with in Situ Atomic Force Microscopy. *Sci. Reports 2020 101* **2020**, *10* (1), 1–10. https://doi.org/10.1038/s41598-020-65552-6.

(139) Wang, Y.; Hu, Y.-J.; Hao, X.; Peng, P.; Shi, J.-Y.; Peng, F.; Sun, R.-C. Hydrothermal Synthesis and Applications of Advanced Carbonaceous Materials from Biomass: A Review. https://doi.org/10.1007/s42114-020-00158-0/Published.

(140) El Moctar, I.; Ni, Q.; Bai, Y.; Wu, F.; Wu, C. Hard Carbon Anode Materials for Sodium-Ion Batteries. *Funct. Mater. Lett.* **2018**, *11* (6). https://doi.org/10.1142/S1793604718300037.

(141) Hasegawa, G.; Kanamori, K.; Kannari, N.; Ozaki, J. ichi; Nakanishi, K.; Abe, T. Hard Carbon Anodes for Na-Ion Batteries: Toward a Practical Use. *ChemElectroChem* **2015**, *2* (12), 1917–1920. https://doi.org/10.1002/CELC.201500412.

(142) Zhang, X.; Devine, T. M. Identity of Passive Film Formed on Aluminum in Li-Ion Battery Electrolytes with LiPF[Sub 6]. *J. Electrochem. Soc.* **2006**, *153* (9), B344. https://doi.org/10.1149/1.2214465.

(143) Wang, J.; Yamada, Y.; Sodeyama, K.; Chiang, C. H.; Tateyama, Y.; Yamada, A. Superconcentrated Electrolytes for a High-Voltage Lithium-Ion Battery. *Nat. Commun.* **2016**, *7*. https://doi.org/10.1038/ncomms12032.

(144) Yamada, Y.; Chiang, C. H.; Sodeyama, K.; Wang, J.; Tateyama, Y.; Yamada, A. Corrosion Prevention Mechanism of Aluminum Metal in Superconcentrated Electrolytes. *ChemElectroChem* **2015**, *2* (11), 1687–1694. https://doi.org/10.1002/celc.201500235.

(145) Brouillette, D.; Irish, D. E.; Taylor, N. J.; Perron, G.; Odziemkowski, M.; Desnoyers, J. E. Stable Solvates in Solution of Lithium Bis(Trifluoromethylsulfone)Imide in Glymes and Other Aprotic Solvents: Phase Diagrams, Crystallography and Raman Spectroscopy. *Phys. Chem. Chem. Phys.* **2002**, *4* (24), 6063–6071. https://doi.org/10.1039/b203776a.

(146) Mandai, T.; Tsuzuki, S.; Ueno, K.; Dokko, K.; Watanabe, M. Pentaglyme-K Salt Binary Mixtures: Phase Behavior, Solvate Structures, and Physicochemical Properties. *Phys. Chem. Chem. Phys.* **2015**, *17* (4), 2838–2849. https://doi.org/10.1039/c4cp05017g.

(147) Machida, K.; Miyazawa, T. Infrared and Raman Spectra of Polyethyleneglycol Dimethylethers in the Liquid State. *Spectrochim. Acta* **1964**, *20* (12), 1865–1873. https://doi.org/10.1016/0371-1951(64)80191-0.

(148) Dhumal, N. R.; Gejji, S. P. Theoretical Studies on Blue versus Red Shifts in Diglyme-M +- X- (M = Li, Na, and K and X = CF3so 3, PF6, and (CF3so2)2N). *J. Phys. Chem. A* **2006**, *110* (1), 219–227. https://doi.org/10.1021/jp054209g.

(149) Han, S. D.; Yun, S. H.; Borodin, O.; Seo, D. M.; Sommer, R. D.; Young, V. G.; Henderson, W. A. Solvate Structures and Computational/Spectroscopic Characterization of LiPF6 Electrolytes. *J. Phys. Chem. C* **2015**, *119* (16), 8492–8500. https://doi.org/10.1021/acs.jpcc.5b00826.

(150) Zheng, J.; Chen, S.; Zhao, W.; Song, J.; Engelhard, M. H.; Zhang, J. G. Extremely Stable Sodium Metal Batteries Enabled by Localized High-Concentration Electrolytes. *ACS Energy Lett.* **2018**, *3* (2), 315–321. https://doi.org/10.1021/acsenergylett.7b01213.

(151) Kimura, K.; Motomatsu, J.; Tominaga, Y. Correlation between Solvation Structure and Ion-Conductive Behavior of Concentrated Poly(Ethylene Carbonate)-Based Electrolytes. *J. Phys. Chem. C* **2016**, *120* (23), 12385–12391. https://doi.org/10.1021/acs.jpcc.6b03277.

(152) Ortí, E.; Viruela, P. M.; Viruela, R.; Effenberger, F.; Hernández, V.; López Navarrete, J. T. Raman and Theoretical Study of the Solvent Effects on the Sizable Intramolecular Charge Transfer in the Push-Pull 5-(Dimethylamino)-5′- Nitro-2,2′-Bithiophene. *J. Phys. Chem. A* **2005**, *109* (39), 8724–8731. https://doi.org/10.1021/jp052137n.

(153) Yamada, Y.; Usui, K.; Chiang, C. H.; Kikuchi, K.; Furukawa, K.; Yamada, A. General Observation of Lithium Intercalation into Graphite in Ethylene-Carbonate-Free Superconcentrated Electrolytes. *ACS Applied Materials and Interfaces*. American Chemical Society July 2014, pp 10892–10899. https://doi.org/10.1021/am5001163.

(154) Doi, T.; Masuhara, R.; Hashinokuchi, M.; Shimizu, Y.; Inaba, M. Concentrated LiPF6/PC Electrolyte Solutions for 5-V LiNi0.5Mn1.5O4 Positive Electrode in Lithium-Ion Batteries. *Electrochim. Acta* **2016**, *209*, 219–224. https://doi.org/10.1016/j.electacta.2016.05.062.

(155) Westman, K.; Dugas, R.; Jankowski, P.; Wieczorek, W.; Gachot, G.; Morcrette, M.; Irisarri, E.; Ponrouch, A.; Palacín, M. R.; Tarascon, J. M.; Johansson, P. Diglyme Based Electrolytes for Sodium-Ion Batteries. *ACS Appl. Energy Mater.* **2018**, *1* (6), 2671–2680. https://doi.org/10.1021/acsaem.8b00360.

(156) Valøen, L. O.; Reimers, J. N. Transport Properties of LiPF[Sub 6]-Based Li-Ion Battery

Electrolytes. *J. Electrochem. Soc.* **2005**, *152* (5), A882. https://doi.org/10.1149/1.1872737.

(157) Smith, A. J.; Burns, J. C.; Zhao, X.; Xiong, D.; Dahn, J. R. A High Precision Coulometry Study of the SEI Growth in Li/Graphite Cells. *J. Electrochem. Soc.* **2011**, *158* (5), 447–452. https://doi.org/10.1149/1.3557892.

(158) Prasad, G. K.; Rahn, C. D. Model Based Identification of Aging Parameters in Lithium Ion Batteries. *J. Power Sources* **2013**, *232*, 79–85. https://doi.org/10.1016/j.jpowsour.2013.01.041.

(159) Aurbach, D.; Markovsky, B.; Salitra, G.; Markevich, E.; Talyossef, Y.; Koltypin, M.; Nazar, L.; Ellis, B.; Kovacheva, D. Review on Electrode-Electrolyte Solution Interactions, Related to Cathode Materials for Li-Ion Batteries. *Journal of Power Sources*. March 2007, pp 491–499. https://doi.org/10.1016/j.jpowsour.2006.10.025.

(160) Pieczonka, N. P. W.; Liu, Z.; Lu, P.; Olson, K. L.; Moote, J.; Powell, B. R.; Kim, J. H. Understanding Transition-Metal Dissolution Behavior in LiNi 0.5Mn1.5O4 High-Voltage Spinel for Lithium Ion Batteries. *J. Phys. Chem. C* **2013**, *117* (31), 15947–15957. https://doi.org/10.1021/jp405158m.

(161) Yoshida, K.; Nakamura, M.; Kazue, Y.; Tachikawa, N.; Tsuzuki, S.; Seki, S.; Dokko, K.; Watanabe, M. Oxidative-Stability Enhancement and Charge Transport Mechanism in Glyme-Lithium Salt Equimolar Complexes. *J. Am. Chem. Soc.* **2011**, *133* (33), 13121–13129. https://doi.org/10.1021/ja203983r.

(162) Nikitina, V. A.; Zakharkin, M. V.; Vassiliev, S. Y.; Yashina, L. V.; Antipov, E. V.; Stevenson, K. J. Lithium Ion Coupled Electron-Transfer Rates in Superconcentrated Electrolytes: Exploring the Bottlenecks for Fast Charge-Transfer Rates with LiMn2O4 Cathode Materials. *Langmuir* **2017**, *33* (37), 9378–9389. https://doi.org/10.1021/acs.langmuir.7b01016.

(163) Moyer, K.; Donohue, J.; Ramanna, N.; Cohn, A. P.; Muralidharan, N.; Eaves, J.; Pint, C. L. High-Rate Potassium Ion and Sodium Ion Batteries by Co-Intercalation Anodes and Open Framework Cathodes. *Nanoscale* **2018**, *10* (28), 13335–13342. https://doi.org/10.1039/c8nr01685b.

(164) Hosaka, T.; Komaba, S. Development of Nonaqueous Electrolytes for High-Voltage K-Ion Batteries. *https://doi.org/10.1246/bcsj.20210412* **2022**, *95* (4), 569–581. https://doi.org/10.1246/BCSJ.20210412.

(165) Eshetu, G. G.; Diemant, T.; Hekmatfar, M.; Grugeon, S.; Behm, R. J.; Laruelle, S.; Armand, M.; Passerini, S. Impact of the Electrolyte Salt Anion on the Solid Electrolyte Interphase Formation in Sodium Ion Batteries. *Nano Energy* **2019**, *55*, 327–340. https://doi.org/10.1016/j.nanoen.2018.10.040.

(166) Ells, A. W.; May, R.; Marbella, L. E. Potassium Fluoride and Carbonate Lead to Cell Failure in Potassium-Ion Batteries. *ACS Appl. Mater. Interfaces* **2021**, *13* (45), 53841–53849. https://doi.org/10.1021/ACSAMI.1C15174/ASSET/IMAGES/LARGE/AM1C15174_000 7.JPEG.

(167) Zhu, Z.; Tang, Y.; Lv, Z.; Wei, J.; Zhang, Y.; Wang, R.; Zhang, W.; Xia, H.; Ge, M.; Chen, X. Fluoroethylene Carbonate Enabling a Robust LiF-Rich Solid Electrolyte Interphase to Enhance the Stability of the MoS2 Anode for Lithium-Ion Storage. *Angew. Chemie - Int. Ed.* **2018**, *57* (14), 3656–3660. https://doi.org/10.1002/anie.201712907.

(168) Buqa, H.; Würsig, A.; Vetter, J.; Spahr, M. E.; Krumeich, F.; Novák, P. SEI Film Formation on Highly Crystalline Graphitic Materials in Lithium-Ion Batteries. In *Journal of Power Sources*; Elsevier, 2006; Vol. 153, pp 385–390. https://doi.org/10.1016/j.jpowsour.2005.05.036.

(169) Chang, C. C.; Hsu, S. H.; Jung, Y. F.; Yang, C. H. Vinylene Carbonate and Vinylene Trithiocarbonate as Electrolyte Additives for Lithium Ion Battery. *J. Power Sources* **2011**, *196* (22), 9605–9611. https://doi.org/10.1016/J.JPOWSOUR.2011.06.058.

(170) Aurbach, D.; Gamolsky, K.; Markovsky, B.; Gofer, Y.; Schmidt, M.; Heider, U. On the Use of Vinylene Carbonate (VC) as an Additive to Electrolyte Solutions for Li-Ion Batteries. *Electrochim. Acta* **2002**, *47* (9), 1423–1439. https://doi.org/10.1016/S0013-4686(01)00858-1.

(171) Wang, A.; Kadam, S.; Li, H.; Shi, S.; Qi, Y. Review on Modeling of the Anode Solid Electrolyte Interphase (SEI) for Lithium-Ion Batteries. *npj Comput. Mater.* **2018**, *4* (1). https://doi.org/10.1038/S41524-018-0064-0.

(172) Qian, Y.; Schultz, C.; Niehoff, P.; Schwieters, T.; Nowak, S.; Schappacher, F. M.; Winter, M. Investigations on the Electrochemical Decomposition of the Electrolyte Additive Vinylene Carbonate in Li Metal Half Cells and Lithium Ion Full Cells. *J. Power Sources* **2016**, *332*, 60–71. https://doi.org/10.1016/J.JPOWSOUR.2016.09.100.

(173) Michan, A. L.; Parimalam, B. S.; Leskes, M.; Kerber, R. N.; Yoon, T.; Grey, C. P.; Lucht, B. L. Fluoroethylene Carbonate and Vinylene Carbonate Reduction: Understanding Lithium-Ion Battery Electrolyte Additives and Solid Electrolyte Interphase Formation. *Chem. Mater.* **2016**, *28* (22), 8149–8159. https://doi.org/10.1021/ACS.CHEMMATER.6B02282.

(174) Hosaka, T.; Muratsubaki, S.; Kubota, K.; Onuma, H.; Komaba, S. Potassium Metal as Reliable Reference Electrodes of Nonaqueous Potassium Cells. *J. Phys. Chem. Lett.* **2019**, *10* (12), 3296–3300. https://doi.org/10.1021/ACS.JPCLETT.9B00711.

(175) Soto, F. A.; Ma, Y.; Martinez De La Hoz, J. M.; Seminario, J. M.; Balbuena, P. B. Formation

and Growth Mechanisms of Solid-Electrolyte Interphase Layers in Rechargeable Batteries. *Chem. Mater.* **2015**, *27* (23), 7990–8000. https://doi.org/10.1021/ACS.CHEMMATER.5B03358.

(176) Lemordant, D.; Zhang, W.; Ghamouss, F.; Farhat, D.; Darwiche, A.; Monconduit, L.; Dedryvère, R.; Martinez, H.; Cadra, S.; Lestriez, B. Artificial SEI for Lithium-Ion Battery Anodes: Impact of Fluorinated and Nonfluorinated Additives. *Adv. Fluoride-Based Mater. Energy Convers.* **2015**, 173–202. https://doi.org/10.1016/B978-0-12-800679-5.00008-7.

(177) Sun, Y.; Zheng, G.; Seh, Z. W.; Liu, N.; Wang, S.; Sun, J.; Lee, H. R.; Cui, Y. Graphite-Encapsulated Li-Metal Hybrid Anodes for High-Capacity Li Batteries. *Chem* **2016**, *1* (2), 287–297. https://doi.org/10.1016/J.CHEMPR.2016.07.009.

(178) Nellist, M. R.; Chen, Y.; Mark, A.; Gödrich, S.; Stelling, C.; Jiang, J.; Poddar, R.; Li, C.; Kumar, R.; Papastavrou, G.; Retsch, M.; Brunschwig, B. S.; Huang, Z.; Xiang, C.; Boettcher, S. W. Atomic Force Microscopy with Nanoelectrode Tips for High Resolution Electrochemical, Nanoadhesion and Nanoelectrical Imaging. *Nanotechnology* **2017**, *28* (9). https://doi.org/10.1088/1361-6528/AA5839.

(179) Ding, L.; Song, Z.; Wu, P.; Cheng, J.; Chen, C.; Niu, Y.; Li, B. Electrochemical Oscillations during Copper Electrodissolution in Hydrochloric Acid Solution. *Int. J. Electrochem. Sci.* **2019**, *14* (1), 585–597. https://doi.org/10.20964/2019.01.63.

(180) Lanz, M.; Lehmann, E.; Imhof, R.; Exnar, I.; Novák, P. In Situ Neutron Radiography of Lithium-Ion Batteries during Charge/Discharge Cycling. *J. Power Sources* **2001**, *101* (2), 177–181. https://doi.org/10.1016/S0378-7753(01)00706-6.

(181) Simone, V.; Boulineau, A.; de Geyer, A.; Rouchon, D.; Simonin, L.; Martinet, S. Hard Carbon Derived from Cellulose as Anode for Sodium Ion Batteries: Dependence of Electrochemical Properties on Structure. *J. Energy Chem.* **2016**, *25* (5), 761–768. https://doi.org/10.1016/J.JECHEM.2016.04.016.

(182) Chen, C.; Wang, Z.; Zhang, B.; Miao, L.; Cai, J.; Peng, L.; Huang, Y.; Jiang, J.; Huang, Y.; Zhang, L.; Xie, J. Nitrogen-Rich Hard Carbon as a Highly Durable Anode for High-Power Potassium-Ion Batteries. *Energy Storage Mater.* **2017**, *8*, 161–168. https://doi.org/10.1016/J.ENSM.2017.05.010.

(183) Martin, L.; Martinez, H.; Ulldemolins, M.; Pecquenard, B.; Le Cras, F. Evolution of the Si Electrode/Electrolyte Interface in Lithium Batteries Characterized by XPS and AFM Techniques: The Influence of Vinylene Carbonate Additive. *Solid State Ionics* **2012**, *215*, 36–44. https://doi.org/10.1016/J.SSI.2012.03.042.

(184) Lei, Y.; Han, D.; Dong, J.; Qin, L.; Li, X.; Zhai, D.; Li, B.; Wu, Y.; Kang, F. Unveiling the Influence of Electrode/Electrolyte Interface on the Capacity Fading for Typical Graphite-

Based Potassium-Ion Batteries. *Energy Storage Mater.* **2020**, *24*, 319–328. https://doi.org/10.1016/J.ENSM.2019.07.043.

(185) Ota, H.; Sakata, Y.; Inoue, A.; Yamaguchi, S. Analysis of Vinylene Carbonate Derived SEI Layers on Graphite Anode. *J. Electrochem. Soc.* **2004**, *151* (10), A1659. https://doi.org/10.1149/1.1785795.

(186) Li, J.; Zhuang, N.; Xie, J.; Zhu, Y.; Lai, H.; Qin, W.; Javed, M. S.; Xie, W.; Mai, W. Carboxymethyl Cellulose Binder Greatly Stabilizes Porous Hollow Carbon Submicrospheres in Capacitive K-Ion Storage. *ACS Appl. Mater. Interfaces* **2019**, *11* (17), 15581–15590. https://doi.org/10.1021/ACSAMI.9B02060.

**Appendices A**

Table A1. KVOPO$_4$ lattice parameters refined by Le Bail method for pristine and cycled electrodes

| KVOPO$_4$: space group $Pn2_1a$, after 30 cycles; 2.5-4.5 V vs K$^+$/K | | | | | |
|---|---|---|---|---|---|
| | Initial | 1M KPF$_6$ | 1.5M KPF$_6$ | 2M KPF$_6$ | 2.5M KPF$_6$ |
| $a$, Å | 12.8105 ± 0.0003 | 12.7744 ± 0.0005 | 12.6663 ± 0.0006 | 12.7669 ± 0.0004 | 12.8027 ± 0.0004 |
| $b$, Å | 10.44511 ± 0.00017 | 10.4808 ± 0.0003 | 10.5244 ± 0.0005 | 10.4950 ± 0.0003 | 10.5412 ± 0.0003 |
| $c$, Å | 6.36641 ± 0.00012 | 6.3486 ± 0.00017 | 6.3286 ± 0.0004 | 6.35671 ± 0.00013 | 6.3517 ± 0.0002 |
| Volume, Å$^3$ | 851.87 ± 0.04 | 849.98 ± 0.06 | 843.63 ± 0.10 | 851.73 ± 0.05 | 857.20 ± 0.08 |
| wR$_p$ | 2.76 | 3.5 | 6.85 | 2.84 | 3.33 |
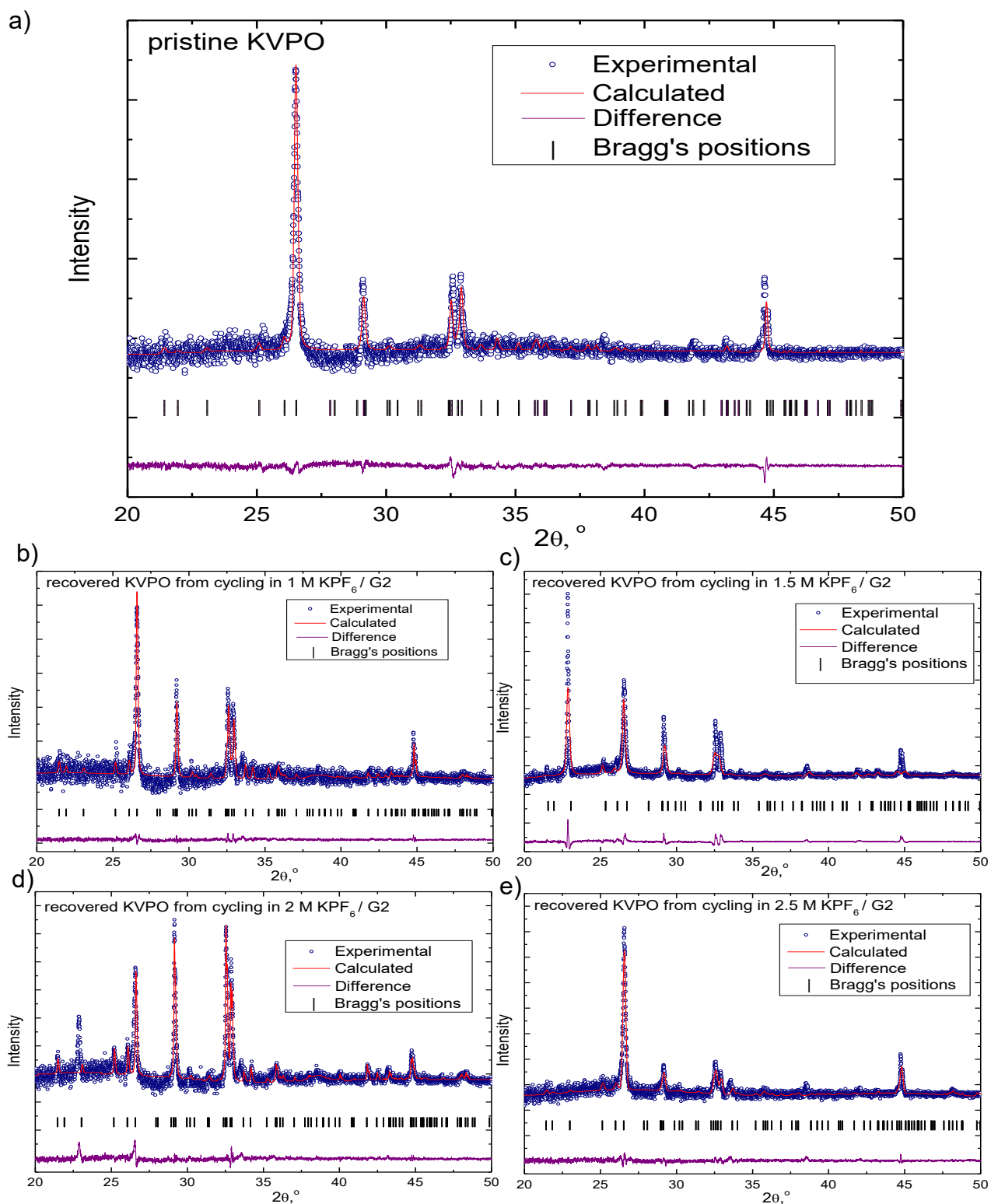
Figure A1. The experimental, calculated and difference X-ray profiles for a) the pristine $KVOPO_4$ electrode on Al foil and for the $KVOPO_4$ electrodes on the Al foil cycled upon 30 cycles in b) 1M c) 1.5M d) 2M e) 2.5M $KPF_6$ in diglyme.

Table A2. KMFCN lattice parameters refined by Le Bail method for pristine and cycled electrodes.

| $K_{1.44}Mn(Fe[CN]_6)_{0.9}*H_2O$: space group $P2_1/c$, after 30 cycles; 2.5-4.5 V vs $K^+/K$ | | | | | |
|---|---|---|---|---|---|
| | Initial | 1M KPF$_6$ | 1.5M KPF$_6$ | 2M KPF$_6$ | 2.5M KPF$_6$ |
| $a$, Å | 6.99660 ± 0.00009 | 6.9810 ± 0.0011 | 6.9385 ± 0.0007 | 6.99794 ± 0.00011 | 6.9984 ± 0.0002 |
| $b$, Å | 7.3521 ± 0.0002 | 7.3297 ± 0.0008 | 7.3965 ± 0.0006 | 7.3651 ± 0.0002 | 7.3641 ± 0.0003 |
| $c$, Å | 12.23711 ± 0.00019 | 12.2483 ± 0.0013 | 12.1776 ± 0.0010 | 12.2526 ± 0.0003 | 12.2606 ± 0.0004 |
| β, ° | 124.5032 ± 0.0014 | 124.337 ± 0.008 | 124.343 ± 0.003 | 124.4528 ± 0.0016 | 124.4726 ± 0.0013 |
| Volume, Å$^3$ | 518.745 ± 0.013 | 517.51 ± 0.11 | 516.01 ± 0.12 | 520.717 ± 0.014 | 520.91 ± 0.04 |
| wR$_p$ | 2.38 | 1.72 | 2.58 | 2.67 | 2.05 |
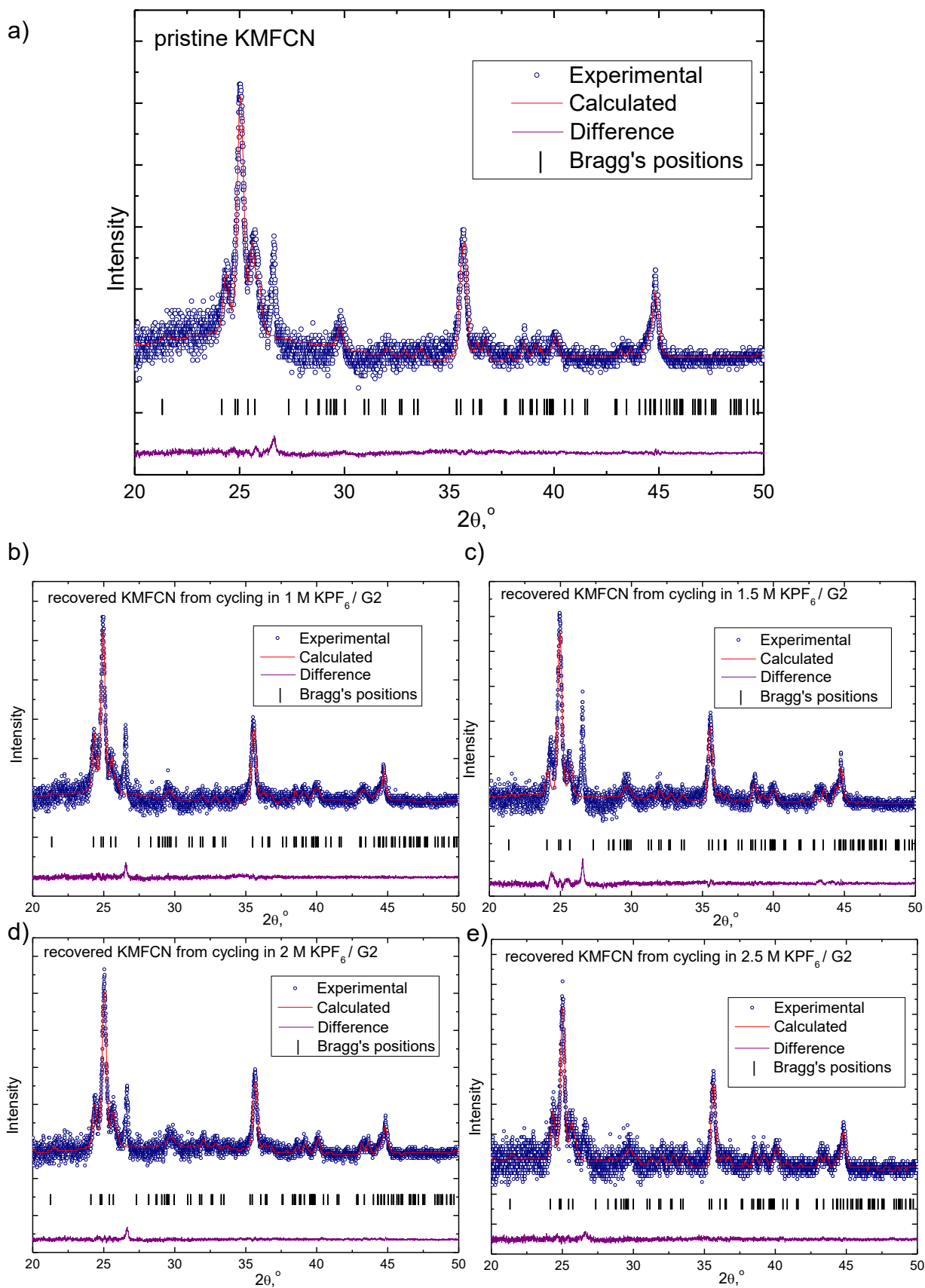
Figure A2. The experimental, calculated and difference X-ray profiles for a) the pristine $K_{1.44}Mn(Fe[CN]_6)_{0.9}*H_2O$ electrode on Al foil and for the $K_{1.44}Mn(Fe[CN]_6)_{0.9}*H_2O$ electrodes on the Al foil cycled upon 30 cycles in b) 1M c) 1.5M d) 2M e) 2.5M $KPF_6$ in diglyme